Experimental Investigation of Silicon Dust Explosions in Pipes

Andreas Faye

Master Thesis in Energy

University of Bergen

Department of Physics and Technology

June 2023

Supervisor: Trygve Skjold

Co-supervisors: Torfinn Buseth and Bjørn Johan Arntzen

Abstract

Metallurgical silicon and its alloys are essential in several industries, such as solar energy, automotive, aerospace, and steel production. However, silicon dust, generated during silicon production, processing, and handling, poses significant health and safety hazards. Dust extraction systems control these risks by capturing, transporting, and removing dust particles from the work environment, thereby improving air quality for personnel, and reducing the accumulation of dust deposits.

This study investigates the hazards associated with dust explosions in dust extraction ducts. It measures explosion pressures inside pipes and observes the length of emitted fireballs. Experiments were conducted using an explosion vessel and pipes of three different internal diameters, with expanders and reducers utilized to create pipe configurations of both diminishing and increasing diameters, simulating a small-scale dust extraction system. The dusts used in the experiments were silicon and silicon-alloy dusts, with dust layers representing nominal dust concentrations ranging from 250 to 5000 g/m³. Piezoelectric pressure transducers recorded pressure development at specific locations inside the pipes, while a high-speed camera captured the fireball length emitted from the pipe ends.

Experiments involving single pipes and configurations of two connected pipes revealed a strong correlation between dust layer concentration and fireball length. However, no evidence suggested a relationship between explosion pressure and dust layer concentration. A 25-metre configuration with four connected pipes of varying diameters, with the smallest pipes near the exit, demonstrated that silicon dust, formally classified as St-1 dust, although on the limit to St-2, can result in detonation-like overpressures and shock wave speeds. Further research is needed to determine whether and under which conditions a silicon dust deflagration may transition into a self-sustained detonation.

Acknowledgements

This master's thesis is submitted in partial fulfilment of a five-year integrated master's program in Energy at the University of Bergen, leading to the degree of Master of Science. The Geophysical Institute administers the program, while the thesis work was conducted at the Department of Physics and Technology. The primary focus of this thesis is process safety, specifically examining dust explosions in dust extraction systems through experimental research.

I extend my deepest gratitude to my supervisor, Trygve Skjold. His course, «Explosion Hazards in the Process Industries», sparked my interest in dust explosions, and his guidance has been invaluable throughout this thesis—both academically and during late-night sessions in the university workshop. I also wish to sincerely thank my lifelong friend and study partner, Anders Bjørnsen, for his support and camaraderie throughout this academic journey.

Further, I express my appreciation to Torfinn Buseth at Elkem ASA for defining the scope of this thesis and his genuine enthusiasm for process safety. Without Elkem's financial support, our experiments would not have been feasible. I am also grateful to Roald and Charles for their generosity in allowing us to utilize all facilities at the university workshop and for their continuous help and assistance.

In addition, I extend my gratitude to PhD fellow Matthijs van Wingerden for his invaluable guidance with the instrumentation used in the experiments and his software assistance regarding C-J velocity calculations. I would also like to thank Gexcon AS, particularly the team at Gexcon Steinsland, for granting access to their test field and assisting us in the experimental set-up.

I also wish to express my appreciation to Bjørn Johan Arntzen, who took on the role of co-supervisor. His feedback and guidance have been valuable in the final stages of this work.

Lastly, I want to convey my profound gratitude to my girlfriend and my parents for their unwavering love and support during this intense period. Their encouragement has been a cornerstone of this accomplishment.

Disclaimer

Considering the extensive scope of the experimental work in this thesis, conducting all experiments alone would have been infeasible. Therefore, large-scale, and laboratory-scale experiments were carried out in partnership with my fellow student, Anders Bjørnsen (2023).

Throughout these experiments, we used three distinct types of dust. The data collected from the Silgrain MC (Si) was shared between us, while the data for the other two types of dust were split. The experimental collaboration and the shared data collection approach means there will be notable similarities in the 'Method' sections of both theses and identical results for experiments involving Silgrain MC (Si). Therefore, any discrepancies or differences in the interpretation of the results should be attributed to our individual analysis of the shared data, rather than differences in the experimental data itself.

Table of Contents

List of Figures

List of Tables

Nomenclature

Symbols	Description	Unit
c	Speed of sound	$m \cdot s^{-1}$
d	Tube diameter	m
$D_{C\text{-}J}$	Chapman-Jouguet detonation velocity	$m \cdot s^{-1}$
d_{ct}	Critical tube diameter for detonation transmission	m
d_{cp}	Critical diameter of detonation propagation	m
$\left(\frac{dP}{dt}\right)$	Rate of pressure rise	$bar \cdot s^{-1}$
$\left(\frac{dP}{dt}\right)_{max}$	Maximum rate of pressure rise	$bar \cdot s^{-1}$
K_{st}	Deflagration index	$bar \cdot m \cdot s^{-1}$
M	Molar mass	$kg \cdot mol^{-1}$
m	Mass	kg
$m_{\%}$	Mass percentage	%
n	Number of moles	mol
P	Absolute pressure	bar
P_{ci}	Overpressure due to chemical ignitors	bar
$P_{C\text{-}J}$	Chapman-Jouguet detonation Pressure	bar
P_{ex}	Explosion overpressure	bar
P_m	Corrected explosion overpressure	bar
P_{max}	Maximum explosion overpressure	bar
Q	Heat release	$J \cdot kg^{-1}$
Q^*	Thermal radiation energy	$W \cdot m^{-2}$
R	Universal gas constant	$J \cdot mol^{-1} \cdot K$
T	Absolute temperature	K
V	Volume	m^3
$V_{\%}$	Volume percentage	%
V_D	Volume displacement	m^3
V_f	Volume fraction	—
V_S	Total system volume	m^3

Greek Symbols	Description	Unit
β	Fraction evaporated at adiabatic flame temperature	—
γ	Heat capacity ratio	—
λ	Detonation cell size	m
ρ	Density	$kg \cdot m^{-3}$
σ	Stefan-Boltzmann constant	$W \cdot m^{-2} \cdot K^{-4}$

Abbreviations	Description	Unit
Barg	Bar gauge	bar
C-J	Chapman-Jouguet	—
DDT	Deflagration-to-detonation transition	—
DN	Diameter nominal	mm
FAT	Flame acceleration tube	—
FSM	Ferrosilicon magnesium	—
ID	Inner diameter	mm
LEL	Lower explosive limit	$g \cdot m^{-3}$
LOC	Limiting oxygen concentration	$V_{\%}$
OD	Outer diameter	mm
UEL	Upper explosive limit	$g \cdot m^{-3}$
UiB	University of Bergen	—

1 Introduction

This chapter outlines the motivation and aim of the thesis. It sheds light on the potentially devastating consequences of metal dust explosions and presents various prevention and mitigation strategies.

1.1 Motivation

Dust explosions represent a significant hazard within various industries where fine particles of combustible material are processed. Their ability to inflict catastrophic damage, disrupt operations, and pose a threat to human safety underscores the urgency and significance of studying this phenomenon. Dust explosions occur when a combustible dust cloud in the atmosphere encounters an ignition source. Numerous factors, including dust concentration, particle size, dispersion conditions, confinement, and the presence of oxidants, influence the severity and propagation of dust explosions. Under the right conditions, an initial or primary explosion can stir up more dust into the air. If this dust is ignited, a secondary explosion, often far more destructive, can ensue, leading to substantial damage and potential loss of life. Figure 1 illustrates the components necessary for a dust explosion to occur.

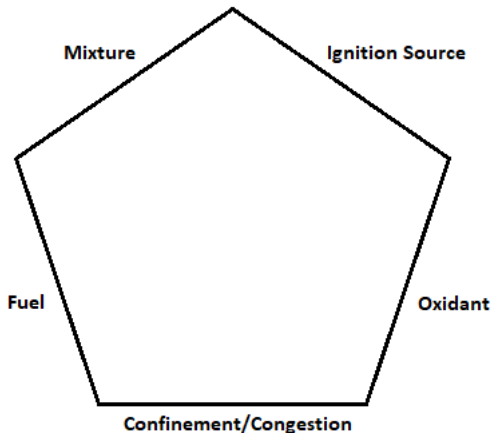

Figure 1: The explosion pentagon (Kauffman, 1982)

Metallurgical silicon and silicon alloys are fundamental to many industries, from solar energy to automotive and aerospace. In the solar energy sector, for example, high-purity metallurgical silicon is a critical precursor for the productions of solar-grade silicon, which is utilized in the fabrication of monocrystalline and multicrystalline solar cells. These cells are integral components of photovoltaic modules.

In the automotive and aerospace industries, aluminium-silicon alloys, known for their lightweight and heat-resistant properties, are extensively used. Components manufactured from these alloys significantly reduce vehicle weight, improving fuel efficiency and overall performance. In addition, silicon alloys, including ferrosilicon and ferrosilicon-magnesium, enhance steel and cast iron's strength, durability, and corrosion resistance. Such alloys are crucial in various industries, such as construction, automotive, and aerospace, contributing to developing robust structures and components.

While silicon and silicon alloys play a critical role in numerous applications, their production and processing also come with certain safety challenges. A notable safety challenge is the generation of combustible silicon dust during various stages of production, such crushing and processing, and material handling and transport. This dust poses a significant health hazard to workers and is an explosion hazard if accumulated in deposits. Figure 2 shows a dust layer on top of a dust extraction duct and dust deposits inside a dust extraction duct at a former crushing plant at Elkem Bjølvefossen. (NB, it is important to note that a new dust extraction system has been built, and that the system featured in the figure is no longer in operation).

Figure 2: Dust layer on top of dust extraction duct (left). Dust deposits inside dust extraction duct (right). Bjølvefossen 9. June 2022.

Process plants employ dust extraction systems to control the hazards associated with hazardous dust in the workplace. These systems capture, transport, and remove dust particles from the work environment, mitigating the risk of inhalation and reducing the risk of dust accumulation. The ductwork, consisting of ducts of varying lengths and diameters, forms a vital aspect of these dust extraction systems. Illustration of the duct work for the old dust extraction system at Elkem Bjølvefossen can be seen in Figure 3.

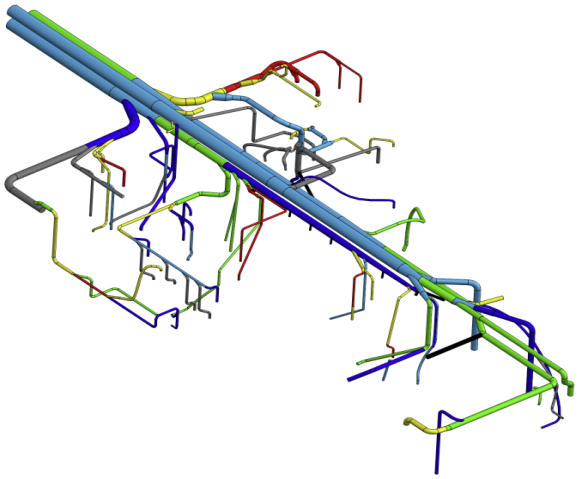

Figure 3: Illustration of dust extraction duct work at the old crushing plant at Elkem Bjølvefossen (T. Buseth, personal communication, 28. April 2022).

Ductwork is crucial for connecting different system components and facilitating the transport of particle-laden air from the hoods to the filtration or collection unit. Factors such as plant layout, number of capture points, airflow requirements, and system pressure losses influence the duct lengths and diameters, resulting in a complex system of various dimensions. Swedish incident statistics indicate a high rate of dust-related incidents involving dust collectors, ventilation ducts, extraction ducts, and filters. As illustrated in Figure 4, statistics from 2012 to 2017 on metal dust incidents within the Swedish metalworking industry demonstrates the vulnerability of dust extraction systems to such occurrences.

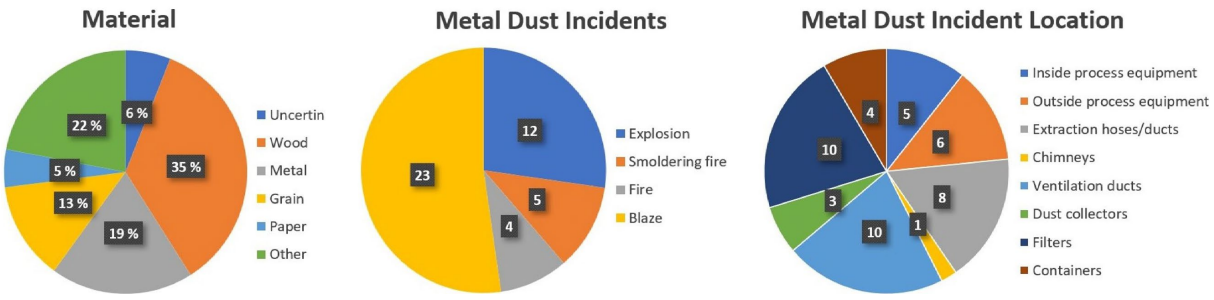

Figure 4: Dust explosion incident statistics in Sweden 2012-2017 (Nessvi & Persson, 2019).

The motivation for this master thesis is to enhance our understanding of dust explosions in dust extraction systems and to contribute with scientific data that can help develop strategies to mitigate the risk of such events. The motivation for this research can be divided into three key aspects: safety, economic considerations, and scientific advancement.

Safety

The primary motivation for this study is to prevent accidents and enhance safety in industries that deal with combustible dust. Dust explosions can lead to fatalities, structural damage, and equipment loss. By understanding the underlying mechanisms and factors contributing to these explosions, this study aims to develop more effective preventive measures to safeguard workers' well-being and protect industrial facilities.

Economic considerations

Dust explosions can result in significant financial losses due to the destruction of property, equipment, and inventory. In addition, production downtime, loss of market share, and compensation claims can further exacerbate the economic impact. By investigating the causes and dynamics of dust explosions in pipes and ducts, this study aims to contribute to the development of cost-effective solutions that will minimize the economic burden associated with such events.

Scientific advancement

Although much research has been conducted on dust explosions, the specific challenges and complexities associated with dust extraction systems and ventilation ducts demand further investigation, particularly in the context of interconnected pipes with varying dimensions. This study aims to expand the current understanding of dust explosion dynamics in dust extraction systems. By advancing the scientific knowledge in this area, the findings from this thesis can help contribute to the development of more effective explosion protection strategies and technologies.

In conclusion, this master's thesis is motivated by the desire to improve safety, minimize economic losses, and expand the scientific understanding of dust explosions in pipes, dust extraction systems, and ventilation ducts. The findings from this research could influence the future design of dust extraction systems in industries that handle combustible dust, ultimately resulting in safer and more sustainable operational environments.

1.2 Incidents Involving Metal Dusts

This section will present two incidents involving metal and metalloid dusts that are particularly relevant to the subject of the thesis.

1.2.1 Silicon Dust Explosion in Bremanger

In 1972, a severe dust explosion occurred at a silicon smelting plant in Bremanger, Norway, leading to the loss of five lives and significant injuries for four additional workers (Eckhoff, 2016). The explosion occurred in the plant's milling section, causing substantial damage to the process equipment and the factory building. Witnesses reported that the flame was exceptionally bright, almost white, which is consistent with the high temperatures of silicon dust flames. The intense thermal radiation from the flame contributed to the severity of the burns suffered by the nine workers.

The investigation following the accident revealed a small hole in a steel pipe used to transport silicon powder from a mechanical sieve to a silo below. An oxygen/acetylene cutting torch with both valves open was discovered on the floor about 1 metre from the pipe with the hole. Evidence suggests that the cutting torch made the hole just before the explosion occurred.

At the time of the explosion, part of the plant was shut down for various repairs, but the dust extraction system was still in operation. This could partly explain the rapid spread of the explosion throughout the entire plant. Likely, the internal pipe wall had not been cleaned before the perforation. Given the high temperature and intense thermal power of the cutting torch and the oxygen supply it provided, a layer of fine dust on the internal pipe wall may have been dispersed and ignited as the gas flame burned through the pipe wall. The subsequent blast from the primary silicon dust explosion then lifted dust deposits in other areas of the plant, allowing the explosion to propagate further until it ultimately engulfed the entire silicon grinding building.

1.2.2 Aluminium-Alloy Dust Explosion in China

On August 2, 2014, a massive dust explosion occurred at Kunshan Zhongrong Metal Products Co., Ltd., in Kunshan, Jiangsu province, China (Li et al., 2016). The explosion resulted in 146 fatalities and more than 100 injuries, making it one of the deadliest industrial accidents in China's history.

The factory specialised in polishing different types of metal parts. When the explosion occurred, the factory was polishing aluminium-alloy wheel hubs for the automaker Industry. This process generated a lot of very fine aluminium-alloy dust as a by-product. This dust was highly flammable and accumulated in the factory due to inadequate ventilation and dust control measures.

When aluminium-alloy dust encounters water or moisture, an exothermic reaction can occur (Eckhoff & Li, 2021). This reaction generates heat, which may be enough to lead to the auto-ignition of the dust. In the case of the Kunshan explosion, it is believed that this reaction transpired within a dust-collecting barrel connected to the dust extraction system. The barrel was situated outdoors and was exposed to moisture. Over time, this exposure led to corrosion, creating a hole in the barrel, and allowing its contents to come into contact with moisture.

Once ignited, the fire spread through the dust extraction ducts and emerged from the dust extraction hoods situated above all the worktables on the first floor of the plant, this led to a secondary explosion triggered by the ignition of dust deposits on the floor and around the production lines. The secondary explosions caused the fire to rapidly spread throughout the factory's first floor and be drawn into the dust-extraction hoods, resulting in a massive filter explosion. Furthermore, the explosion spread to the factory's second floor through a staircase, leading to the fire engulfing the entire second floor as well.

1.3 Dust Explosion Prevention and Mitigation

Dust explosions are a significant concern in various industries, including agriculture, food processing, metalworking, and woodworking. They occur when combustible dust particles suspended in the air ignite, resulting in a rapid and destructive release of energy. Preventing and limiting dust explosions is essential for ensuring the safety of employees, protecting property, and preventing costly business interruptions. Hierarchy of principles for risk reduction: inherent safety, prevention, mitigation, and procedural safety.

Inherent Safety

Inherent safety is a proactive approach to engineering and design that emphasises identifying, eliminating, or minimising hazards by incorporating fundamental safety principles during the initial stages of design (Kletz & Amyotte, 2010). This approach contrasts with more traditional safety measures, which rely on protective systems, devices, or procedures to manage risks. Trevor Kletz introduced the concept of inherent safety in the 1970s as a method for improving process safety in the chemical industry. It has since been extended to other fields, such as nuclear power plants, transportation systems, and manufacturing. Inherent safety is based on four main principles (Kletz & Amyotte, 2010):

- *Minimise*: This principle involves reducing the amount of hazardous material present at any time, such as using smaller batches. Decreasing the number of hazardous substances minimises the potential for accidents or harmful incidents, leading to a safer working environment.
- *Substitute*: This principle advocates for replacing hazardous materials with less hazardous alternatives, for example, using water and detergent instead of a flammable solvent for cleaning purposes. Substituting less hazardous materials can reduce the risks associated with handling, storing, and using the substance.
- *Moderate:* This principle aims to reduce the strength of an effect by altering the conditions in which hazardous materials are used. Examples include using a cold liquid instead of a high-pressure gas or employing a diluted solution rather than a concentrated form. Modifying the conditions can reduce the likelihood and severity of accidents or incidents.

- *Simplify:* This principle focuses on eliminating problems through thoughtful design rather than adding extra equipment or features to address them. Simplification involves only using complex procedures when necessary. Simplifying systems and processes reduces the potential for human error or equipment failure, leading to safer operations.

Implementing inherent safety principles requires a comprehensive understanding of the potential hazards and risks associated with a given system or process. This involves conducting hazard identification studies, risk assessments, and other analyses to identify potential sources of harm and determine the most effective ways to eliminate or minimise those hazards through design choices.

Prevention

Prevention of explosible atmosphere (Eckhoff & Li, 2021):

- *Inertisation:* Adding inert gas to the atmosphere to limit oxygen concentration is a proven method for preventing dust explosions in various industrial processes. By maintaining the oxygen concentration below the limiting oxygen concentration (LOC), self-sustained flame propagation is not possible, reducing the risk of dust explosions. Inert gases, such as carbon dioxide, water vapour, nitrogen, and rare gases like argon, are used for this purpose because they do not support combustion. The selection of the appropriate inert gas depends on factors like availability, cost, and compatibility with the process or materials involved.

  In coal mines, inert dust is employed to establish an environment that prevents dust explosions from propagating into secondary explosions. This is achieved by ensuring adequate amounts of stone dust are present as a layer on the mine gallery floor or on shelves and other surfaces. The initial blast, which always precedes the flame in a dust explosion, will disperse both the stone and coal dust simultaneously, forming non-combustible dust mixtures in the air. As a result, when the dust flame reaches these mixed clouds, it is extinguished. In industries other than mining, the addition of inert dust is rarely applied due to concerns regarding product contamination and other issues.

- *Maintaining dust concentration outside the explosive range:* Consistent and thorough housekeeping is vital in minimizing dust accumulation. The establishment of a cleaning schedule that encompasses routine cleaning and comprehensive deep cleaning to eliminate dust from surfaces, equipment, and inaccessible areas. Utilize cleaning techniques that prevent dust from becoming airborne during the cleaning process. Maintaining dust concentrations below explosive levels to prevent dust explosions can be challenging. Dust concentrations within process equipment often fluctuate unpredictably and uncontrollably, particularly during accidental dust explosions.

Prevention of ignition sources (Eckhoff & Li, 2021):

- *Open flames/hot gases:* Enforcing proper organizational procedures and routines can avoid most open flame ignition sources, such as prohibiting smoking, lighters, matches, and implementing strict procedures for hot work.
- *Hot surfaces:* Hot surfaces can be intentional (e.g., heaters, dryers, steam pipes) or unintentional (e.g., engines, blowers, fans, mechanical conveyors, mills, mixers, bearings, unprotected light bulbs) and pose a risk of ignition. In order to reduce the likelihood of ignition caused by hot surfaces, it is essential to adopt appropriate design and maintenance procedures, including using heat-resistant materials, ensuring sufficient ventilation, and carrying out routine inspections to detect any potential hazards.
- *Smouldering nests:* Detecting infrared radiation and extinguishing smouldering nests during pneumatic transport can prevent fires and explosions in downstream equipment. Water is commonly used as an extinguishing agent, applied as a fine mist.
- *Mechanical impact:* Mechanical impacts can produce two types of potential ignition sources: flying fragments/particles of burning material and hot-spots where the impacting bodies touch. Preventing ignition from mechanical impacts requires proper equipment design and maintenance.
- *Electric sparks and arcs and overheating caused by electrical equipment:* Electric sparks and arcs can result from equipment malfunction, improper installation, or failure to follow safety guidelines. They can ignite dust clouds, leading to dust explosions. Preventing electric sparks and arcs involves:

i. Proper grounding and bonding of equipment to minimize static electricity build-up.
ii. Installation of electrical equipment that complies with explosion protection standards.
iii. Routine inspection and maintenance of electrical systems to detect and correct any defects.

- *Overheating:* Overheating of electrical equipment can lead to fires and the ignition of dust clouds. Preventive measures include:
  i. Ensuring equipment is properly rated for the intended use and installed according to the manufacturer's guidelines.
  ii. Implementing a regular maintenance program to inspect and maintain equipment.
  iii. Implementing temperature monitoring and alarms to detect overheating.

Mitigation

If an explosion occurs, there are several methods to mitigate the consequences (Eckhoff & Li, 2021).

- *Explosion venting* is a passive method to release the pressure generated during a dust explosion. Properly designed vents allow pressure to dissipate, preventing equipment damage and minimizing the risk of a secondary explosion. Key factors in designing explosion vents include vent size, location, and the use of flame arrestors or quenching systems to prevent flames from escaping.
- *Explosion suppression* systems are active methods designed to detect and extinguish a dust explosion in its early stages. These systems use sensors to detect the initial pressure increase and activate a suppressant release system, typically using water, foam, or a dry chemical suppressant. This rapidly extinguishes the flame and limits pressure development, preventing equipment damage and secondary explosions.
- *Explosion isolation* systems are designed to prevent the propagation of a dust explosion from one part of a process to another. They include mechanical barriers, such as rotary airlock valves and rapid-acting gates, which close to block the path of an explosion, and chemical barriers, which use extinguishing agents to quench the flame.

Proper design, installation, and maintenance of these systems are critical to their effectiveness.

Procedural safety

Employees should be trained in the hazards associated with combustible dust and the specific risks present in their workplace (Eckhoff, 2016). Training should cover the following:

- Recognition of combustible dust hazards and conditions that can lead to dust explosions.
- Proper handling, storage, and disposal of combustible dust to minimize risk. Safe operating procedures, including the use of appropriate personal protective equipment.
- Emergency response procedures in the event of a dust explosion, including the use of fire suppression equipment and evacuation plans.

1.4 Aim of the Thesis

The primary objective of this master thesis is to enhance safety by advancing our understanding of dust explosions, specifically, those involving silicon and silicon-alloy dust, in ventilation ducts and dust extraction systems. To achieve this, the research will examine explosion characteristics and fireball dynamics by analysing explosion pressure and fireball length across a range of experimental setups, incorporating pipes of varying lengths and diameters. Through a deeper understanding of the governing mechanisms and contributing factors behind dust explosion behaviour, this study aims to provide valuable insights that can inform the development of more effective dust explosion prevention and mitigation strategies within the silicon and silicon-alloy processing industries.

2 Theory and Previous Work

This chapter introduces relevant theory and previous work.

2.1 Definitions and Basic Concepts

This section elucidates relevant definitions and fundamental concepts.

2.1.1 Combustion

Combustion is a complex process and is not straightforward to define. However, a commonly used explanation is that combustion is an exothermic chemical reaction that occurs when a fuel reacts with an oxidising agent. This chemical reaction results in the production of heat and products:

fuel + oxidizer → products + heat

As an example, the total reaction for the combustion of silicon (Si) be represented as (Lide, 2006):

Si (s) + O_2 (g) → SiO2 (s) + 911 kJ/mol

The combustion process involves several steps, including initiation, propagation, and termination. In the initiation step, a source of energy (e.g., a spark or flame) is needed to start the reaction. In the propagation step, the reaction spreads throughout the fuel and oxidiser mixture, releasing more energy. Finally, in the termination step, the reaction slows down and stops as the fuel and oxidiser are depleted. The combustion rate depends on several factors, including the availability of oxidiser, the system's temperature, and the fuel's physical characteristics, such as composition and particle size. These factors affect the reaction's kinetics and hence the rate of energy release.

Combustion of Dust Particles

The nature of the combustion of solid materials is influenced by the degree of subdivision of the combustible material (Eckhoff, 2016). Any substance capable of burning in air will combust more rapidly and violently as the degree of subdivision increases. The rationale behind this phenomenon is that when a material is broken down into smaller fragments, the surface area that can interact with oxygen expands considerably.

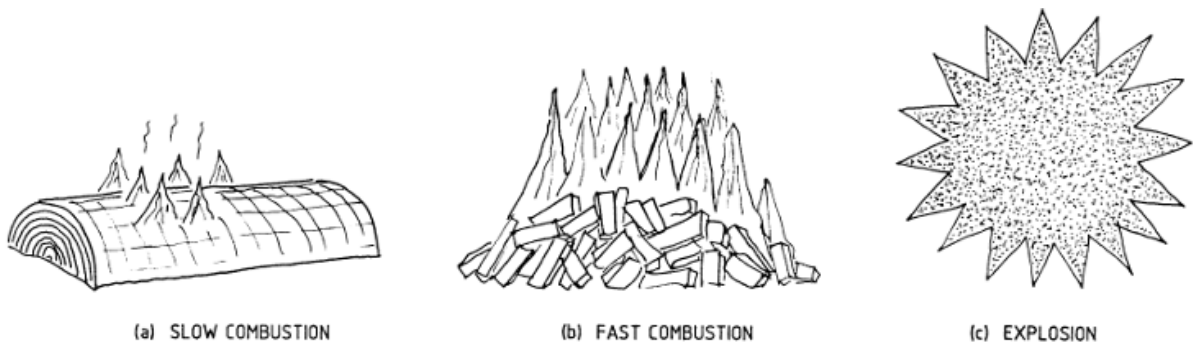

Figure 5: Illustration of the impact of increasing subdivisions on combustion rate (Eckhoff, 2003).

Heterogenous and Homogenous Combustion

Heterogeneous and homogeneous combustion are two distinct types of combustion processes that differ based on the phases of the reactants and their interaction during the reaction (Glassman & Yetter, 2008).

Heterogeneous combustion is a combustion process that involves reactions at the interface of different phases, typically solid or liquid fuel and gaseous oxidizer. This type of combustion is characterized by a series of steps, including heat transfer, mass transfer, and surface reactions (Glassman & Yetter, 2008). These steps are explained below:

- *Heat transfer*: Heat is transferred from the high-temperature gaseous environment to the surface of the solid or liquid fuel. This transfer occurs via conduction, convection, and radiation.
- *Mass transfer*: The oxidizer diffuses from the gas phase to the fuel surface, while gaseous fuel products diffuse from the surface. The concentration gradients between the fuel and oxidizer drive this mass transfer.

- *Surface reactions*: The oxidizer reacts with the fuel at the surface, either through chemical reactions or physical processes like adsorption, desorption, and surface diffusion. The surface reactions can involve heterogeneous catalysis or direct oxidation of the fuel.

The rates of heat transfer, mass transfer, and surface reactions influence the rate of heterogeneous combustion. The complexities arise from the fact that these processes are often interconnected, and the overall combustion rate may be limited by any one of them. Moreover, heterogeneous combustion can involve multi-step reactions and alterations in the fuel's physical properties (such as melting, evaporation, or pyrolysis), which add further intricacy to the process.

Homogeneous combustion, on the other hand, occurs when fuel and oxidizer are in the same phase (typically gaseous) and react throughout the entire volume of the mixture. There is no mass transfer limitation in this case, as the fuel and oxidizer are already mixed. The steps involved in homogeneous combustion are (Glassman & Yetter, 2008):

- Mixing: To achieve a combustible mixture, the fuel and oxidizer must be mixed appropriately. Depending on the application, this mixing can be achieved by turbulent or laminar flow.
- Ignition: The mixture is ignited by an external energy source, such as a spark, flame, or hot surface. The ignition initiates a series of chain reactions, leading to the formation of reactive radicals and intermediate species.
- *Combustion*: The chain reactions continue to propagate throughout the mixture, leading to the conversion of the fuel and oxidizer into combustion. The process continues until the reactants are consumed, or the reaction is quenched by heat loss or dilution.

The chemical kinetics of the reactions and the spatial distribution of the reactants in the mixture primarily determine the homogeneous combustion rate. However, temperature and pressure also play important roles, as they can affect reaction rates and radical concentrations.

Heat of Combustion

Heat of combustion, also known as the enthalpy of combustion or calorific value, is a measure of the amount of energy released during the complete combustion of a specific amount of a substance, typically a fuel, in the presence of an oxidiser like oxygen (Atkins et al., 2018). The heat of combustion is typically expressed in units of energy per mass, such as joules per gram (J/g) or kilojoules per mole (kJ/mol).

In a combustion reaction, the fuel reacts with the oxidiser. Consequently, it generates combustion products like carbon dioxide and water vapor for organic dusts, and metal oxides for metallic dusts, along with a release of energy in the form of heat. This energy release results from breaking the chemical bonds in the reactants and forming new chemical bonds in the products.

Metals generally have higher enthalpy release than organic materials (Glassman & Yetter, 2008). This difference in enthalpy, or heat of combustion, arises from the nature of the chemical bonds in metals and organic compounds. Organic compounds predominantly contain carbon and hydrogen atoms bound together by covalent bonds. During the combustion of organic materials, these bonds are broken, and new bonds are formed with oxygen to create products like carbon dioxide and water. On the other hand, metals consist of metal atoms arranged in a lattice structure, held together by metallic bonds. These bonds result from the attraction between positively charged metal ions and the negatively charged «sea» of free electrons in the metal lattice (Kittel, 2005). Metals, including those which are combustible such as magnesium and aluminium, can react with oxygen to form metal oxides. The heat of combustion of metals is generally higher than that of organic materials because metallic bonds are generally stronger and require more energy to break.

Combustion of Silicon and Ferrosilicon Magnesium

Silicon, a metalloid, has properties between those of metals and nonmetals. While it is not a metal, it does have some metallic characteristics (*Smithells Metals Reference Book*, 1998). For example, silicon has a crystalline structure similar to metals and is a good conductor of heat. The combustion of silicon forms silicon dioxide (SiO_2), a reaction with a relatively high enthalpy of combustion compared to many organic materials. The standard enthalpy of formation for SiO_2 is -911 kJ/mol (Lide, 2006). For comparison, the standard enthalpy of formation for CO_2, a common product from combustion of organic material, is -393.5 kJ/mol (Lide, 2006).

Silicon particle combustion is a complex process involving both homogeneous and heterogeneous reactions, which can occur sequentially or simultaneously depending on factors such as particle size, temperature, pressure, and the composition of the surrounding environment (Futko et al., 2019; Schei et al., 1998).

Initially, heterogeneous combustion prevails as solid silicon particles react with the surrounding oxygen, generating heat at the solid-gas interface. This exothermic reaction results in the formation of silicon dioxide (SiO_2), which creates an oxide layer on the silicon particle surface, acting as a diffusion barrier and restricting oxygen access to the unreacted silicon core. The reaction rate is governed by oxygen diffusion through the SiO_2 layer and the oxygen availability at the reaction front, leading to a more intricate and uneven combustion process.

As the reaction advances and temperatures increase, some silicon particles vaporize, forming gaseous silicon monoxide (SiO) when the SiO_2 layer is reduced by unreacted silicon at higher temperatures. This endothermic reaction consumes some of the energy released during the initial exothermic reaction. Gaseous SiO reacts with oxygen in the gas phase, initiating a homogeneous combustion process. This results in a more uniform temperature distribution and steadier flame propagation due to the efficient mixing of reactants and consistent heat release.

Between 1300 K and 2000 K, Si combustion produces gaseous SiO, which reacts with oxygen in the combustion process to form SiO_2 and Si (Broggi et al., 2019). SiO combustion further increases the combustion temperature. SiO sublimates at 2070 K (Broggi, 2021), resulting in a

greater volatilization rate. When SiO (g) is rapidly cooled, it produces a brown condensate consisting of SiO_2 and Si (Broggi et al., 2019). This brown condensate is often seen in fuel rich combustion of Si.

Cashdollar & Zlochower (2007) recorded the flame temperature of silicon dust particles with a median diameter of four micrometres as 2300 ± 100 K. They also computed the adiabatic flame temperature as 3240 K and, based on this, calculated that the evaporation fraction, β, was above unity, suggesting homogeneous combustion at this temperature. The results obtained for silicon (Si), iron (Fe), and magnesium (Mg) from their study are presented in Table 1. These findings suggest that magnesium combustion may be more homogeneously driven compared to silicon. The combustion of iron particles has primarily been identified as a heterogeneous reaction (Guo et al., 2022). However, if iron particles combust alongside silicon and magnesium, which exhibit higher flame temperatures than iron, this might potentially promote a shift towards a higher degree of homogenous combustion.

Table 1: Median particle size, adiabatic flame temperature, evaporation fraction, and pyrometric temperature for Si, Fe and Mg (Cashdollar & Zlochower, 2007).

Dust	D50 (µm)	$T_{ad,max}$ (K)	β	$T_{Pyrometer}$ (K)
Si	4	3240	> 1	2300 ± 100
Fe-1	4	2490	> 1	1800 ± 50
Fe-2	45	2490	0.3	1600 ± 100
Mg	16	3610	≫ 1	2800 ± 100

In the solidification process of silicon and silicon-alloys, intermetallic phases can form due to varying cooling rates, composition gradients, and specific alloying elements. These intermetallic phases exhibit different structural, mechanical, and thermal properties than the parent material, which can significantly affect the performance of the alloy. In addition, the formation of these phases directly impacts the ignition and combustion properties of the material. For instance, they can alter the ignition temperature and combustion rate, influencing the alloy's behaviour under specific operational conditions. This thesis has not delved into the specifics of the ignition and combustion properties of these intermetallic phases within silicon or silicon alloys.

Stoichiometry

The stoichiometric value refers to the ideal proportion of fuel and air required for a complete combustion reaction. In this perfect mixture, all fuel reacts with the available oxygen in the air, leaving no unburned fuel or excess oxygen after the combustion process. Dust particles displace volume; however, this displacement is negligible concerning the dust layer concentrations used in this thesis. This is demonstrated by calculating the volume fraction for a concentration of 1000 $g \cdot m^{-3}$ with silicon, in 1 m^3 of air using the density of Si provided by Lide (2006). Equation 1, where V is volume, m is mass, and ρ is density, and Equation 2, where V_f is the volume fraction, V_D is the volume displacement, and V_S is the system volume, are presented below to further illustrate this point.

$$V = \frac{m}{\rho} \qquad \textit{Eq. 1}$$

$$V_f = \frac{V_D}{V_S} \qquad \textit{Eq. 2}$$

$$V = \frac{1\ kg}{\frac{2329.6\ kg}{m^3}} = 4.29 \cdot 10^{-4}\ m^3$$

$$V_f = 4.29 \cdot 10^{-4}$$

As a result, the stoichiometric values for silicon will be determined without accounting for the displacement from the dust particles. Since the number of moles of silicon would equal the number of moles of oxygen in a stoichiometric mixture the ideal gas law (Eq. 3) can be employed to calculate the number of moles. The number of moles, n, of oxygen in 1 m^3 of air, can be calculated with the volume, V, the pressure, P, the temperature, T, and the universal gas constant, R:

$$PV = nRT \qquad \textit{Eq. 3}$$

$$n_{O_2} = 0.21 \cdot \left(\frac{101300\ Pa \cdot 1m^3}{\frac{8.314\ J}{molK} \cdot 298\ K} \right) = 8.59\ mol$$

Silicon has a molar mass of 28.084 g/mol (Lide, 2006), and given 8.59 moles oxygen, this results in the following concentrations listed in Table 2.

Table 2: Stoichiometric concentration for silicon in 1 m^3 of air

Stoichiometric concentration SiO (g/m^3)	Stoichiometric concentration SiO_2 (g/m^3)
241.2	482.4

2.1.2 Explosion

According to Eckhoff (2016, p. 2), the definition of an explosion can vary and generally falls into two main categories. The first category focuses on the noise or «bang» resulting from the sudden release of a powerful pressure wave or blast wave, regardless of whether the wave's origin is a chemical or mechanical energy release. This definition corresponds with the primary meaning of the word «explosion» as a sudden outburst.

The second category of definitions is restricted to explosions that arise from the sudden release of chemical energy, including the explosions of gases, dusts, and solid explosives. In this context, the emphasis is on the chemical energy release itself, and the definition of an explosion reflects this aspect accordingly. For example, one potential definition can be, «An explosion is an exothermic chemical process that leads to a sudden and significant increase in pressure when it occurs at a constant volume». The choice of definition depends on the context, whether the focus is on the cause or the effect of the explosion.

Primary and Secondary Dust Explosions

In industrial settings, primary dust explosions typically take place within process equipment and are often relatively small (Casal, 2018). Despite their smaller scale, these primary explosions generate considerable turbulence inside the confined space where they occur. This turbulence can unsettle and suspend accumulated dust in the vicinity or inside another piece of equipment, forming a new, larger combustible dust cloud. Secondary explosions are frequently more powerful than primary ones, as they often have greater access to both combustible materials and oxygen. The intensified blast from secondary explosions can result in extensive damage to equipment, facilities, and personnel. A secondary explosion is illustrated in Figure 6 with a primary explosion rupturing a piece of process equipment, resulting in the dispersion and ignition of a second dust cloud.

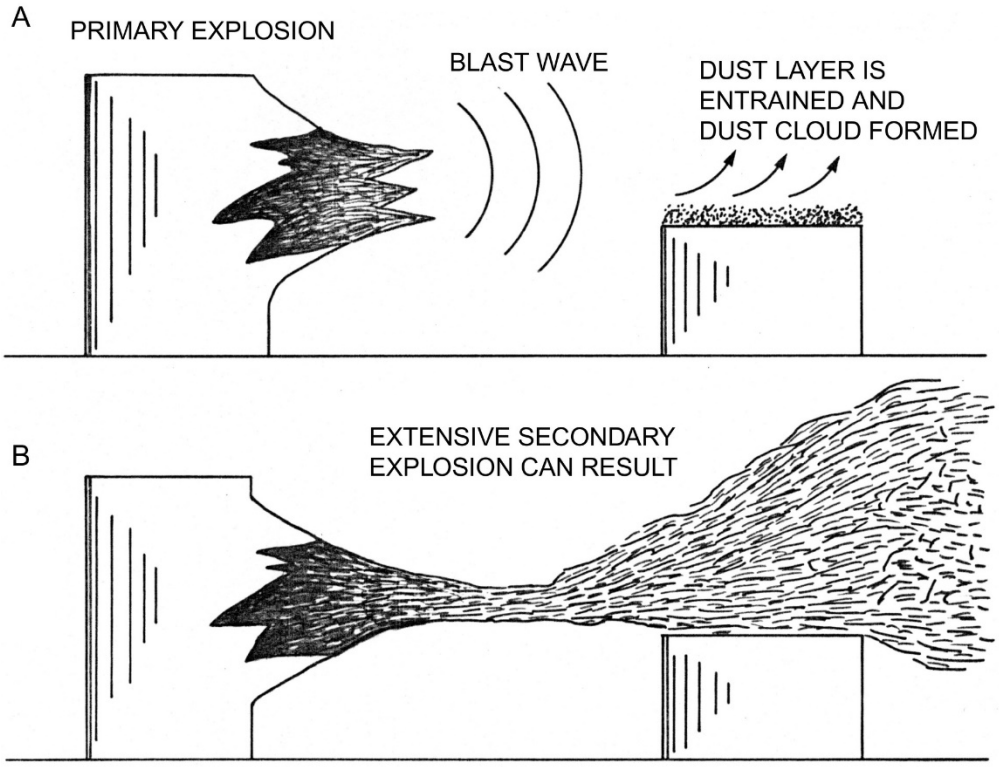

Figure 6: Secondary dust explosion resulting from a primary explosion within process equipment (Eckhoff, 2003).

Figure 7 illustrates how a thin dust layer can result in a combustible dust cloud when dispersed in air, and how the dust cloud concentration changes with dispersion height.

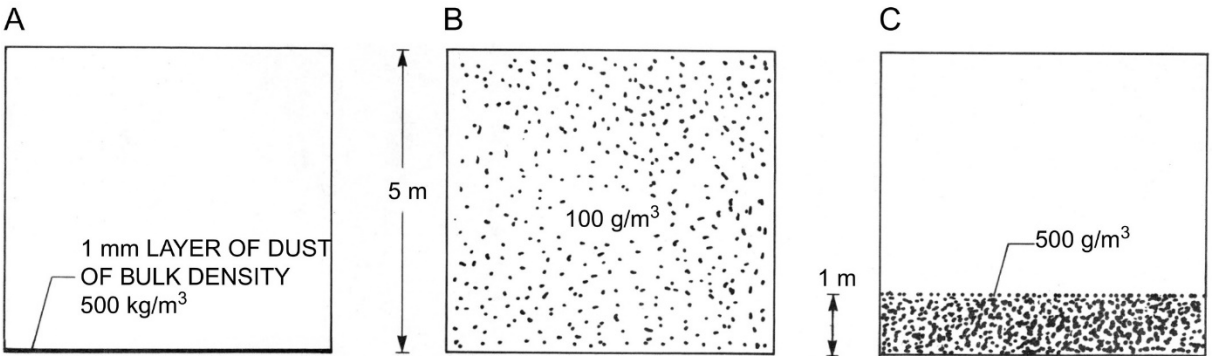

Figure 7: Dust cloud concentration at different hights, resulting from dispersion of a thin dust layer (Eckhoff, 2003).

Explosibility Limits

The lower explosive limit (LEL) is an essential parameter in combustion and fire safety research. It represents the minimum concentration of a flammable substance in a mixture with air, below which the mixture becomes too lean to sustain a flame or cause an explosion when exposed to an ignition source (Eckhoff, 2003).

For dust, the LEL is usually expressed in mass concentration units, such as grams per cubic metre. LEL for dust indicates the minimum mass of the combustible dust suspended in a unit volume of air required to propagate a flame or explosion. It is important to note that the LEL for dust is highly dependent on particle size, as smaller particles have a larger surface area available for combustion, which can result in a lower LEL.

Understanding the LEL is essential for several reasons, such as ensuring the safe handling and storage of flammable materials, assessing the risk of fire or explosion, and designing safety systems in various industries.

Several factors influence the LEL, including temperature, pressure, particle size, and the presence of other gases or substances in the mixture. For example, the LEL generally decreases as temperature and pressure increase, meaning less fuel is needed for a mixture to become flammable. Conversely, as temperature and pressure decrease, the LEL typically increases. Additionally, the presence of other substances, such as diluent gases or chemical inhibitors, can affect the LEL by modifying the combustion process or altering the mixture's properties.

Gases have an upper threshold called the Upper Explosibility Limit (UEL), beyond which the mixture becomes too rich to ignite or explode due to the lack of sufficient oxygen, dust particles do not have a similar upper limit. This lack of a definitive upper limit for dust particles is primarily due to their unique physical properties and the dynamics of dust explosions. Even at very high concentrations, dust particles can retain sufficient oxygen between them to sustain an explosion.

Cube Root Law and K_{St}

The K_{St} value is an important parameter in evaluating the severity of dust explosions, specifically referring to the rate of pressure rise during an explosion (Eckhoff, 2003). It is an empirical value representing the deflagration index of a dust cloud, measured in bar·m·s^{-1}. K_{St} is used to classify dust materials based on their explosive potential and helps determine the safety measures required to prevent or mitigate dust explosion hazards, K_{St} classes are presented in Table 3.

Table 3: K_{St} classification (Eckhoff, 2003).

Classes	K_{St} (bar·m·s^{-1})	Explosion strength
St 0	0	No explosion
St 1	> 0 – 200	Weak explosion
St 2	> 200 – 300	Strong explosion
St 3	> 300	Very strong explosion

The «Cube Root Law», alternatively known as the «Cube Root Scaling Law», plays a critical role in defining the correlation between *dP/dt* values and the dynamics of dust explosions. This principle posits that the rate at which pressure rises during a dust explosion is proportionate to the cube root of the confined space's volume (Eckhoff, 2003).

Equation 4 represents these relationships. Here, $(dP/dt)_{max}$ signifies the maximum rate of pressure rise and is calculated by dividing the change in pressure by the change in time, with the units being bar·s^{-1}. The term $V^{1/3}$ represents the system volume raised to the one-third power.

$$\left(\frac{dP}{dt}\right)_{max} \cdot V^{\frac{1}{3}} = constant = K_{St} \qquad \textit{Eq. 4}$$

Deflagration

Deflagration is a type of self-propagating combustion wave characterized by its relatively low subsonic propagation speed with respect to the reactants ahead of the pressure wave (Lee, 2008). It is a complex process where the reactants transform into products, releasing the energy stored in their chemical bonds. This energy is then converted into thermal and kinetic energy of the combustion products, leading to large changes in the thermodynamic and gas-dynamic states across the combustion wave.

The properties and initial state of the explosive mixture and the boundary conditions behind the wave influence the speed at which deflagration propagates. Deflagration is an expansion wave where the pressure drops across the reaction front, and combustion products are accelerated in the opposite direction of the wave's propagation. As a result, the reactants are displaced ahead of the reaction front, causing the reaction front to propagate into reactants that move in the direction of propagation.

A propagating deflagration wave typically consists of a leading shock followed by the reaction front. The strength of the leading shock depends on the displacement flow velocity, which in turn depends on the boundary condition.

Deflagration propagation primarily occurs via heat and mass diffusion. The temperature and chemical species concentration gradients across the reaction front facilitate the transport of heat and radical species from the reaction zone to the reactants ahead, leading to ignition. Consequently, deflagration is a diffusion wave with a velocity proportional to the square root of the diffusivity and the reaction rate.

Detonation

Detonation is a highly exothermic chemical reaction. It is characterized by the supersonic propagation of a shock wave and a combustion zone, which together form the detonation front (Lee, 2008). This process can be distinguished from deflagration by the fact that detonation involves a shock wave travelling through the medium, while deflagration is a subsonic combustion process.

The detonation process can be divided into three distinct stages: initiation, propagation, and termination. Initiation refers to the application of energy (such as heat, shock, or electrical energy) to a reactive material in order to trigger a chemical reaction. This energy input causes the formation of a localized high-pressure region within the material, which subsequently leads to the generation of a shock wave.

Propagation occurs as the shock wave travels through the material at supersonic speeds, compressing and heating the reactants ahead of the wave. The rapid compression and heating cause the chemical reaction to occur almost instantaneously behind the shock front. The energy released from the chemical reaction further amplifies the shock wave and drives the

combustion zone forward. This self-sustaining cycle continues as long as there is unreacted material available.

Termination occurs when the shock wave reaches the boundaries of the reactive material, either by consuming all the available reactants or encountering a change in the surrounding medium that inhibits the continuation of the reaction. At this point, the shock wave dissipates, and the combustion process ceases.

Deflagration-to-Detonation Transition (DDT)

Deflagration-to-Detonation Transition (DDT) is a complex process involving transforming a subsonic deflagration wave into a supersonic detonation wave (Lee, 2008).

During the initial phase of DDT, the flame front experiences several instability mechanisms that contribute to its acceleration. The Landau-Darrieus instability arises due to the interaction between the flame front and the flow field it generates, while thermal diffusion instability results from the temperature gradients present in the reaction zone. The flame front can also experience instabilities due to its density interface, which varies due to temperature and pressure, resulting in Taylor instability, Richtmyer-Meshkov instability, and Rayleigh instability.

As the flame front accelerates, a precursor shock wave form ahead of it. This shock wave compresses the unburned fuel-oxidizer mixture, causing a localized rise in pressure and temperature. Finally, the compressed mixture reaches a state where it can ignite spontaneously, leading to the formation of a detonation wave. This process of shock-induced ignition is essential for the deflagration-to-detonation transition.

The transition from deflagration to detonation is influenced by various factors, including turbulence, which can be introduced by obstacles or confinement within a restricted space. Turbulence enhances the mixing of unburned fuel and oxidizer, increasing the reaction rate and creating localized regions of elevated pressure and temperature. These regions can accelerate the flame front and contribute to the formation of a detonation wave.

The chemical reactivity of the fuel-air mixture also plays a significant role in the likelihood of DDT. Highly reactive mixtures, such as hydrogen and acetylene, are more prone to undergoing DDT due to their lower ignition energy requirements and faster reaction kinetics. Conversely, less reactive mixtures with higher ignition energy and slower reaction kinetics are less likely to experience DDT under similar conditions.

Initial conditions, including pressure, temperature, and fuel-air equivalence ratio, can also affect the DDT process. These conditions influence the ignition delay times and reaction kinetics, either promoting or inhibiting the transition from deflagration to detonation. For example, increased initial pressure and temperature typically promote faster reaction kinetics, increasing the likelihood of DDT.

Lastly, the thickness of the reaction zone within the flame front can also influence the propensity for DDT. Thinner reaction zones typically exhibit faster flame propagation, leading to a higher likelihood of DDT. The reaction zone thickness and its interaction with turbulence can promote flame acceleration and contribute to the transition to detonation.

Quasi-Detonation

Quasi-detonation is a transient process that lies between the two extremes of combustion modes: deflagration and detonation (Gelfand et al., 2012; Lee, 2008). Quasi-detonation is characterized by a high-speed reaction front that propagates at a velocity between those of deflagration and detonation.

In a quasi-detonation, the reaction front velocity is significantly higher than the laminar flame speed of the mixture but lower than the Chapman-Jouguet (C-J) detonation velocity, in very rough tubes detonation velocities of less than 50% of the C-J values have been observed. As a result, this intermediate combustion mode exhibits some features of both deflagration and detonation, such as a highly compressed reaction zone and a strong pressure wave that propagates ahead of the reaction front. However, unlike in a true detonation, the reaction zone in a quasi-detonation is not fully coupled with the shock front.

The occurrence of quasi-detonation is often associated with specific conditions, including the presence of obstacles, confinement, or turbulence in the reactive mixture. These factors can lead to the amplification of flame speed and the formation of local hot spots, which may

initiate the transition from deflagration to quasi-detonation. The detailed mechanism of this transition, as well as the properties and structure of quasi-detonation, may vary depending on the specific fuel and oxidizer combination, initial pressure, and temperature of the reactive gas mixture. The mechanism governing quasi-detonations is to this date not fully understood.

Detonation Cell Size

Detonation cell size is a fundamental parameter that characterizes the multidimensional structure of a detonation wave in a reactive combustible mixture (Lee, 2008). It represents the characteristic spatial scale of the transverse wave pattern that forms due to the interaction between the shock front, the reaction zone, and the boundary layers in the detonating mixture. This multidimensional structure is also known as the cellular structure of detonation.

The detonation cell size, often denoted as λ, is typically measured as the distance between two adjacent triple points along the transverse wavefront. It is an important parameter in understanding the stability and dynamics of detonation waves, as well as their sensitivity to various factors, such as the initial conditions of the reactive mixture and the degree of confinement.

The detonation cell size is strongly influenced by the chemical composition of the mixture, the initial pressure and temperature, and the detailed reaction kinetics. In general, mixtures with higher activation energies and slower reaction rates exhibit larger detonation cell sizes, while mixtures with lower activation energies and faster reaction rates have smaller cell sizes. The detonation cell size is inversely proportional to the detonation sensitivity of the mixture, as smaller cell sizes are typically associated with more stable and robust detonation waves.

The measurement of detonation cell size is often performed experimentally using a variety of techniques, such as high-speed schlieren photography or soot foils. These methods capture the cellular structure of the detonation front, allowing for the direct measurement of the characteristic spatial scale of the transverse wave pattern.

Critical Diameter of Detonation Propagation

The following is based on Gelfand et al., (2012). The critical diameter of detonation propagation (d_{cp}) refers to the smallest channel diameter that permits a continuous detonation over extensive distances. The d_{cp} varies based on the specific fuel and oxidizer types involved. Generally, the d_{cp} equals one-third of the detonation cell size measured in a large diameter channel. When the channel diameter is equal to or smaller than the d_{cp}, unstable detonation types may occur, such as spin, galloping, and unsteady detonations. In certain mixtures, fast combustion modes have been observed within long, narrow channels, reaching velocities between 50-60% of the ideal detonation speed.

Critical Diameter of Detonation Transmission

The critical tube diameter for detonation transmission is the smallest tube diameter that allows a detonation to successfully transform into a spherical detonation when exiting into an open space (Gelfand et al., 2012). When the diameter is smaller than this value, the detonation can be quenched. A previously established correlation ratio of $d_{ct}/\lambda \approx 13$, has been identified for most fuel-air mixtures. However, recent studies suggests that this does not apply to rough tubes, where the value is estimated to be approximately $d_{ct}/\lambda \approx 8$ (Suna et al., 2022).

Chapman-Jouguet Detonation

The Chapman-Jouguet (C-J) detonation is a simplification that characterizes the steady-state, self-sustained propagation of a detonation wave in a reactive mixture (Lee, 2008). It represents the minimum velocity and associated pressure at which the shock wave and the reaction zone are fully coupled, such that the energy released from the chemical reactions exactly sustains the shock wave without any net gain or loss of energy.

In a C-J detonation, the reactive mixture is compressed and heated by the leading shock wave to the point where the chemical reactions behind the shock front are initiated and proceed at a rate sufficient to maintain the shock wave. The reactive mixture undergoes an irreversible transformation from an unburnt state (pre-shock) to a burnt state (post-shock). The chemical reactions occur within a thin reaction zone behind the shock front. At the C-J detonation

velocity and pressure, the burnt gas mixture reaches a thermodynamic equilibrium state, known as the Chapman-Jouguet state.

The C-J detonation velocity, denoted as D_{C-J}, and the C-J detonation pressure, denoted as P_{C-J}, are influenced by the chemical composition of the reactive mixture, the initial pressure and temperature, and the reaction kinetics. Both parameters are typically determined by solving the reactive Euler equations, which govern the conservation of mass, momentum, and energy in a compressible reacting flow, together with an appropriate equation of state and a set of reaction rate equations. Analytical or semi-analytical methods, such as the ZND (Zeldovich, von Neumann, and Döring) model, can be used to approximate the C-J detonation velocity and pressure for a given gas mixture, while more accurate numerical simulations or experimental measurements are often required to account for the complex multidimensional structure and dynamics of real detonation waves.

2.1.3 Thermal Radiation

When a dust particle is exposed to a flame front, it undergoes a process called pre-heating, which is the absorption of thermal radiation emitted by the flame. This pre-heating leads to the following (Eckhoff, 2016):

- *Lower ignition energy*: The increased temperature of dust particles reduces the energy required for ignition, making it easier for the flame front to sustain combustion and propagate through the dust cloud.
- *Acceleration of the flame front*: The pre-heating of dust particles increases flame front speed, as the elevated temperature enables combustion reactions to occur more rapidly. This can lead to a more violent explosion, characterized by higher pressure and greater damage potential.
- *Enhanced combustion efficiency*: Pre-heating dust particles allows for more complete combustion, reducing the likelihood of unburned dust particles being emitted from the explosion.

Thermal radiation-induced pre-heating plays a role in all dust explosions. However, its impact is most pronounced in metal and metalloid dust explosions due to the higher flame temperatures involved. This is because the energy from thermal radiation is proportional to

the temperature raised to the fourth power as evidenced by the equation 5 where Q^* is the thermal energy, σ, is the Stefan-Boltzmann constant, and T is the temperature.

$$Q^* = \sigma T^4 \qquad \textit{Eq. 5}$$

2.1.4 Pressure Piling

Pressure piling is a phenomenon that occurs in interconnected vessels when an explosion in one vessel travels through a conduit to another vessel (Ogle, 2016). The propagation of the flame pressurizes the unburnt gas ahead of it, amplifying the final explosion pressure in the second vessel. As the flame accelerates, the overpressure in the unburnt gas progressively increases.

The pressure piling process begins with a deflagration in the first vessel. Even if this vessel is vented, the flame can still enter the connecting conduit and advance towards the second vessel. As the flame moves through the conduit, a pressure wave forms in front of it. The acceleration of the flame results in the precompression of the gas in the connected vessel. When the flame enters the second vessel and ignites the dust inside, the deflagration pressure within the second vessel surpasses the explosion pressure typically associated with that dust concentration. This precompression effect magnifies the final explosion pressure.

The magnitude of the pressure piling effect depends on several factors, such as the volume ratio of the two vessels, the diameter of the connecting conduit, and the primary vessel's volume. The ignition location is also crucial, as shifting from central to edge ignition can increase the final pressure in the primary vessel.

Pressure piling involves various geometric complexities, including intricate process vessel geometry, flow obstacles, a connecting conduit with a variable cross-section or changing direction, and a receiving vessel with complex shape and internal features. In addition, flame propagation, turbulence, and gas dynamics are essential in determining the final pressures achieved in the vessels and conduit.

2.1.5 Particle Size Distribution

Particle size distribution refers to the quantitative characterization of a collection of particles, such as powders, granules, or droplets, by measuring and reporting the relative frequency of particles in various size ranges (Allen, 2003). This information is crucial in various scientific disciplines and industrial processes because the size distribution of particles can significantly influence the properties and behaviour of a material or system.

The following is based on Allen (2003), and are important aspects to considered when describing particle size distribution in detail. Particle size can be defined in various ways, such as the diameter, equivalent spherical diameter, or Feret's diameter. The choice of definition depends on the specific application and the shape of the particles. In some cases, the aspect ratio, the ratio of the longest to the shortest dimension, is also considered.

There are numerous methods for determining particle size distribution, including:

- *Sieving*: A mechanical process that separates particles by size using a series of sieves with different mesh sizes. Can be performed both wet and dry.
- *Laser diffraction*: A technique that measures the angular variation in the intensity of scattered light as a laser beam passes through a suspension or a dry powder, providing information about the size distribution.
- *Dynamic light scattering:* A method that analyses fluctuations in scattered light intensity due to Brownian motion of particles in a suspension, providing information about their hydrodynamic radius and size distribution.
- *Image analysis*: A technique that uses digital image processing to analyse the size and shape of particles in microscopy images.
- Coulter counter: An electrical sensing method that measures changes in electrical resistance as particles pass through a small aperture, providing information about their volume and size.

Particle size distribution data can be represented in several ways, such as histograms, cumulative distribution plots, or density functions. The choice depends on the specific application and desired level of detail. Several statistical parameters can be used to describe the particle size distribution quantitatively, including:

- *Mean:* The average particle size, which can be calculated as arithmetic, geometric, or harmonic mean, depending on the application.
- *Median (D50)*: The particle size at which 50% of the particles are smaller and 50% are larger.
- *Mode:* The most common particle size in the distribution.
- *Standard deviation and variance*: Measures of the spread of the particle sizes around the mean.
- *Quartiles and percentiles*: Specific points in the distribution that divide it into equal parts.
- *Span:* Term used to measure the distribution or range of particle sizes in a sample, defined by the relationship; (D90-D10)/D50.

Several theoretical models are used to describe particle size distributions mathematically, such as the log-normal, Rosin-Rammler and Gaudin-Schuhmann distributions. These models are often used to fit experimental data and make predictions about the behaviour of particles in various processes.

Representative Sampling

According to Allen (2003) the golden rules of sampling encapsulate these principles:

- Always sample a powder when it is in motion.
- Instead of taking a portion of the powder stream for the entire duration, it is preferable to collect the entire stream for multiple short time intervals.

In some cases, strictly following «the golden rules of sampling» may not be practical, especially when obtaining samples from large bags like bulk bags or flexible intermediate bulk containers. To ensure the sample's representativeness, reducing segregation, contamination, and other factors that could jeopardize sample quality is crucial. The following steps and considerations, adapted from Pitard (1993), outline the procedure for obtaining accurate powder or dust samples from large bags:

- *Selection of appropriate sampling tools:* Choose sampling devices designed specifically for powders and dust, such as thief samplers, powder lances, or core samplers. These devices enable the collection of samples from various depths and locations within the bag, ultimately yielding a more representative sample of the material.
- *Sampling plan:* Develop a practical sampling plan that considers the specific needs of the application, considering factors such as the material's variability, the desired level of accuracy, and analysis requirements. The plan should outline the number of samples required, the locations from which samples will be taken, and the sample size.
- *Sampling procedure: Sampling location:* Systematically select sampling locations to ensure representativeness. It is crucial to sample from multiple locations within the bag, as particle size distribution can vary due to segregation.
- *Sampling depth*: Utilize the sampling device to collect samples at different depths within the bag. This approach helps to obtain a more representative sample, as particle segregation can occur vertically within the container.
- *Sample extraction*: Carefully insert the sampling device into the bag, ensuring that the device reaches the desired depth. Extract the sample with minimal disturbance to the material and avoid introducing contamination.
- *Sample handling and storage*: After collecting the samples, transfer them to appropriate, clean, and labelled containers. Seal the containers to prevent contamination and change in moisture content. Store the samples in a controlled environment until analysis, adhering to any specific requirements for temperature, humidity, and light exposure.
- Quality assurance and quality control*:* Implement a quality assurance and quality control program to ensure that the sampling procedure is consistently performed, and the samples are representative of the material in the big bag. This may involve periodic reviews of the sampling plan, training of personnel, and verification of sampling equipment.

2.1.6 Converging and Diverging Nozzles

Converging and diverging nozzles are essential in fluid mechanics, particularly when examining compressible flows (El-Sayed, 2016). The nozzles act as flow modulators, and are changing the fluid's velocity and pressure, by adjusting the flow area. The fluid's behaviour in these nozzles can be explained using conservation principles of mass, momentum, and energy, along with the fluid's equation of state.

In a converging nozzle, the flow area narrows in the direction of the flow. When an incompressible fluid, such as water, flows through a converging nozzle, its velocity increases while its pressure decreases, as explained by Bernoulli's principle. Conversely, when a compressible fluid, like a gas, flows through a converging nozzle, its behaviour becomes more intricate, depending on the Mach number (the ratio of fluid velocity to the speed of sound in the fluid) and the fluid's specific heat ratio. When the Mach number is below one (subsonic flow), the converging nozzle accelerates the fluid, increasing its velocity, like in the incompressible case. However, if the fluid reaches a Mach number of one (sonic flow) at the nozzle throat (the narrowest cross-sectional area), the flow becomes choked, preventing further acceleration within the converging section of the nozzle.

In a diverging nozzle, the flow area expands in the direction of the flow. For subsonic flows, the fluid decelerates, and its pressure rises in a diverging nozzle. However, for supersonic flows, the fluid accelerates while its pressure and temperature decrease in the diverging section, a counterintuitive phenomenon compared to incompressible flows.

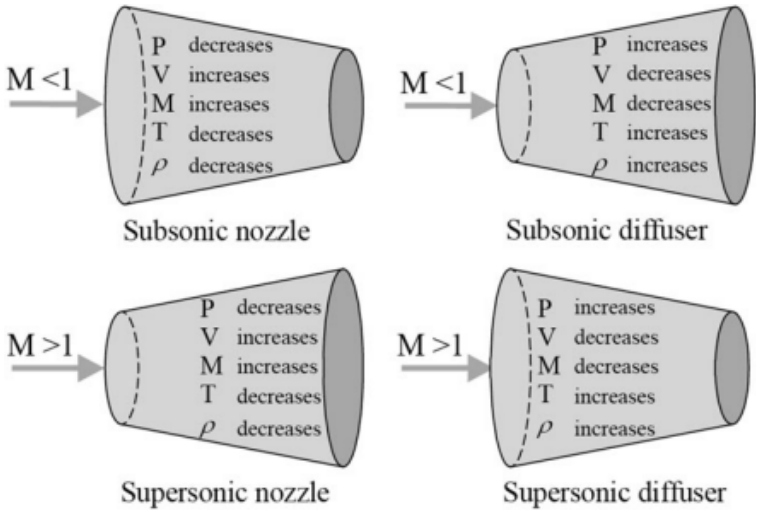

Figure 8: Variation of flow properties in subsonic and supersonic nozzles and diffusers (El-Sayed, 2016)

2.1.7 Shock Waves

Shock waves are nonlinear, high-amplitude disturbances that propagate through a medium at supersonic speeds, causing abrupt changes in the medium's properties. As a shock wave propagates, it compresses, heats, and alters the properties of the medium it is traveling through. The speed of a shock wave is always faster than the speed of sound in the medium. Shock waves exhibit four distinct characteristics (Krehl, 2001):

I. Pressure-dependent propagation velocity
II. Formation of a steep wave front with abrupt changes in thermodynamic properties
III. Significant decrease in propagation velocity with increasing distance from the point of origin for nonplanar shock waves
IV. Nonlinear superposition properties, such as reflection and interaction

Types of shock waves that can occur due to the energy release from explosions (Emanuel, 2001):

- *Normal shock waves:* In a normal shock wave the wavefront is perpendicular to the flow direction. These waves arise due to the sudden deceleration of a supersonic flow to a subsonic flow. As the supersonic flow encounters the shock wave, the velocity of the flow decreases, the pressure and temperature rise, and the density of the medium increases. These changes occur across a relatively thin region known as the shock layer.
- *Oblique shock waves:* Oblique shock waves are formed when a shock wave is inclined to the flow direction. These waves are commonly observed when a supersonic flow encounters a surface or object that is not perpendicular to the flow direction, such as a wedge or an airfoil. In these cases, the shock wave is bent or deflected around the object, creating an oblique angle with the flow direction. When the flow downstream of the oblique shock remains supersonic, the shock wave is called a weak oblique shock. If the flow transitions to subsonic, it is referred to as a strong oblique shock. In both cases, the flow experiences an increase in pressure, temperature, and density, similar to normal shocks, but to varying degrees depending on the shock wave angle and flow conditions.
- *Bow shock waves:* Bow shock waves are curved, detached shock waves that form in front of blunt objects, such as spheres or cylinders, when a supersonic flow passes around the object. The bow shock wave forms due to the inability of the fluid to flow

smoothly around the object's geometry, which results in a build-up of pressure upstream of the object. This pressure gradient leads to a curved shock wave that wraps around the object, separating the supersonic flow upstream from the subsonic flow downstream. Bow shocks are characterized by significant increases in pressure, temperature, and density behind the shock front, as well as a decrease in flow velocity.

- *Detonation waves:* Detonation waves are a specific type of shock wave generated by the rapid release of chemical energy during an explosive reaction, such as the combustion of a fuel-air mixture or the detonation of a high-explosive material. These waves are characterized by supersonic propagation speeds, typically ranging from 1.000 to 9.000 metres per second, depending on the properties of the material and the surrounding medium. Detonation waves are accompanied by a sharp pressure rise, an increase in temperature, and a decrease in density across the shock front. The energy released by the explosive reaction drives the expansion of the detonation products, creating a blast wave that travels through the surrounding medium.

Shock waves can alter their shape and become nonplanar when moving in ducts and pipes with changing cross-sectional are (Friedman, 1960). When the cross-sectional area expands, the intensity of the shock wave decreases, but as the area contracts, the strength of the shock wave increases. As a result, the propagating shock wave generates a distinct velocity in the flow behind it. In the case of a frictionless flow, this velocity aligns with the wall at the point of contact, and the shock wave remains perpendicular to the wall where it meets the surface.

Mach Reflections

Mach reflection is a shock wave interaction phenomenon occurring in steady, pseudo-steady, and unsteady flows when the supersonic flow encounters an obstruction like a wedge, converging duct or a reflecting surface such as a flat wall (Ben-Dor, 2001). This interaction gives rise to three intersecting shock waves: the incident shock, the reflected shock, and the Mach stem, along with a slip plane. The point where the three shocks meet is called the triple point, a unique feature of Mach reflection.

The triple point is crucial in determining flow properties downstream of the Mach reflection, as it signifies the transition from the influence of the incident shock to that of the reflected shock and Mach stem. The triple point's position and movement can impact overall flow

behaviour, pressure distribution, and shock wave interactions in supersonic devices like nozzles, diffusers, and wind tunnels, as well as the performance and stability of supersonic vehicles.

Converging ducts can produce a progressive series of Mach reflections that effectively concentrate the shock wave, leading to significantly higher pressures at the focal point (Milton, 2001). The angle of a converging duct substantially influences Mach reflections in several ways:

- *Oblique shock formation*: The angle of the converging duct affects the oblique shock wave's angle relative to the incoming flow direction. A larger converging duct angle results in a stronger oblique shock and a more significant change in flow properties across the shock.
- *Shock reflections*: A larger converging duct angle increases the likelihood of multiple shock reflections off the converging walls, creating a more complex network of shock waves within the duct.
- *Transition to Mach reflection*: The converging duct angle influences the transition from regular reflection to Mach reflection. When the angle between the converging walls' surface and the primary shock wave is large enough, a single reflected shock wave cannot turn the flow parallel to the wall, leading to a transition to Mach reflection.
- *Mach stem height*: The height of the Mach stem in Mach reflection depends on the converging duct angle. A larger angle typically results in a taller Mach stem, corresponding to a more significant difference in flow properties across the Mach stem.

Types of Mach reflection include Direct-Mach reflection, Inverse-Mach reflection, and pseudo-stationary-Mach reflection (Ben-Dor, 2006):

- *Direct-Mach reflection*: This type of Mach reflection occurs when the incident shock wave reflects off a solid surface, creating a secondary shock wave intersecting with the incident shock at the triple point. The flow conditions in Direct-Mach reflection are steady or pseudo-steady, meaning the flow properties do not change significantly over time.

- *Inverse-Mach reflection:* In this type of Mach reflection, the secondary shock wave reflects off the solid surface and intersects with the primary shock wave at the triple point, similar to Direct-Mach reflection. However, the angle between the incident shock wave and the solid surface differs from the Direct-Mach reflection, leading to a different flow pattern.
- *Pseudo-stationary-Mach reflection:* This can occur when the flow conditions are unsteady, meaning the flow properties change significantly over time. In this case, the shock waves interact with the solid surface in a manner that results in a pseudo-stationary reflection pattern, despite the unsteady nature of the flow.

Depending on the specific conditions, each primary type of Mach reflection can exhibit different reflection patterns, such as single-Mach, transitional-Mach, or double-Mach reflections (Krehl, 1992):

- *Single-Mach reflection*: This occurs when the incident shock wave interacts with the solid surface, generating a single reflected shock wave. The triple point, in this case, forms a simple Mach stem.
- *Transitional-Mach reflection*: This type of reflection occurs when the flow conditions are changing or approaching a critical point where the reflection pattern transitions from one form to another (e.g., from Single-Mach to Double-Mach reflection). The resulting pattern is a complex combination of the two forms.
- *Double-Mach reflection*: Double-Mach reflection occurs when the incident shock wave interacts with the solid surface in such a way that two reflected shock waves are generated. The triple point, in this case, forms a more complex structure, sometimes referred to as a double Mach stem.

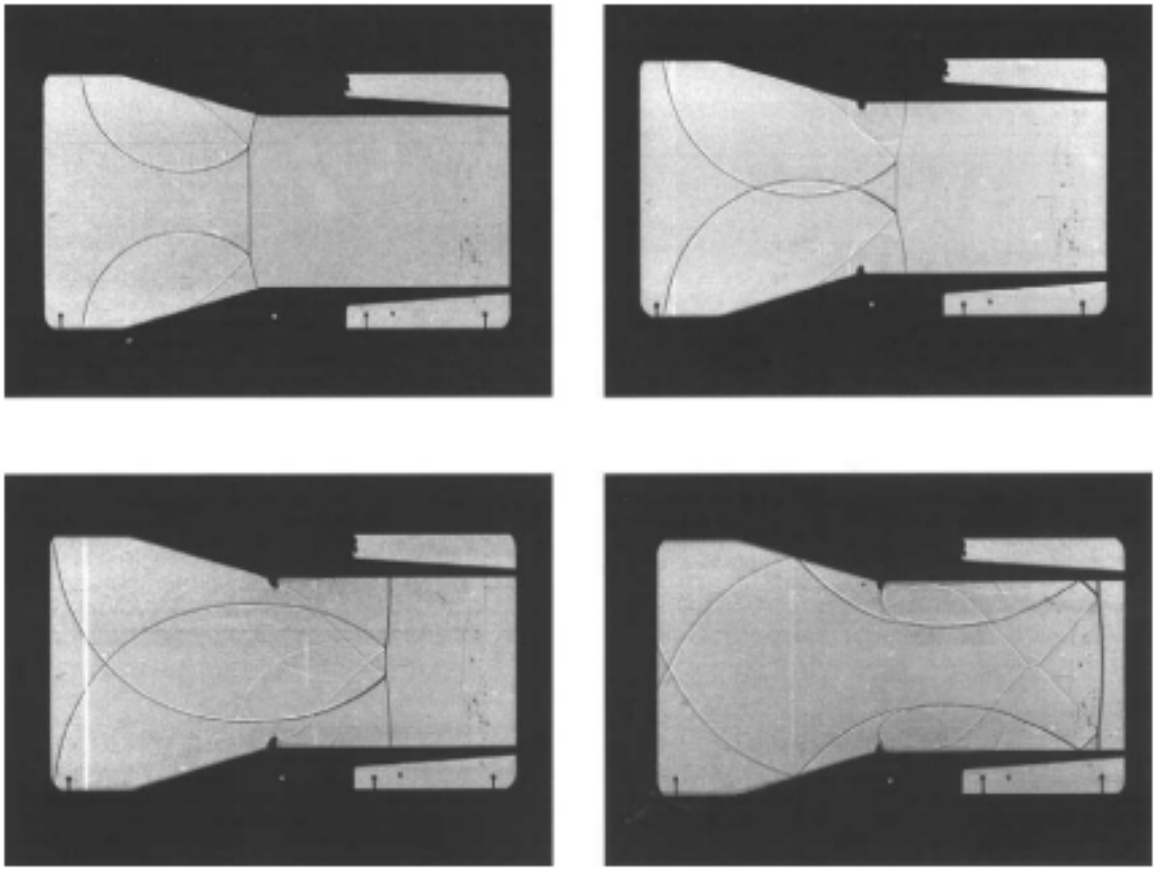

Figure 9: Mach reflections on converging walls leading to a steepening of the transmitted shock wave (Igra & Heilig, 2001).

2.1.8 Speed of Sound

The speed of sound in a gas is the rate at which pressure disturbances, such as sound waves, propagate through the medium (Young & Freedman, 2016). It is an important property of the gas, as it influences various phenomena, such as the transmission of information, noise propagation, and the behaviour of shock waves. To understand the speed of sound in a gas, we need to consider the gas's molecular interactions, compressibility, and thermodynamic properties.

Molecular interactions: Gas molecules interact with each other through collisions. When a pressure disturbance is introduced, the gas molecules closer to the source experience a change in momentum, which is then transferred to neighbouring molecules through successive collisions. This chain reaction of molecular collisions propagates the pressure disturbance through the gas, leading to the propagation of sound waves.

Compressibility: Gases are compressible, meaning their density can change under pressure. When a pressure disturbance is introduced, the density of the gas is altered locally, and the pressure wave propagates by compressing and expanding the gas. The speed of sound depends on how easily the gas can be compressed and uncompressed, which is related to its bulk modulus and density.

Thermodynamic properties: The speed of sound in a gas is influenced by its thermodynamic properties, such as temperature, pressure, and specific heat. The specific heat of a gas, namely the specific heat capacity at constant pressure and the specific heat capacity at constant volume, are essential in determining the speed of sound, as they describe how the gas responds to changes in temperature and pressure.

Considering the above factors, the speed of sound in a gas can be described mathematically by equation 6 (Young & Freedman, 2016), where *c*, is the speed of sound, *γ*, is the heath capacity ratio, *R,* is the universal gas constant, *T,* is absolute temperature and *M,* is the molar mass:

$$c = \sqrt{\frac{\gamma RT}{M}} = m \cdot s^{-1} \qquad \textit{Eq. 6}$$

In ideal gases, the speed of sound is primarily dependent on temperature, as it is the sole variable in the formula under ideal gas conditions.

Using the experimentally determined pyrometric flame temperature for Si particles with a median particle size of four µm, as reported by Cashdollar & Zlochower (2007), we can calculate the speed of sound in the surrounding medium assuming the behaviour of an ideal gas and gas properties of dry air (Lide, 2006):

$$c = \sqrt{\frac{1.4 \cdot 8.314\ J \cdot mol^{-1} \cdot K^{-1} \cdot 2300\ K}{0.0289655\ kg \cdot mol^{-1}}} = 960\ m \cdot s^{-1}$$

Speed of sound in the surrounding medium using adiabatic flame temperature (Cashdollar & Zlochower, 2007), and assuming ideal gas and dry air (Lide, 2006):

$$c = \sqrt{\frac{1.4 \cdot 8.314\ j \cdot mol^{-1} \cdot K^{-1} \cdot 3240\ K}{0.0289655\ kg \cdot mol^{-1}}} = 1140\ m \cdot s^{-1}$$

In an adiabatic process, heat is neither absorbed nor released by the system, meaning that all the energy released during combustion is used to increase the temperature of the reactants and products. Therefore, the adiabatic flame temperature is the highest theoretical temperature a combustion reaction can attain.

The pyrometric flame temperature is the particle temperature measured in the combustion process. In a combustion process with a high degree of volatilization, the temperature of the gases surrounding the dust particles could be higher than the pyrometric flame temperature. This is because the volatile components vaporize and undergo combustion, releasing heat and raising the temperature of the surrounding gases. However, this temperature will still be lower than the adiabatic flame temperature, as some heat will inevitably be lost to the surroundings during combustion.

In gas-particle mixtures, understanding sound propagation involves two fundamental concepts: the *frozen speed of sound* and the *equilibrium speed of sound* (Rudinger, 1980). These terms characterize the transmission of sound waves under varying conditions, contingent on the degree of interaction between the gas and particles.

The equilibrium speed of sound refers to the scenario in which particles always remain in equilibrium with the gas (Rudinger, 1980). In this case, the particles and gas maintain a balance in temperature and pressure, allowing the sound waves to propagate under isentropic conditions. The equilibrium speed of sound can be significantly lower than the speed of sound in a pure gas, particularly in cases where the particle mass fraction is high. As the particle volume fraction increases, the particle density ratio influences the equilibrium speed of sound, resulting in a more complex relationship between the gas and particle properties. Equilibrium speed of sound in gas-particle mixture, would be lower than that of clean gas. It can be lower by a factor of 0.5-0.6 (Eckhoff, 2003).

The frozen speed of sound describes the case where particles do not interact with the gas, maintaining their velocity and temperature as the flow changes rapidly (Rudinger, 1980). This situation is termed frozen flow, as the particles cannot adapt quickly enough to match the changing conditions in the gas. In such cases, the frozen speed of sound is determined by the gas properties alone, as if the particles were not present. However, when the volume occupied by particles is considered, it effectively reduces the volume available for the gas phase to

propagate sound waves. This reduction in available volume for wave propagation leads to an increase in gas density. Since the speed of sound in a medium is generally proportional to the square root of the ratio of the medium's bulk modulus to its density, an increase in gas density can result in a higher frozen speed of sound compared to that in a clean gas.

In dust explosions, the particle volume fraction is quite low as demonstrated in the section where the stoichiometric value is calculated, resulting in a negligible difference between the frozen speed of sound and the speed of sound in pure gas. This is attributed to the minimal overall impact of particles on the gas properties at such low-volume fractions. The actual speed of sound in a dust cloud lies between the frozen and equilibrium speed of sound, never exceeding the speed of sound in clean gas. The gas-phase speed of sound serves as a useful benchmark for determining the theoretical maximum speed of sound in a dust cloud in the concentration range used in this thesis.

2.1.9 Dust Lifting

Dust lifting is essential in the generation of an explosible dust cloud. For a dust layer to possess the ability to undergo rapid combustion in the form of an explosion, the dust layer needs to be suspended in the air (Eckhoff, 2003). The process of dust lifting can be divided into two categories:

- *Flow-Induced Dust Lifting (Crowe et al., 2011):* When a dust explosion occurs, the initial ignition of dust particles generates a high-velocity flow of expanding gases, which in turn can induce dust lifting from the underlying surface. This flow-induced dust-lifting mechanism is primarily driven by the shear stress exerted on the dust layer by the flow. The magnitude of the shear stress depends on the flow velocity and the dust layer's properties, such as particle size, particle density, and layer thickness. When the shear stress surpasses a critical value, the particles' interparticle forces are overcome, and they become entrained in the flow.
- *Shock Wave-Induced Dust Lifting (Li et al., 2022):* During a dust explosion, a shock wave can be generated because of the rapid pressure increase and the supersonic propagation of the flame front. The interaction of this shock wave with the dust layer can lead to the lifting of dust particles. When the shock wave encounters a dust layer, the pressure difference across the layer generates a force that acts to lift and disperse

the dust particles. The degree of dust lifting depends on the strength of the shock wave, the dust layer's properties, and the underlying surface's characteristics. In addition, the passage of a shock wave can create local turbulence and vortices near the dust layer, which can further enhance dust lifting.

2.1.10 Particle Jamming

Particle jamming is a phenomenon that can occur in a particle laden flow when the cross-sectional area forces the particles closer and closer to each other (Sun et al., 2019). If the cross-sectional area becomes small enough, and the local concentration high enough, the particles can jam the opening, resulting in an abrupt decrease in fluid velocity. The jamming of a converging nozzle caused by particle collisions is depicted in Figure 10.

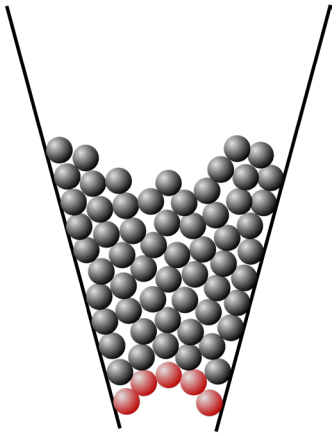

Figure 10: Illustration of particle jamming in converging nozzle (Wikipedia, 2022).

2.2 Previous Work

Numerous studies have been conducted to analyse flame propagation in dust layers and dust clouds within pipes, tubes, and ducts (Bartknecht, 1989; Gan et al., 2019; Liu et al., 2009; Zhang et al., 2001). Despite this, there has been a need for more research specifically focusing on dust explosions within pipe systems that mimic ductwork, particularly with varying cross-sectional areas aligned to the flow direction. This section aims to overview the relevant studies on the subjects studied in this thesis - flame propagation in pipes, the impact of varying cross-sectional areas in these pipes, and the extent of fireball length.

2.2.1 Detonation

Sichel et al. (1995) studied DDT in layered coal dust, using a 70-metre flame acceleration tube. The transition distance was found to be about twice that of pre-dispersed dust, which was attributed to the slow dust entrainment process. They also discovered that DDT favoured low moisture content, a large, exposed dust layer area subject to the convective flow behind the leading shock, and dust particles that promote entrainment. In the experiments, a retonation wave was observed, travelling upstream from the detonation at a nearly constant speed. When the retonation reached the end of the FAT, a reflected wave emerged, travelling downstream at the local speed of sound.

Liu et al. (2009) investigated DDT for aluminium dust-air mixtures under weak ignition conditions in a 0.199-metre diameter and 29.6-metre-long pipe. They found that the DDT process could be divided into two stages: a slow reaction compression stage and a fast reaction shock stage. In his study, the transition between the two stages was marked by the formation of a critical shock, with a speed of Mach 3.5 and an overpressure exceeding 48 bar. Liu observed the same transverse wave as Zhang. They found the detonation cell size for aluminium to be 0.495 metres. The detonation velocity oscillated between 1480 and 1820 $m \cdot s^{-1}$, while the overpressure ranged from 40 bar to 102 bar. The velocity was found to be in agreement with the C-J detonation velocity, but the overpressure was much greater than the C-J detonation pressure. Liu indicates that further research is needed to predict detonation pressure in aluminium dust-air mixtures.

Zhang et al. (2001) studied self-sustained dust detonations in air using two detonation tubes with diameters of 0.14 metres and 0.3 metres and a length-to-diameter ratio of 124. They tested dust-air mixtures of corn starch, anthraquinone, and aluminium. Zhang found that dust detonations in air are mainly influenced by transverse waves, which enable the coupling between the shock wave and the chemical reaction. Additional time scales are necessary for mass, momentum, and heat transfer between solid particles and the oxidizing gas environment, resulting in the transverse wave spacing of a dust detonation wave being significantly larger than that of homogeneous gas detonation waves. Consequently, large tube diameter is required to propagate self-sustained dust detonation in confined dust-air mixtures. For aluminium, the cell size was found to be 0.4 metres, and the minimum tube

diameter for stable detonation in air was 0.12 metres in a 0.3 metres detonation tube. The study estimates that a tube diameter of 0.1 to 1.0 metres is necessary for the propagation of a stable detonation for dust in the K_{St} range of 40 to 400 bar·m·s^{-1}. The same slow reaction compression stage and a fast reaction shock stage, as observed in the study by Liu et al., could be observed here, and is consistent with the theory on deflagration to detonation transition.

Wolinski & Wolanski (1992) studied shock wave-induced combustion of dust layers in a shock tube using wheat and brown coal dust in a pure oxygen atmosphere. They found that shock waves propagating over a dust layer can disperse the dust layer, create a combustible dust cloud, and ignite the dust cloud. A strong correlation was found between shock wave velocity and mixing and flame propagation, where higher-velocity shock waves promote a more intense combustion process. Detonations were observed for brown coal dust, and pressure profiles indicated nonuniformities in the flow behind the leading shock and pressure waves propagating in the reaction zone of the detonation wave.

2.2.2 Propagation Limits

Teodorczyk et al. (1989) studied quasi-detonation propagation in stoichiometric mixtures of gaseous H_2-O_2, C_3H_8-O_2, and C_2H_4-O_2 in a rectangular channel with obstacles. The channel had dimensions of 61.8 mm x 61.8 mm x 1.5 m. Teodorczyk found that quasi-detonation velocity depends on mixture sensitivity and obstacle spacing, with the C-J detonation velocity being reached when $d/\lambda = 10$ for a full channel. The re-initiation mechanism of the quasi-detonation is attributed to continuous re-initiation at the Mach stem, resulting from either thermally induced auto-ignition or turbulent mixing at the vortex in the shear layer of the triple point curling up behind the Mach stem. Decreasing obstacle spacing leads to increased wave attenuation and lower average quasi-detonation velocity.

The study suggests that propagation of quasi-detonation occurs due to re-initiation through shock reflections from the wall. Obstacles negatively affect wave propagation by attenuating detonation via diffraction. At critical conditions near the transition from choking to the quasi-detonation regime, the obstacle spacing, equivalent to the effective cell length of the quasi-detonation, is approximate twice the normal cell length. In high-speed deflagrations, the leading shock and its reflections from the wall play a minor role, while complex flame-obstacle interactions dominate the combustion mechanism for wave propagation.

Cross & Ciccarelli (2015) investigated deflagration-to-detonation transition and detonation propagation limits in a tube filled with obstacles. The experiments were conducted using hydrogen-air and ethylene-air mixtures at atmospheric pressure in a 6.1-metre-long and 0.1-metre-diameter tube. The tube was filled with 75 mm orifice plates, spaced at equal intervals, creating a 44% area blockage ratio. The study found that quasi-detonation propagation limits can be correlated with $d/\lambda = 1$ for all limits. Classic DDT limits are governed by the detonation propagation mechanism and are independent of the detonation initiation process. Quasi-detonation transmission limits in the smooth tube are narrower on the lean side than quasi-detonation propagation limits.

2.2.3 Fireball

The fireballs resulting from the combustion of metal and metalloid dust pose a greater risk than organic dust due to the intense thermal radiation they produce.

Holbrow et al. (2000) researched the thermal radiation emitted during vented dust explosions using a variety of dust types in two test vessels of 20 m^3 and 18 m^3 capacity. They found that intensity of thermal radiation produced by the external fireball in vented dust explosions is influenced by factors such as the type of dust, the size of the vent area, and the explosion pressure. However, they did not find a strong correlation between the thermal radiation and explosion characteristics like K_{St}. The findings emphasize the intense thermal radiation released by aluminium dust explosions, which reached an incident radiation level of 392.6 kJ/m^2 at a distance of 1 metre and 55 kJ/m^2 at 10 metres. In contrast, coal dust explosions produced comparatively lower incident radiation levels of 107.7 kJ/m^2 at 1 metre and 26.3 kJ/m^2 at 10 metres. This demonstrates the significant difference in thermal radiation hazards associated with different dust types during vented dust explosions.

2.2.4 Explosion Characteristics

20-litre tests have been conducted on silicon dust with a similar chemical composition and particle size to the silicon dust used in this thesis. This has been studied by Skjold (2003) and Østgård (2022). Skjold found that silicon dust with a median particle size of 3.5 to 3.8 micrometres resulted in an explosion overpressure of approximately 8.9 barg, and a rate of pressure rise of approximately 600 $bar \cdot s^{-1}$. Østgård studied silicon dust with a median particle

size of 2.77 micrometres and found the maximum explosion overpressure to be 9.7 barg, with the maximum rate of pressure rise being approximately 740 $bar \cdot s^{-1}$.

No studies have been identified that specifically studies FSM dust with a particle size and chemical composition similar to the one used in this study. However, useful insights can be gleaned from Eckhoff's book, «*Dust Explosions in the Process Industries*» from 2003. The appendix of this work contains a table displaying the explosion characteristics of various types of dust. Notably, it lists an FSM dust with a median particle size of 21 micrometres, comprised of 24% iron, 47% silicon, and 17% magnesium. This dust demonstrated a maximum explosion pressure of 9.9 barg and a K_{St} value of 267 $bar \cdot m \cdot s^{-1}$. It is, however, unclear whether these values were derived from tests conducted in a 20-litre or 1 m^3 vessel.

3 Materials and Methods

In this chapter material properties and experimental methods are described.

3.1 Material

In the experiments there were used two different types of dust. One is purified silicon (Silgrain) and the other is a metallurgical ferrosilicon-magnesium alloy (FSM). In this chapter properties like chemical composition and particle size distribution will be presented.

3.1.1 Dust Sampling and Analysis

The dust samples used in the experiments were provided by Elkem Bremanger and Elkem Bjølvefossen and sent to the University of Bergen. The specific sampling methods employed is unspecified. From the larger samples supplied by Elkem, smaller samples were collected in plastic bags and forwarded to Elkem Kristiansand for analysis. The sampling procedure for Malvern analysis was carried out as per the guidelines described in the user manual, which involved gently rolling and flipping the containers to ensure an even distribution of particle sizes and obtaining samples from multiple points (Malvern Panalytical 2013). Samples from each dust type were submitted for chemical and particle size analysis.

The Silicon dust used in the experiments, Silgrain MC, is a product manufactured by Elkem with strict tolerances regarding particle size. These samples are not material from extraction ducts but a finished product ready for further use. The ferrosilicon magnesium (FSM) dust utilized in the experiments is collected from a big bag, which gathers dust deposits from the cyclone filter of the dust extraction system and is a mixture of four different FSM products.

3.1.2 Particle size distribution

The particle size distribution of the dust types used in this study is presented below in Table 4. Malvern analysis reports is included in Appendix B.

Table 4: Particle Size Distribution of Si and FSM particles

Material	D50 (µm)	D10 (µm)	D90 (µm)	Span	D[3;2] (µm)	D[3;4] (µm)
Si (Silgrain MC)	2.65	0.76	4.91	1.57	1.74	2.81
FSM	9.71	2.38	24.10	2.24	5.14	12.10

3.1.3 Chemical composition

The chemical composition of the dust types used in this study is presented below in Table 5, and is analysed by Elkem, using X-ray fluorescence analysis. The analysis included all elements with a mass percentage above 0.5. Oxygen is determined separately by combustion method.

Table 5: Chemical Composition of Si and FSM particles

Element ($m_{\%}$)	FSM	Si (Silgrain MC)
Mg	9.1	0
Al	2.1	0.1
Ca	1.9	0.1
Ti	1.0	0
Fe	33.1	0
Si	46.8	99
O	2.9	0.5
Total	96.9	99.8

3.2 Laboratory-Scale Experiments

To assess the explosion characteristics of the FSM and Silicon dust samples, a 20-l-apparatus was employed to determine the lower explosive limit (*LEL*), maximum pressure (P_{max}), maximum rate of pressure rise (*dP/dt*), and deflagration index (K_{St}) for each dust.

3.2.1 Apparatus

The apparatus used in this testing is a modified USBM vessel. The internal volume of the vessel has been previously ascertained through water filling to be 20.50 ± 0.02 litres . When testing LEL, two 1 kJ chemical igniters are used. For all other testing, two 5 kJ chemical igniters are utilised.

Figure 11: Modified USBM vessel at UiB.

The dispersion system's valve, the triggering of the chemical igniters and the logging of the pressure all controlled remotely via a computer utilising the KSEP software form Kühner. For redundancy purposes, the vessel features a pair of Kistler 701A piezoelectric pressure transducers. The pressure transducers signals are amplified using a Kistler 5041 amplifier.

Correction Factor for pressure below 5.5 barg

The two 5kJ chemical igniters, produces on their own an overpressure of 1.6 barg in the vessel. To correct for this, all values produced by the KSEP program that is below 5.5 barg are processed using the correction factor in equation 7 (Cesana & Siwek, 2020). In this equation P_m is the corrected explosion overpressure, P_{ex} is the explosion overpressure, and P_{ci} is the overpressure caused by the chemical ignitors.

$$P_m = 5.5\left(\frac{P_{ex} - P_{ci}}{5.5 - P_{ci}}\right) \qquad \textit{Eq. 7}$$

Correction Factor for pressure above 5.5 barg

Due to the unfavourable surface-to-volume ratio, the explosion pressure recorded in the 20-litre-apparatus is often lower than that in a 1 m^3 vessel. This is largely due to the cooling effect exerted by the chamber walls on the gases, which subsequently leads to a decrease in the maximum pressure. To adjust for this effect, a correction factor is introduced in Equation 8. Here, P_m denotes the adjusted pressure, while $P_{ex,}$ refers to the maximum explosion overpressure measured. This adjustment is applied to all results generated by the KSEP program that fall below 5.5 barg (Cesana & Siwek, 2020):

$$P_m = 0.775 \cdot P_{ex}^{\,1.15} \qquad \textit{Eq. 8}$$

Formulas for determining P_{max}, $(dP/dt)_{max}$ and K_{St}

Maximum explosion overpressure, P_{max}, is calculated by averaging the corrected explosion overpressure, P_m, from three series. Maximum rate of pressure rise, $(dP/dt)_{max}$, is calculated by averaging the rate of pressure rise, *(dP/dt),* from three series. The deflagration index, K_{St} , is calculated by using the cube root scaling law, $V^{1/3}$, on the maximum rate of pressure rise, $(dP/dt)_{max.}$ All these calculations are performed automatically by the KSEP program using equation (Cesana & Siwek, 2020):

$$P_{max} = \frac{P_{m_{series1}} + P_{m_{series2}} + P_{m_{series3}}}{3}$$ *Eq. 9*

$$\left(\frac{dP}{dt}\right)_{max} = \frac{\left(\frac{dP}{dt}\right)_{series1} + \left(\frac{dP}{dt}\right)_{series2} + \left(\frac{dP}{dt}\right)_{series3}}{3}$$ *Eq. 10*

$$K_{St} = \left(\frac{dP}{dt}\right)_{max} \cdot V^{\frac{1}{3}}$$ *Eq. 11*

Evaluation Criteria for Lower Explosive Limit

To evaluate ignition or not during LEL testing, the criteria's in Table 6 should be used.

Table 6: Evaluation Criteria for LEL (Cesana & Siwek, 2020)

P_{ex} (bar)	**P_m (bar)**	**Decision**
< 0.5	< 0.2	No ignition
≥ 0.5	≥ 0.2	Ignition

Measurement Deviation

The deviation percentage for the different $(dP/dt)_{max}$ and K_{St} values are presented in Table 7, P_{max} represents the average of the highest values obtained from the three series. The highest value in each set must not exceed a deviation of 10% from the P_{max}, otherwise that series must be repeated (Cesana & Siwek, 2020).

Table 7: $(dP/dt)_{max}$ and K_{St} Deviation (Cesana & Siwek, 2020)

$(dP/dt)_{max}$	**K_{St}**	**Deviation**
≤ 185	≤ 50	± 30%
186 – 370	51-100	± 20%
371-740	101-200	± 12%
>740	> 200	± 10%

3.2.2 Experimental Procedure

Explosion Testing Procedure for the 20-l-aparatus at UiB:

Pre-Test preparation:

1. Examine the chamber for any residue from previous tests. If residue is found, clean the chamber using a brush, compressed air, and a vacuum cleaner.
2. Insert chemical igniters (2x1 kJ for LEL, 2x5 kJ for all other tests).
3. Open the dust dispersion chamber lid, add the desired amount of dust, and close the lid.
4. Close the exhaust valve.
5. Secure the lid on the USBM vessel.
6. Open the valves connected to the vacuum compressor.
7. Start the compressor and run it until the desired vacuum level is reached (0.6 barg for all tests).
8. Close the compressor valve on the x-mas tree.
9. Close the main valve to the x-mas tree. This valve also acts as a safety switch for the KSEP program.
10. Manually pressurise the dust dispersion chamber (20-21 barg).

Test execution:

11. Input the appropriate information about the dust being tested and its weight into the KSEP program. The program will calculate the concentration based on this data.
12. Initiate the test in the KSEP program. (The KSEP control unit will now stabilize the pressure in the dust dispersion chamber at 20 bar).

Post-test actions:

13. Immediately open the exhaust valve.
14. Activate the manual control for compressed air to the dispersion chamber, pressurise the chamber, and release the pressure into the vessel three times. This prevents the metal walls of the vessel from absorbing unnecessary heat from the hot atmosphere inside.
15. Open the lids of the vessel and the dust dispersion chamber.
16. Clean the chamber using a brush, compressed air, and a vacuum cleaner.

17. Inspect the dispersion chamber for any remaining dust deposits.
18. For LEL tests, perform a blank test with only igniters between each test to ensure no unburnt dust remains in the vessel.

Prior to conducting the next test:
The 20-litre apparatus at UiB lacks an integrated water-cooling system. This deficiency can lead to a heat soak condition in the vessel if tests are conducted back-to-back without sufficient cooling time in between. To ensure the vessel is ready for the next test, it is necessary to check its temperature.

To do this, cautiously feel the inner walls and the lid of the vessel. If the metal is cold to touch, it indicates that the apparatus has sufficiently cooled down and is ready for the next test. However, if the metal is warm, it is essential to wait until the apparatus has cooled down before proceeding.

3.4 Large-Scale Experiments

This section presents the experimental setup for the dust lifting and flame propagation experiments. This includes illustrations of the ignition chamber and various experimental configurations employed throughout the experiments, and an overview of the instrumentation used in the experiments.

3.4.1 Ignition chamber

To initiate dust lifting and create an explosion capable of both lifting and igniting the dust layer in the pipe(s) in the dust lifting and flame propagation experiments, a 32-litre ignition chamber was designed. This ignition chamber's design incorporates elements from a dispersion system created by Skjold et al. (2014), it was originally used in a flame acceleration tube experiment. Components borrowed from this experiment include a 2-litre pressure tank, a dust dispersion chamber, a Bosch fast-acting valve, and a single dispersion nozzle. The ignition chamber is engineered to endure a pressure of 25 bar, with a safety factor of four, concerning its ultimate tensile strength. This was validated with a finite element analysis in Autodesk Inventor, the analysis is included in Appendix C. An illustration of the ignition chamber can be seen in Figure 12.

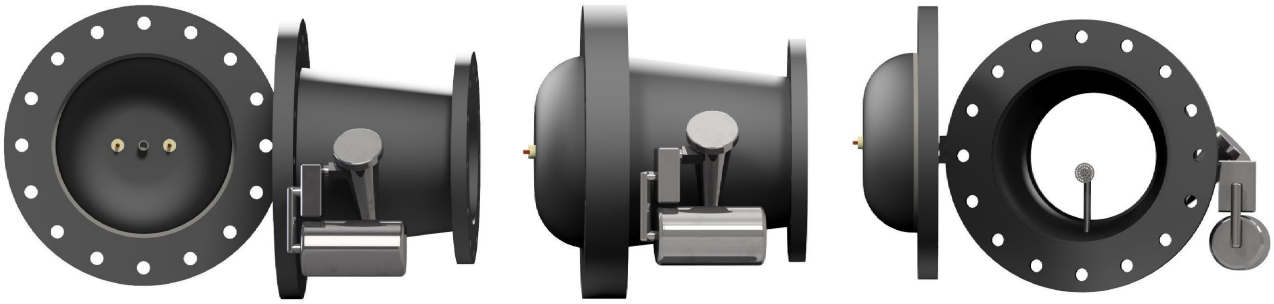

Figure 12: Rendered images of 32-litre ignition chamber. Image on the left shows the chemical ignitor holder placed inside the lid. The image in the middle shows the chamber closed, highlighting the pressure tank and the dispersion chamber. The image on the right shows the dispersion nozzle inside the chamber.

3.4.2 Pipes

Dust extraction and ventilation ducts commonly feature multiple ducts of varying sizes, typically structured with a large primary duct that branches into increasingly smaller extensions, as shown previously in Figure 3. To examine the effects of decreasing or increasing pipe dimensions on silicon dust explosions, three distinct pipe sizes were utilised in the experiments. To facilitate configuring the pipes in various arrangements, flanges were welded to both ends of the pipes, and concentric crossovers were made to accommodate both diminishing and expanding pipe sizes. In this chapter, the various pipes and configurations used in the experiment will be presented. In Table 8 and Table 9, the dimensions and specifications of the pipes and crossovers are listed.

Table 8: Specifications on various pipes utilised in the experiments.

Pipe length (m)	Number of pipes	Outer diameter OD (mm)	Inner diameter ID (mm)	Designation	Pressure Class (bar)
6000	1	273	245	DN250	670
6000	1	178	157	DN160	770
6000	2	73	62	DN60	730

The various pipe sizes will be referred to as DN250, DN160, and DN60 henceforth.

Table 9: Crossovers used in the experiments to connect pipes of different diameters.

Concentric crossover	Length (mm)	OD_1 (mm)	OD_2 (mm)	Half angle (degrees)
DN250 to DN160	248	273	168	11.95
DN160 to DN60	190	168	76	13.61

Configuration 1

The 6-metre DN250 pipe connected to the ignition chamber and the transducer placement is illustrated in presented in Figure 13.

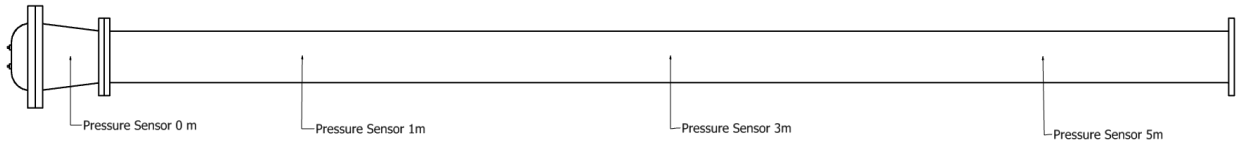

Figure 13: Illustration of pressure transducer placement on configuration 1

Configuration 2

The 6-metre DN160 pipe connected to the ignition chamber and the transducer placement is illustrated in presented in Figure 14.

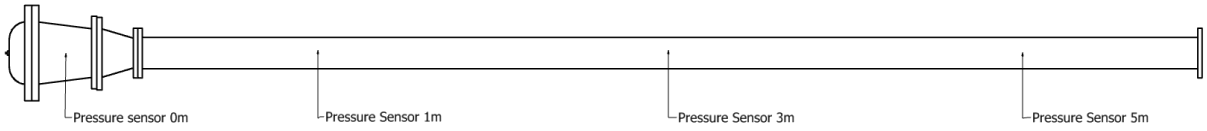

Figure 14: Illustration of pressure transducer placement on configuration 2

Configuration 3

Configuration 3 consists of the ignition chamber, a DN250 and DN160 pipe. The configuration and transducer placement are illustrated in Figure 15.

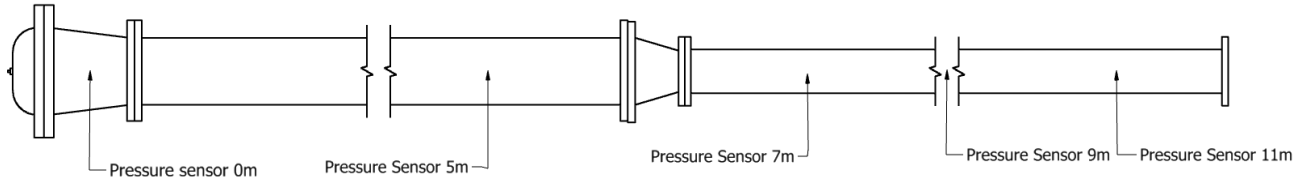

Figure 15: Illustration of pressure transducer placement on configuration 3.

Configuration 4

Configuration 4 consists of the ignition chamber, a DN160 and DN250 pipe. The configuration and transducer placement are illustrated in Figure 16.

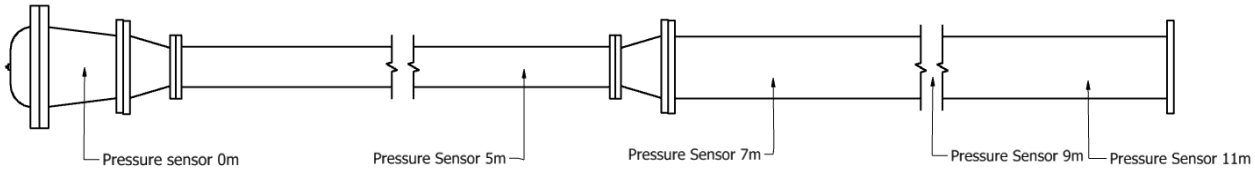

Figure 16: Illustration of pressure transducer placement on configuration 4.

Configuration 5

This configuration consists of ignition chamber, DN250 pipe, DN160 pipe and the crossover from DN160 to DN60. The configuration and the transducer placement are illustrated in Figure 17.

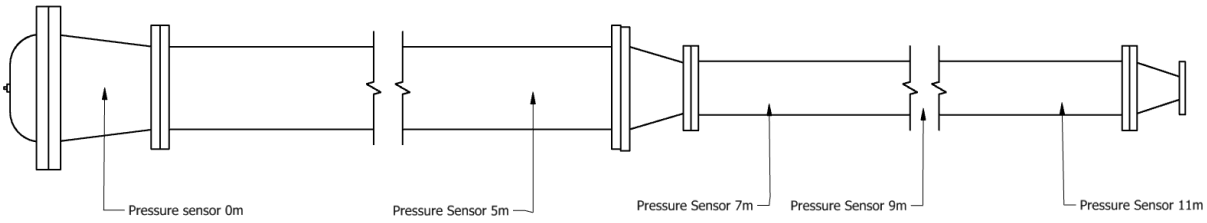

Figure 17: Illustration of pressure transducer placement on configuration 5.

Configuration 6

This configuration consists of the ignition chamber, a 6-metre DN250 pipe, a 6-metre DN160 pipe, and two 6-metre DN60 pipes. The configuration and the transducer placement employed test #1 and #2 with silicon dust, and the test with FSM are illustrated in Figure 18. Transducer placement for test #3, #4 and #5 is illustrated in Figure 19.

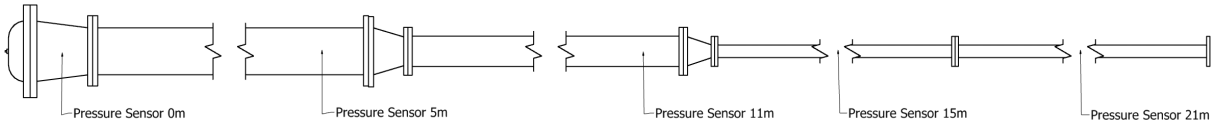

Figure 18: Illustration of pressure transducer placement on configuration 6 for test #1 and #2 with silicon, and the test with FSM.

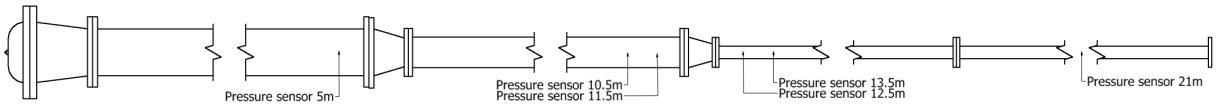

Figure 19: Illustration of pressure transducer placement on configuration 6 for test #3, #4 and #5 with silicon.

3.4.3 Test Parameters

In order to identify the suitable dispersion pressure, dust concentration, and ignition delay time for the initial explosion, a blind flange was affixed to the ignition chamber, as seen in Figure 20. The aim was to fine-tune these settings so that the explosion pressure within the ignition chamber corresponded to the maximum explosion pressure observed for the specific dust in the 20-litre apparatus. This method turned out to be notably time-consuming and challenging due to its exclusive reliance on explosion overpressure readings. To expedite the process, additional tests were carried out without the chemical igniter and blind flange, enabling the visualisation of dust dispersion with a high-speed camera.

Figure 20: 32-litres ignition Chamber with blind flange

These tests, conducted without the blind flange and chemical igniter, proved invaluable. The high-speed camera footage revealed that the initial dispersion pressure was too low. Following some fine-tuning and later tests, the dispersion pressure was set to 21 barg, which was consistently used in all tests. The visual observations also indicated that some dust began exiting the ignition chamber before all the dust had left the dispersion chamber. Initially, the plan was to use a concentration of 500 g/m^3, as it yielded the highest pressure in the 20-litre apparatus. Based on this, the concentration for subsequent tests was increased from 500 g/m^3

to 750 g/m^3. The dust cloud generated from the setting used in the experiments, can be seen in Figure 21.

Figure 21: Test of dispersion pressure

Using the dispersion pressure and concentration that was found from the tests with no ignition, there were done numerous tests with ignition to find the optimal ignition delay time. Since the pressure sensors did not show much variation in explosion pressure due to the chamber being open, the length of the fireball was measured as illustrated in Figure 22. This revealed that setting an ignition delay time of 200 milliseconds between activating the pressure tank valve and triggering the chemical igniter resulted in a sufficient explosion.

Figure 22: Determination of ignition delay time

3.4.4 Instrumentation

This section presents the equipment and software used for sampling and processing of experimental data.

Thermocouple

Thermocouples were utilized in an attempt to measure flame arrival times in the pipes. The first approach involved employing 0.2 mm type K thermocouples, positioned one metre apart along the entire length of the pipes. However, this method proved unsuitable for these experiments because the high flame temperature and the force exerted by dust particles on the thermocouple wire caused them to either break or melt.

In an attempt to solve this, the thermocouples were changed from bare 0.2mm type K to jacketed type K thermocouples to address this issue. This solution, however, created new challenges. Although the additional layer of metal encasing the thermocouple wire offered improved durability, it also contributed to increased thermal mass, leading to a slower response time, making the measurements unusable. Due to time constraints, it was decided to proceed with the experiments without flame speed measurement.

Pressure Transducers

In the experiments Kistler 601CAA piezoelectric pressure transducers were used. These pressure transducers were positioned in ¾" BSP plugs, recessed 1 mm from the plug's surface. The tips of the transducers were covered with high-temperature silicone.

Amplifier

The signal from the transducers is enhanced by using a Kistler 5064D amplifier, mounted in a Kistler 2853B chassis. The amplifier's output signal ranges from -10 to 10 V.

Data Acquisition

The experimental data were recorded using a program named, Test Logger, developed in LabVIEW by Matthijs van Wingerden. This program initiates the data logger, which subsequently activates the measure function on the amplifier for the pressure transducers. A USB-6259 data logger, manufactured by National Instrument, was employed in the experiments.

Data Processing

Unless otherwise mentioned, all data presented in this thesis has undergone some form of filtering or smoothing. This process is carried out using a program called Analyze, a filtering and smoothing program developed in LabVIEW for Gexcon AS, by Matthijs van Wingerden.

A significant portion of the experimental data was affected by 50 Hz noise with an amplitude of around 200 mV. To address this issue, all the affected data was processed in Analyze with a 50 Hz noise reduction filter. Additionally, all data was processed using a Savitzky-Golay smoothing filter within the Analyze program. All graphs presented in this thesis were created using MATLAB.

High Speed Camera

To analyse fireball characteristics, a GoPro Hero 11 was employed to record the events. The camera captured the footage at a rate of 240 frames per second, with a resolution of 2704x1520, providing detailed and high-quality imagery for further analysis.

3.4.5 Experimental procedure

In this section, the experimental procedure and the dust concentrations utilised in the dust lifting and flame propagation experiments will be presented.

Experimental Procedure

Pre-Test preparation:

1. Inspect the chamber and pipe(s) for any remnants from prior experiments. If any residue is detected, clean the chamber and/or pipe(s) using a rotating brush connected to an electric drill as shown in Figure 23, compressed air, and a vacuum cleaner.

Figure 23: Illustrating the rotating cleaning brush in DN250.

2. Place a 5-kJ chemical igniter into the igniter holder within the ignition chamber.
3. Open the lid of the dust dispersion chamber, add the required quantity of dust, and close the lid. In all tests for these experiments, a concentration of 750 g/m^3 of silicon was utilised, which corresponds to 24 grams.
4. Distribute the required amount of dust to the 6-metre angel iron using a suitable spreader. Position the angle iron within the pipe and flip it to ensure the dust settles at the bottom. Utilise the angle iron to evenly distribute the dust along the lower half of the pipe by

simultaneously moving both ends of the angle iron from the 9 o'clock to the 3 o'clock position. This process is illustrated in Figure 24.

Figure 24: Illustrating the distribution of dust in the angle iron and in the DN250 pipe.

5. If using a setup with multiple pipes, repeat step 4 until all pipes have the desired dust concentration.
6. Connect the ignition chamber to the pipe(s).
7. Shut the ignition chamber lid and fasten the bolts.
8. Open the compressed air flask valve and pressurise the tank to 21 barg. Close the valve once pressurised.
9. Connect the chemical igniter trigger cable.

Test execution:

10. Enter the relevant test configuration details, dust type, and concentration into the logging program. Ensure all necessary acquisition settings are enabled.
11. Sound the air horn to alert nearby individuals of an impending explosion.
12. Initiate the test by pressing the start button on the logging program.

Post-test procedures:

13. Disconnect the chemical igniter trigger cable.
14. Open the ignition chamber lid.
15. Perform a light cleaning by vacuuming the ignition chamber and then purging the system with compressed air.
16. Examine the pipe(s) for any smouldering residue. If smouldering residue is present, repeat step 15. If not, proceed to step 17.
17. Thoroughly clean the ignition chamber and pipe(s) with the rotating brush attached to an electric drill, compressed air, and a vacuum cleaner.

18. Inspect the dispersion chamber for any residual dust deposits. If any, clean the chamber using compressed air.

Dust Concentrations

In the experiments, a wide range of dust concentrations were utilised. The concentrations and the corresponding mass for each pipe is listed in Table 10.

Table 10: Mass of dust utilised in ignition chamber and pipes at a given concentration.

Concentration in pipe (g/m^3)	**Ignition Chamber (g)**	**DN250 (g)**	**DN160 (g)**	**DN60 (g)**
No dust in pipes	24.0	0	0	Not tested
250	24.0	70.7	29.0	Not tested
500	24.0	141.4	58.1	Not tested
750	24.0	212.1	87.1	Not tested
1000	24.0	282.9	116.2	18.1
1500	24.0	424.3	174.2	Not tested
2000	24.0	565.70	232.3	Not tested
5000	24.0	1414.3	580.8	90.6

3.5 Simulation

The Chapman–Jouguet velocity for a stoichiometric mixture of silicon and air has been calculated employing the following methodology:

- *Generating CHEMKIN Files:* Using the NASA Thermobuilder, thermodynamic data for all species involved in the following reaction are compiled: $Si + O_2 + 3.76N_2 = SiO_2 + 3.76N_2$. This data is then utilized to create CHEMKIN files in NASA9 format.
- *Converting to CTI File:* The CHEMKIN file created in the previous step is converted into a Cantera Input (CTI) file using the Cantera software. Cantera is an open-source chemical kinetics software package used in this case to translate the NASA9-formatted thermodynamic data into a format more conducive to further processing.
- *Creating a Thermodynamic Model:* Using the CTI file created in the previous step, a thermodynamic model is constructed, assuming silicon as an ideal gas.
- *Calculate C-J Velocity*: Calculating C-J Velocity: The thermodynamic model is employed to calculate the C-J detonation velocity. This is accomplished using a Shock and Detonation toolbox in Python, developed by Shepherd (2023). The toolbox provides functions and methods for calculating parameters related to shock and detonation waves, including the C-J velocity.

It is important to note that the thermodynamic model assumes that the combustion of silicon occurs entirely in the gaseous phase. This assumption likely results in an overestimation of the C-J velocity because it does not account for reactions that may occur in other phases or heat loss due to the melting of silicon particles. It only accounts for the heat loss caused by the transition from liquid to gas. Therefore, the calculated C-J velocity should be treated as an approximation. A more detailed thermodynamic model should be constructed for a more accurate calculation. Unfortunately, this was not achievable within the timeframe of this thesis.

4 Results

This chapter will present the experimental findings obtained from tests conducted using the 20-litre apparatus and in the dust lifting and flame propagation experiments, this includes results from all configurations presented in chapter 3.4.2.

4.1 Laboratory-Scale Experiments

In this section, results obtained from the 20-l-apparatus will be presented. KSEP reports are included in Appendix A.

4.1.2 Silicon

The P_{max} and *dp/dt* results obtained from the tests with silicon in the 20-litre-apparatus, is presented in figures 25 and 26. All results are summarized in Table 11.

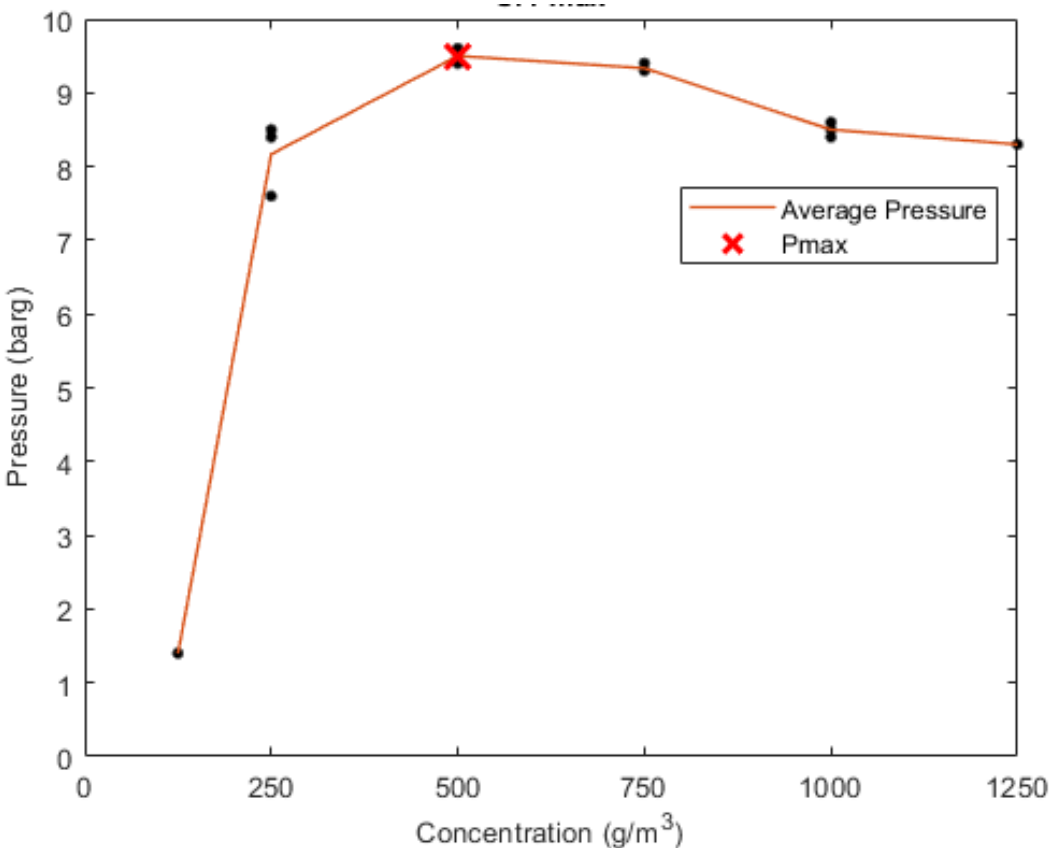

Figure 25: Silgrain MC (Si) P_{max}. Plotting concentration against pressure.

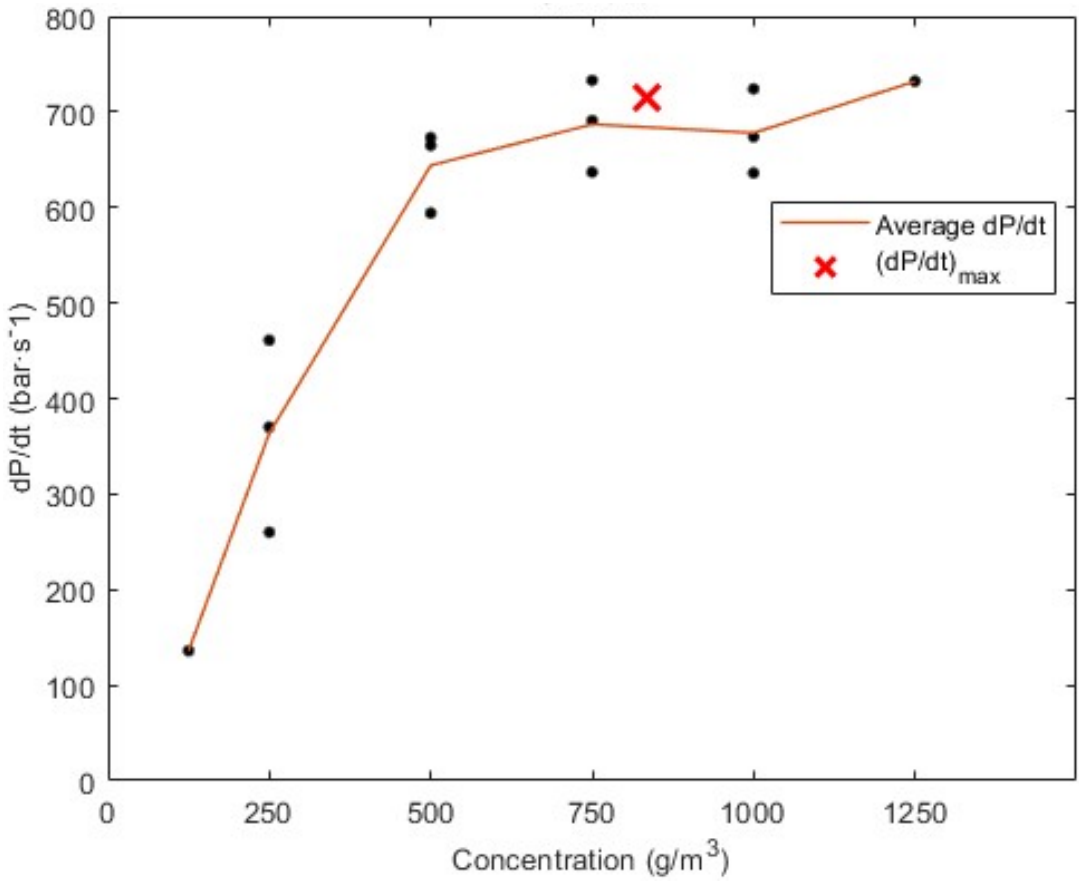

Figure 26: Silgrain MC (Si) dP/dt. Plotting rate of pressure rise against concentration.

Table 11: Explosions Characteristics of Silgrain MC (Si)

P_{max} (barg)	**$(dP/dt)_{max}$ (bar/s)**	**K_{St} (bar·m·s^{-1})**	**LEL (g/m^3)**
9,5 ± 10 %	716 ± 12 %	194 ± 12 %	100 ± 10 %

4.1.3 FSM

The P_{max} and *dp/dt* results obtained from the tests with FSM in the 20-litre-apparatus, is presented in figures 27 and 28. All results are summarized in Table 12.

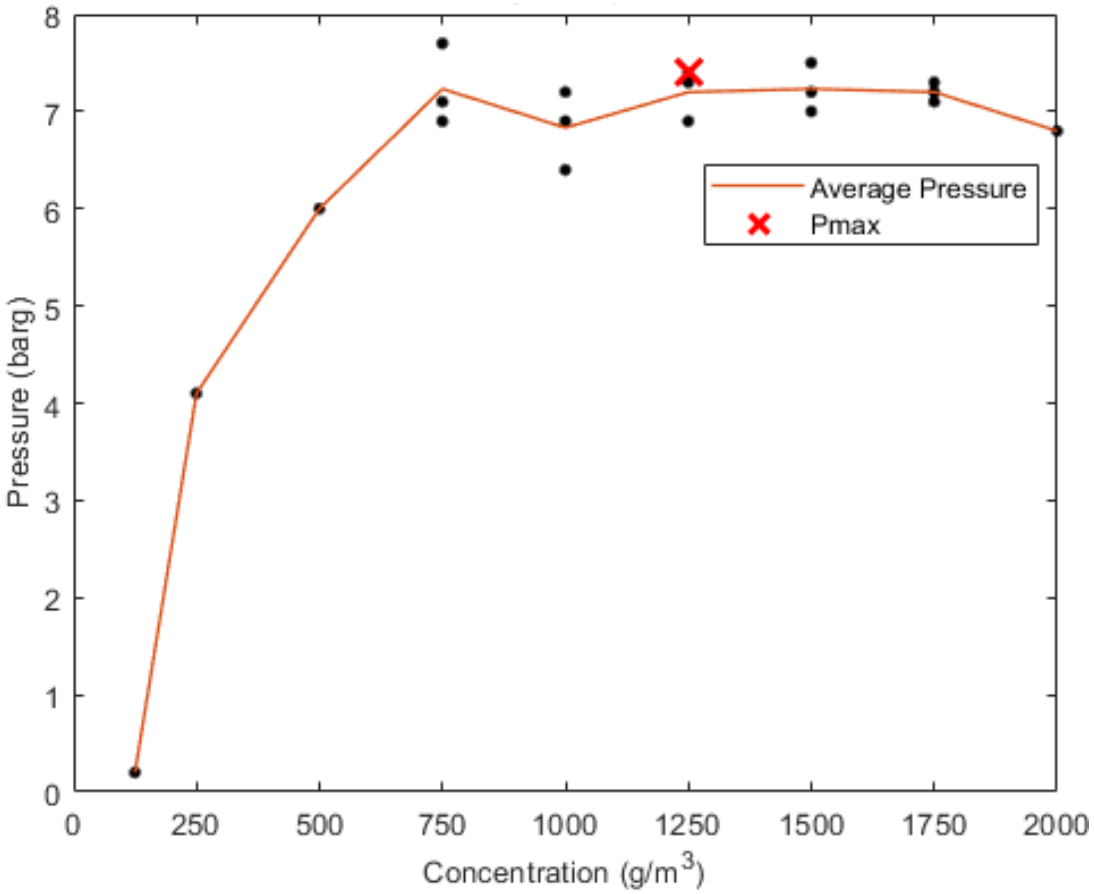

Figure 27: FSM P_{max}. Plotting concentration against pressure.

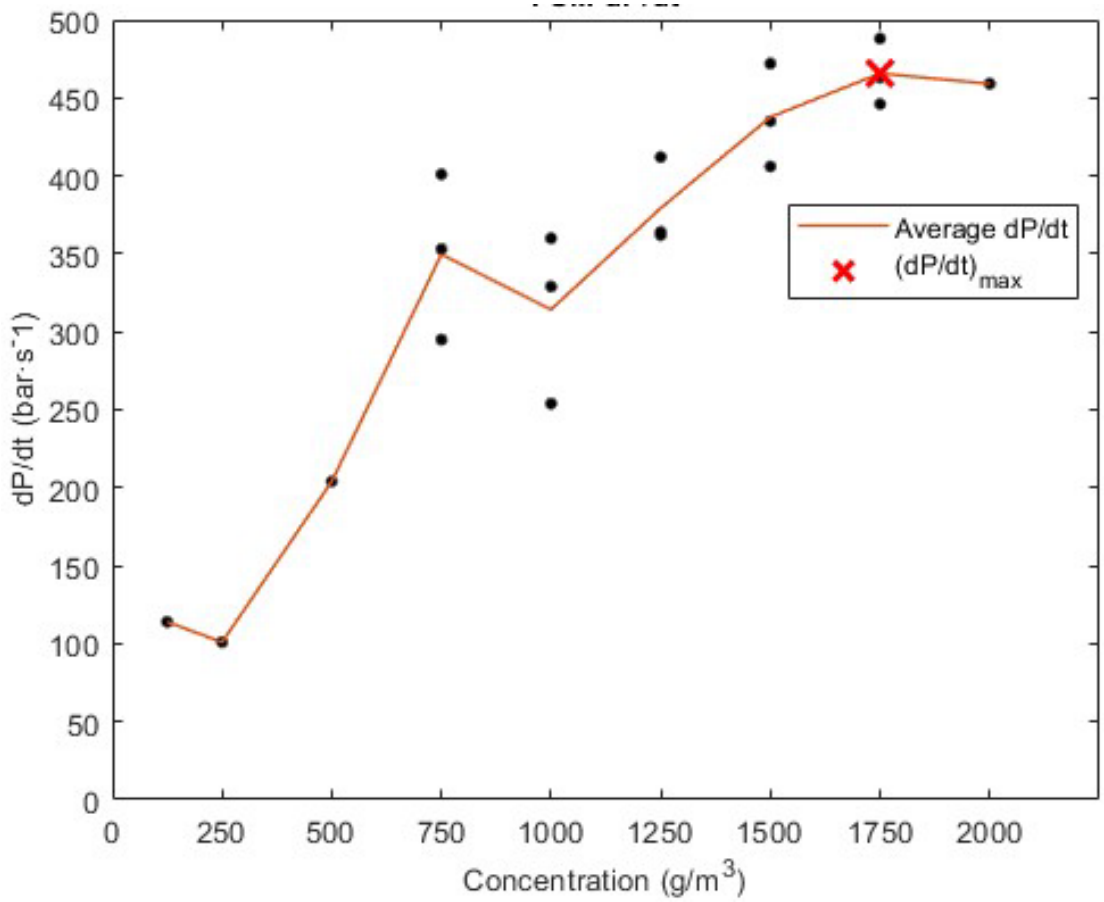

Figure 28: FSM dP/dt. Plotting rate of pressure rise against concentration.

Table 12: Explosions Characteristics of FSM

P_{max} (barg)	$(dP/dt)_{max}$ (bar/s)	K_{St} (bar·m·s^{-1})	LEL (g/m^3)
7,4 ± 10 %	473 ± 12 %	128 ± 12 %	100 ± 10 %

4.2 Large-Scale Experiments

In this section the results from the dust lifting and flame lifting experiments will be presented.

4.2.1 Configuration 1

In this section the results from tests in configuration 1, consisting of the ignition chamber and the DN250 pipe will be presented.

Fireball

The fireball's observed in the DN250 with FSM and silicon is shown in figures 29 and 30, and the measured lengths are presented in Table 13. The results show a strong correlation between dust layer concentration and fireball length, for both FSM and silicon. Silicon produces the largest fireball for all tested concentrations.

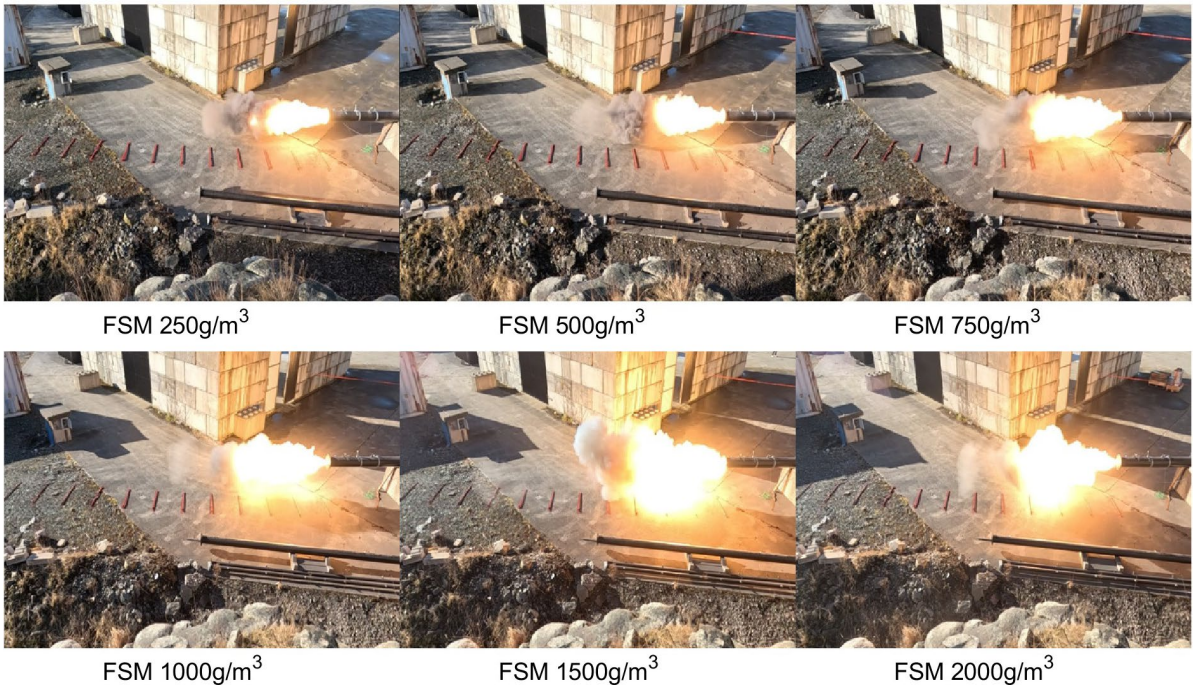

Figure 29: FSM fireball size in configuration 1 at different concentrations.

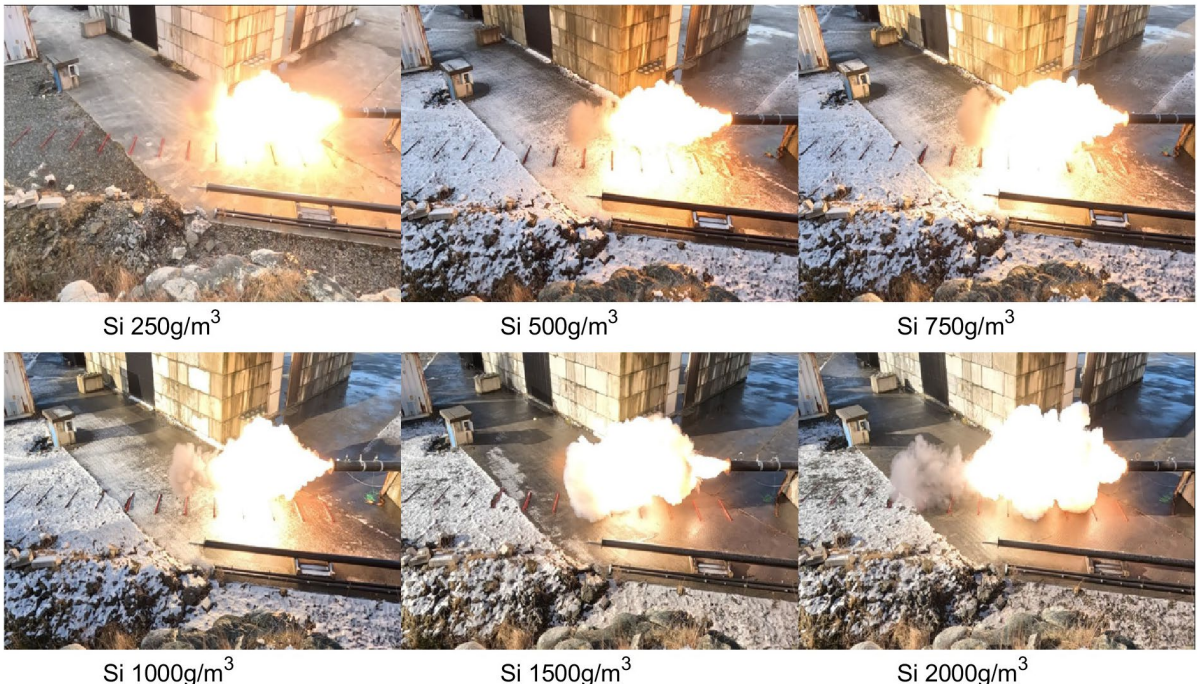

Figure 30: Si fireball size in configuration 1 at different concentrations.

Table 13: Fireball length FSM and silicon in configuration 1

Concentration (g/m³)	Fireball length FSM DN250 (m)	Fireball length silicon DN250 (m)
0	1.5	1.5
250	2.5	4.0
500	2.5	4.0
750	3.0	4.5
1000	3.0	4.0
1500	3.5	5.0
2000	3.5	5.0

Figure 31 exhibits the difference between no dust in pipe, and a concentration of 250 g/m^3 for FSM and silicon.

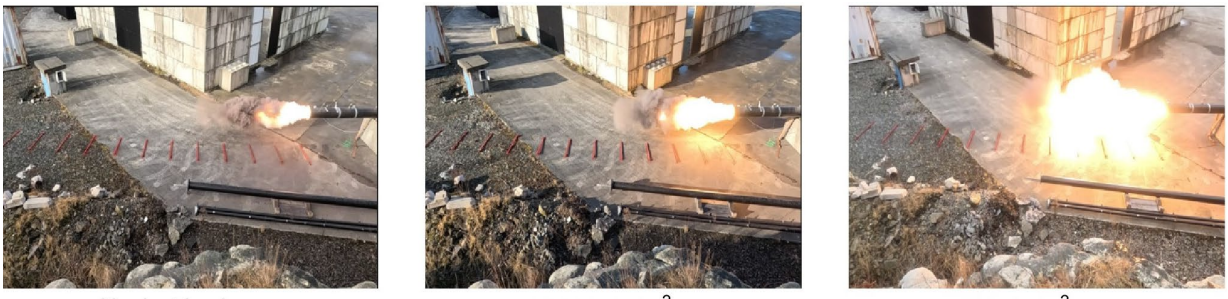

Figure 31: Comparing fireball size in configuration 1 for 250g/m^3 of Si and FSM with no dust in pipe.

Explosion Pressure

The experimental results from the test series with FSM in a DN250 pipe are graphically presented in Figure 32. These results indicate that the layered FSM dust amplifies the explosion pressure within the pipe. However, it is noteworthy that this observed increase in pressure does not appear to correlate directly with the concentration of the dust layer. Interestingly, the explosion pressures remain relatively stable across various concentrations.

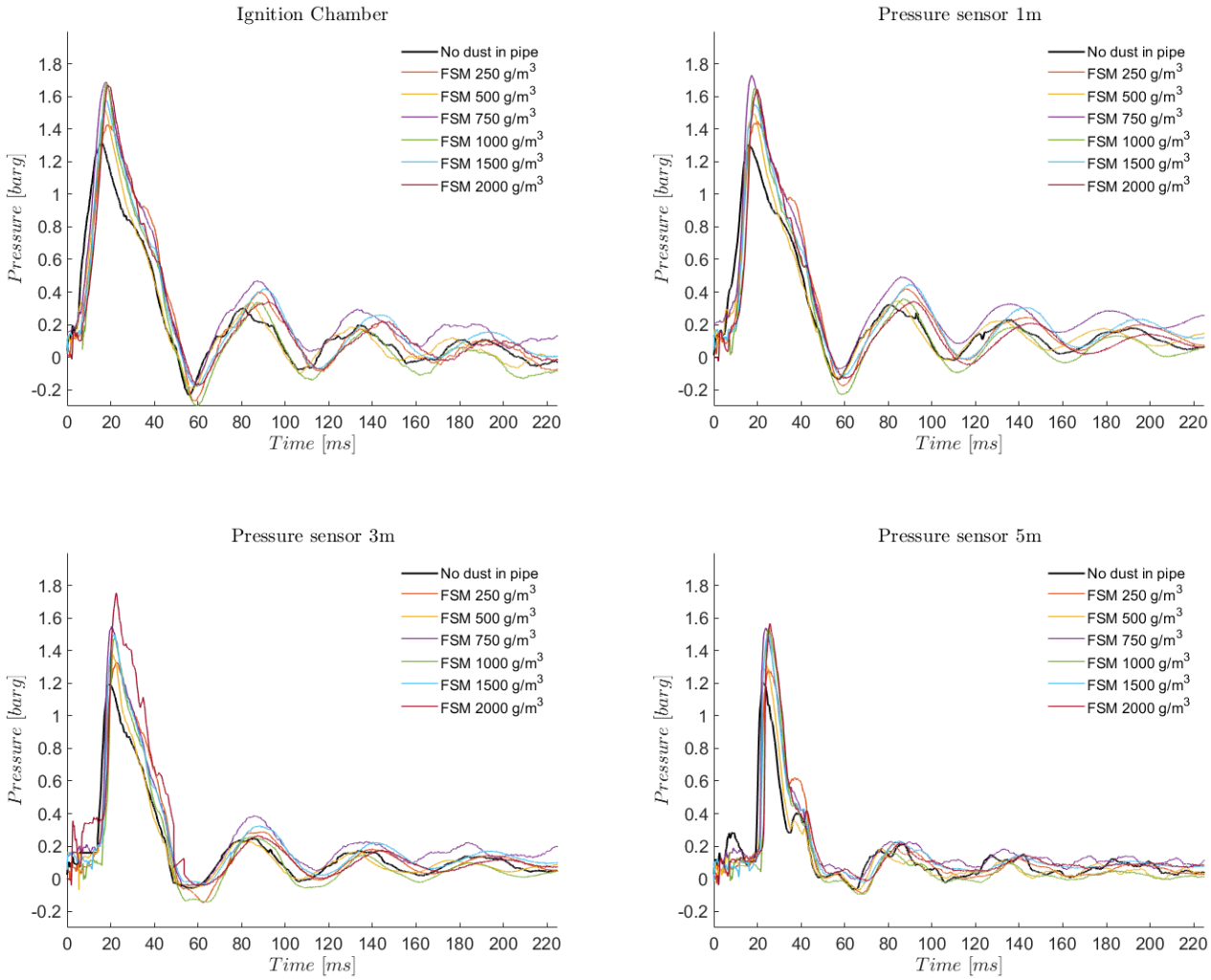

Figure 32: Explosion pressure in configuration 1 with layered FSM dust in varying concentration

In the experimental series presented in Figure 33, which was conducted using silicon dust in the DN250 pipe, an increased explosion pressure is observable upon the introduction of a dust layer. Despite this increase, the data does not establish a clear correlation between the concentration of the dust layer and the explosion pressure. Further, the comparison between silicon and FSM dust layers reveals no significant differential in the explosion pressure.

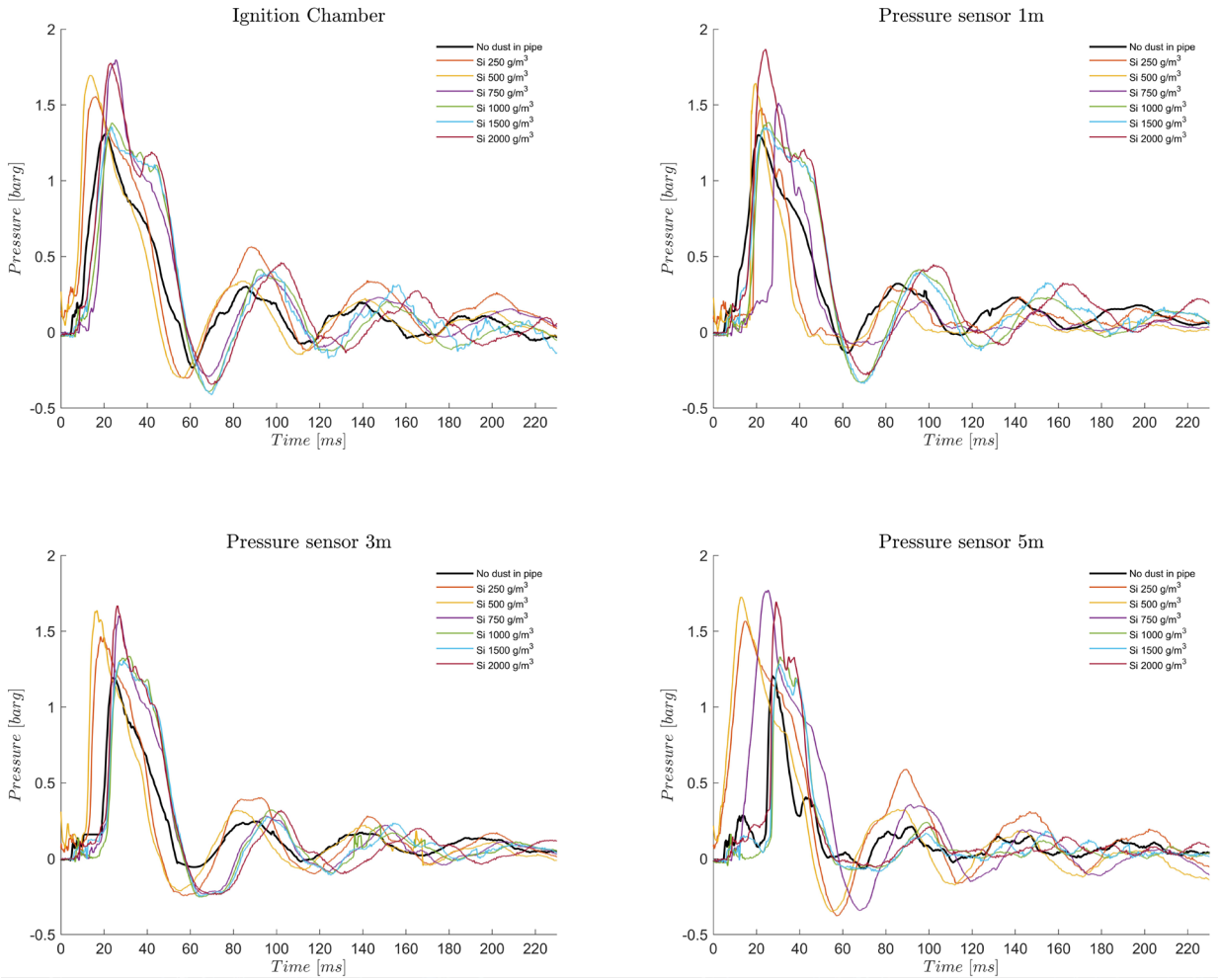

Figure 33: Explosion pressure in configuration 1 with layered silicon dust in varying concentration

4.2.2 Configuration 2

In this section the results from tests in configuration 2, consisting of the ignition chamber and the DN160 pipe will be presented.

Fireball

The test series conducted with FSM and silicon in the DN160 pipes, as depicted in Figure 34 and Figure 35 shows the same coupling between dust layer concentration and fireball length as observed in the DN250 pipe. The corresponding fireball length to each concentration is presented in Table 14.

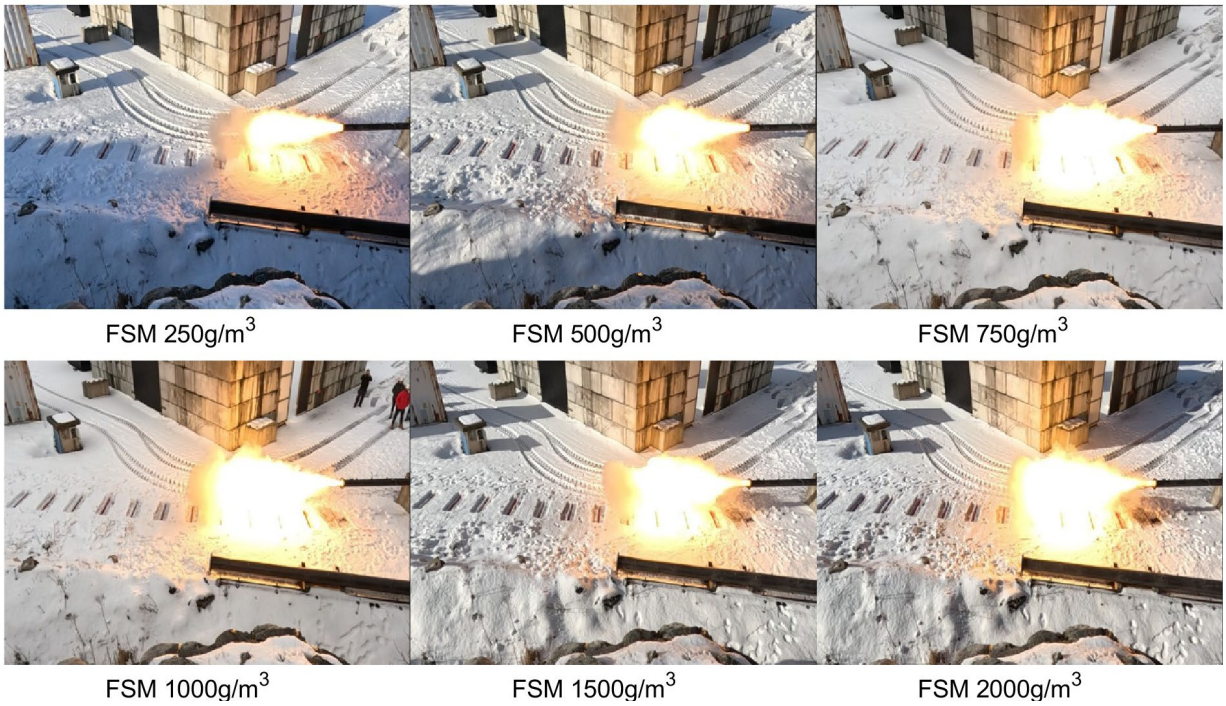

Figure 34: FSM fireball size in configuration 2 at different concentrations

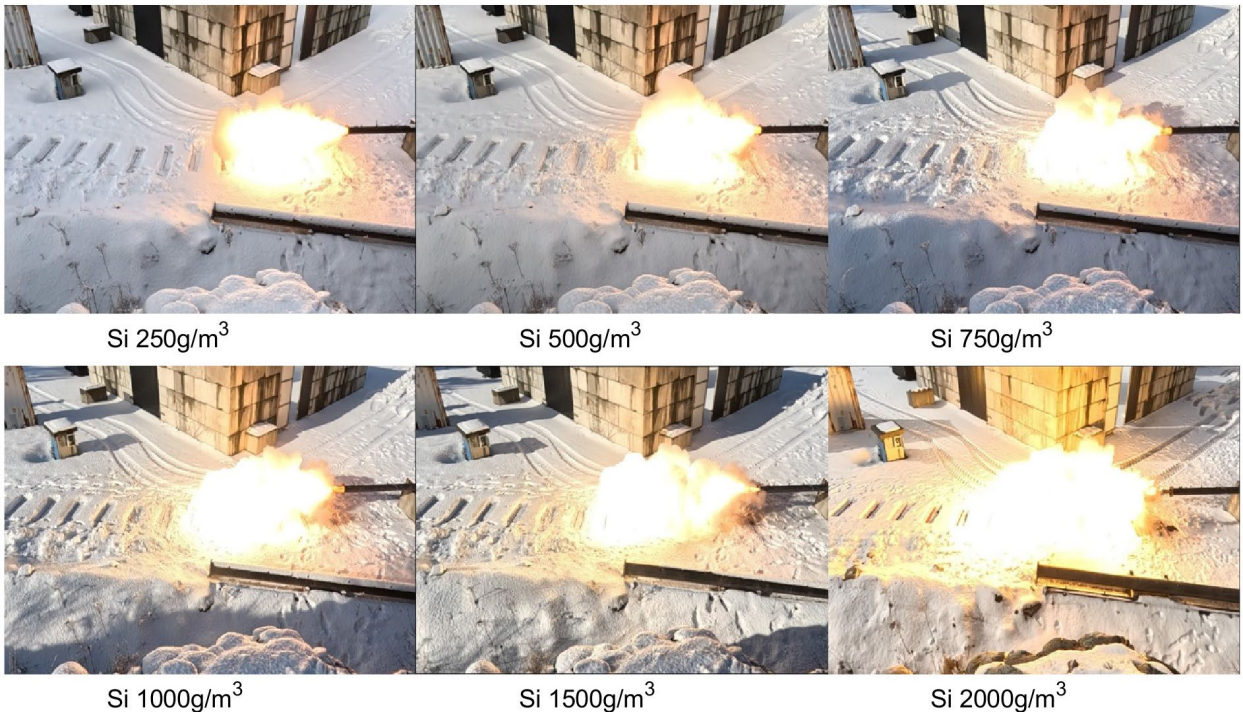

Figure 35: Si fireball size in configuration 2 at different concentrations

Table 14: Fireball length FSM and silicon in configuration 2

Concentration (g/m^3)	Fireball length FSM DN160 (m)	Fireball length silicon DN160 (m)
0	2.0	2.0
250	3	4.0
500	3.5	4.0
750	4.0	4.5
1000	4.5	5.0
1500	4.0	5.5
2000	4.5	6.0

In Figure 36 the fireball resulting from a concentration of 250 g/m^3 with FSM and silicon is compared to the fireball from the test with no dust in pipe.

Figure 36: Comparing fireball size in configuration 2 for 250g/m^3 of Si and FSM with no dust in pipe.

Explosion Pressure

The test series with FSM in the DN160 pipe reveals that the presence of layered FSM dust contributes to an increased explosion pressure within the pipe, as seen in Figure 37. Interestingly, the observed increase in pressure does not appear to be directly related to the dust layer concentration, as there is minimal variation in the explosion pressures across different concentrations.

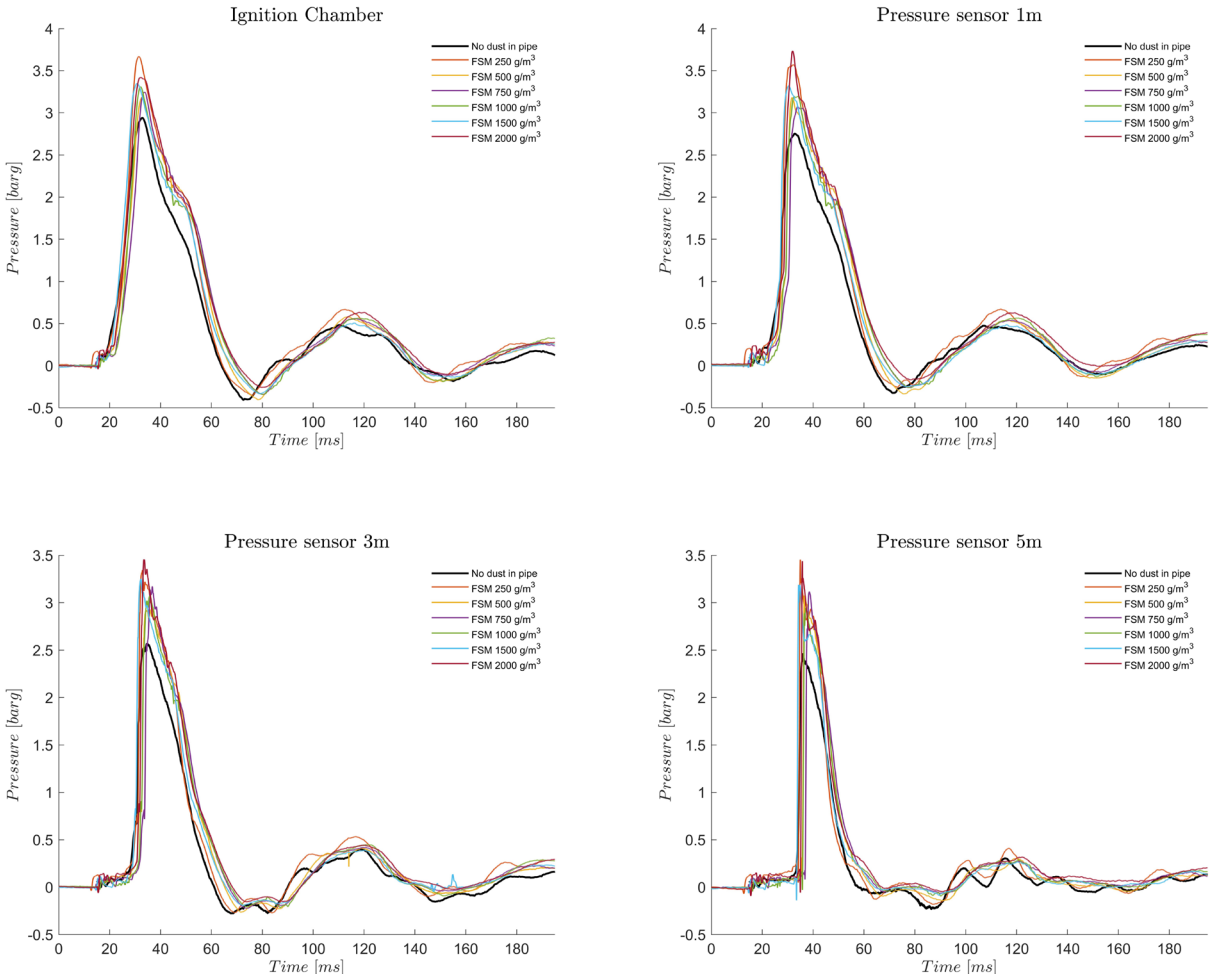

Figure 37: Explosion pressure in configuration 2 with layered FSM dust in varying concentration

The experimental series utilizing silicon dust exhibits an enhanced explosion pressure upon the introduction of a dust layer within the pipe, this can be seen in Figure 38. This pattern echoes the findings from the test with FSM, where a distinct correlation between the dust layer concentration and the resultant explosion pressure is absent. When compared with the FSM series, the silicon series registers slightly higher explosion pressures.

Moreover, an intriguing feature of the silicon series is the observation of a second explosion approximately 20 milliseconds succeeding the initial explosion, a pattern consistent across all dust layer concentrations. This phenomenon is detected by all the pressure transducers in use, except for the one located at the 5-metre mark.

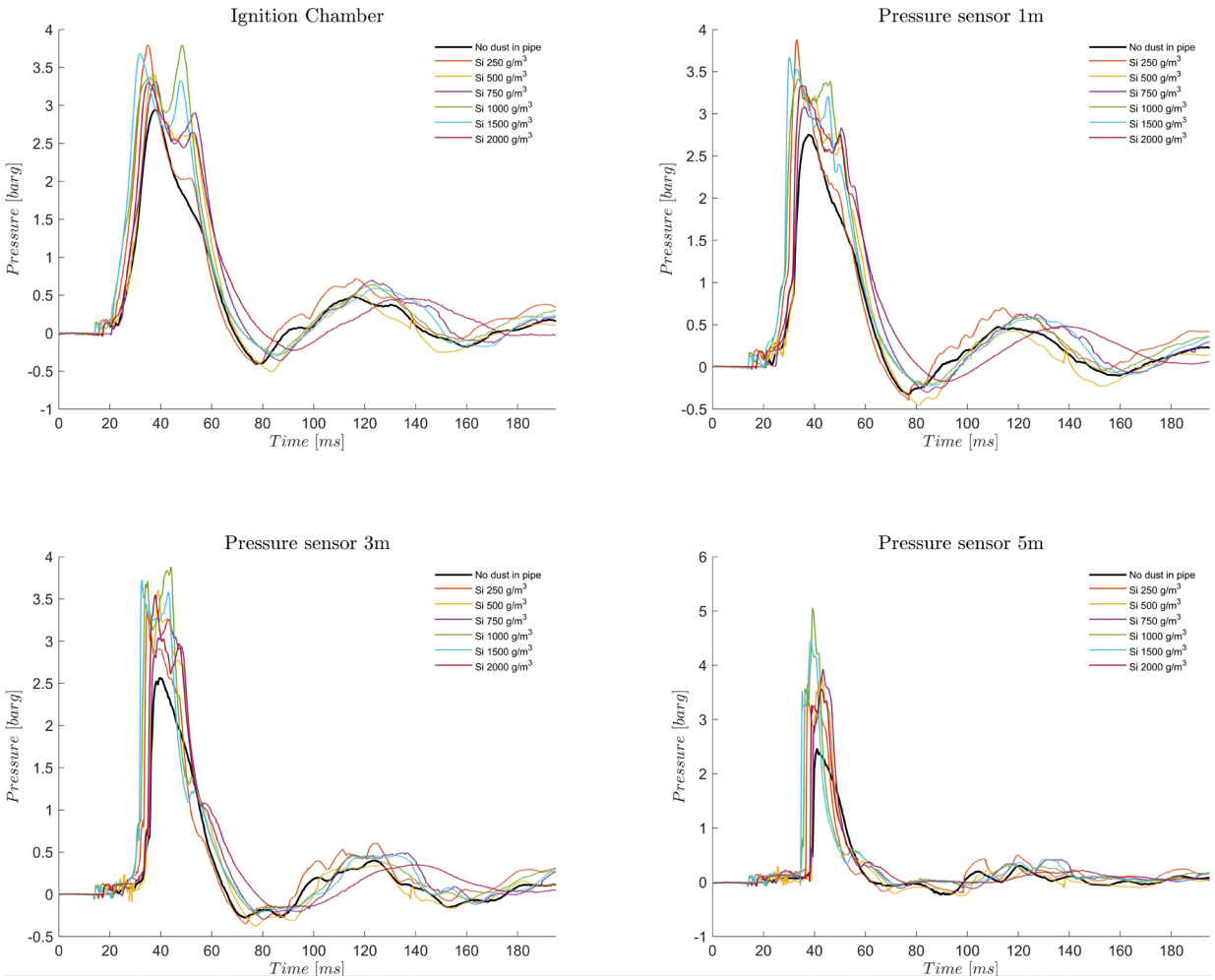

Figure 38: Explosion pressure in configuration 2 pipe with layered silicon dust in varying concentration

4.2.3 Configuration 3

In this section the results from tests in configuration 3, consisting of the ignition chamber and the DN250 pipe connected to the DN160 pipe will be presented.

Fireball

In the pipe configuration transitioning from DN250 to DN160, the flame stemming from the primary explosion within the ignition chamber was capable of propagation through both pipes, even in the absence of a dust layer, as illustrated in Figure 39. When a dust layer was present in the DN160 pipe, flame propagation was only possible through both pipes at a dust layer concentration of 500 g/m^3 for silicon.

However, the introduction of a dust layer with a concentration of 1000 g/m^3 to both pipes resulted in the formation of a substantial fireball. The lengths of the fireballs corresponding to each concentration are detailed in Table 15.

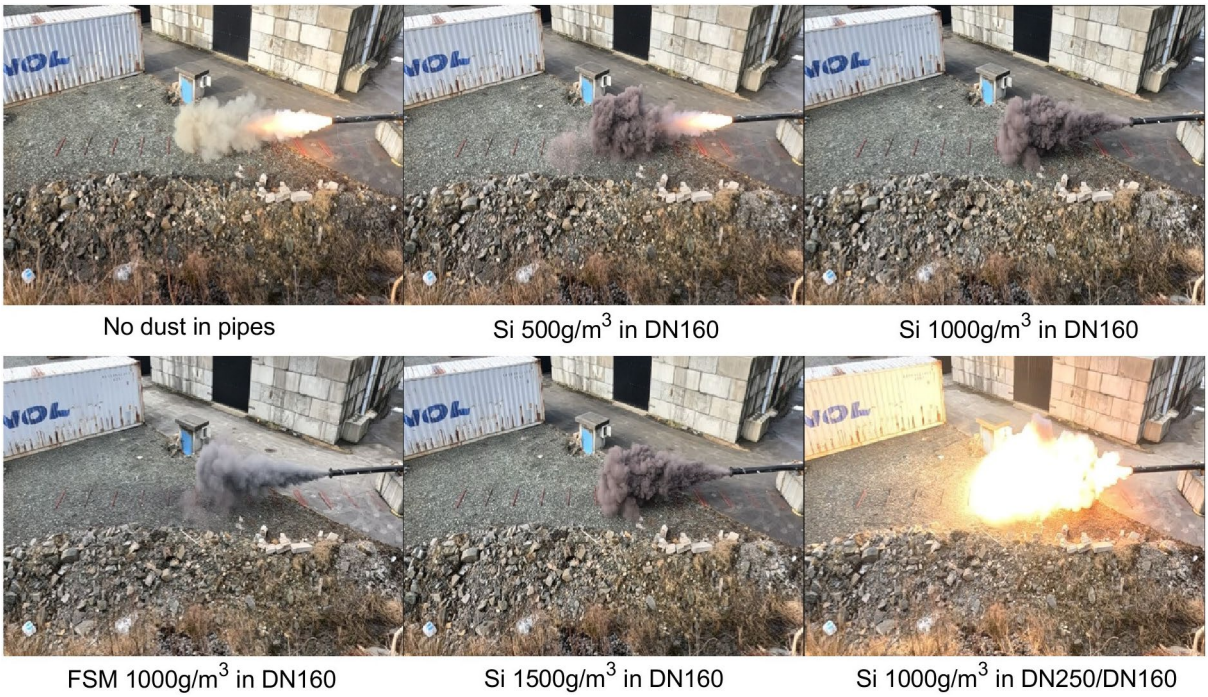

Figure 39: Comparing fireball size in configuration 3 for silicon and FSM, and with no dust in pipes.

Table 15: Fireball length FSM and silicon in configuration 3

Concentration in DN160 (g/m³)	Concentration in DN250 (g/m³)	Fireball length FSM DN160 (m)	Fireball length silicon DN160 (m)
0	0	2.0	2.0
500	0	Not tested	1.5
1000	0	0.0	0.0
1500	0	Not tested	0.0
1000	1000	Not tested	6.0

Explosion Pressure

The test series executed in the pipe configuration 3, as depicted in Figure 40, displays a negligible variation in explosion pressure when contrasting dust layer concentration and dust type with the test involving no dust layer. Upon introduction of a dust layer concentration of 1000 g/m^3 to both pipes, a second explosion is observed roughly 30 milliseconds after the initial explosion in the ignition chamber. This results in an amplified explosion pressure throughout the entire system.

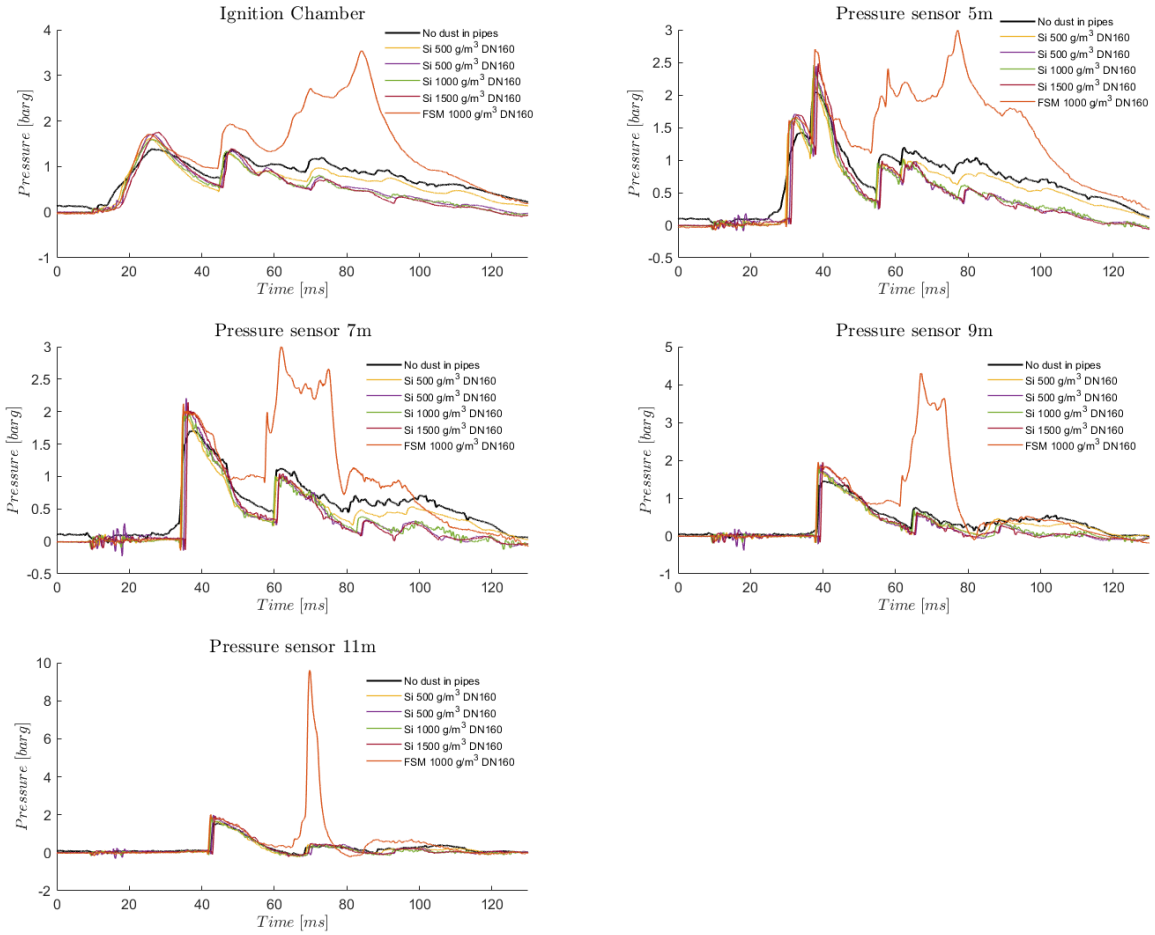

Figure 40: Explosion pressure in configuration 3 with layered dust in varying concentration.

4.2.4 Configuration 4

In this section the results from tests in configuration 4, consisting of the ignition chamber and the DN160 pipe connected to the DN250 pipe will be presented.

Fireball

In the configuration with pipes transitioning from DN160 to DN250, the initial explosion from the ignition chamber was able to continue through both pipes, even when a dust layer was not present, like in configuration 3 with DN250-to-DN160 pipes. This can be seen in Figure 41. There was a correlation observed between the dust layer concentration and the length of the fireball, like in the tests conducted solely in the DN250 and DN160 pipes. However, this correlation was not as strong. The dust layer concentration and corresponding fireball length is presented in Table 16. Unfortunately, due to technical issues, no footage is available for the fireball from the test involving 1000 g/m^3 Si in both pipes.

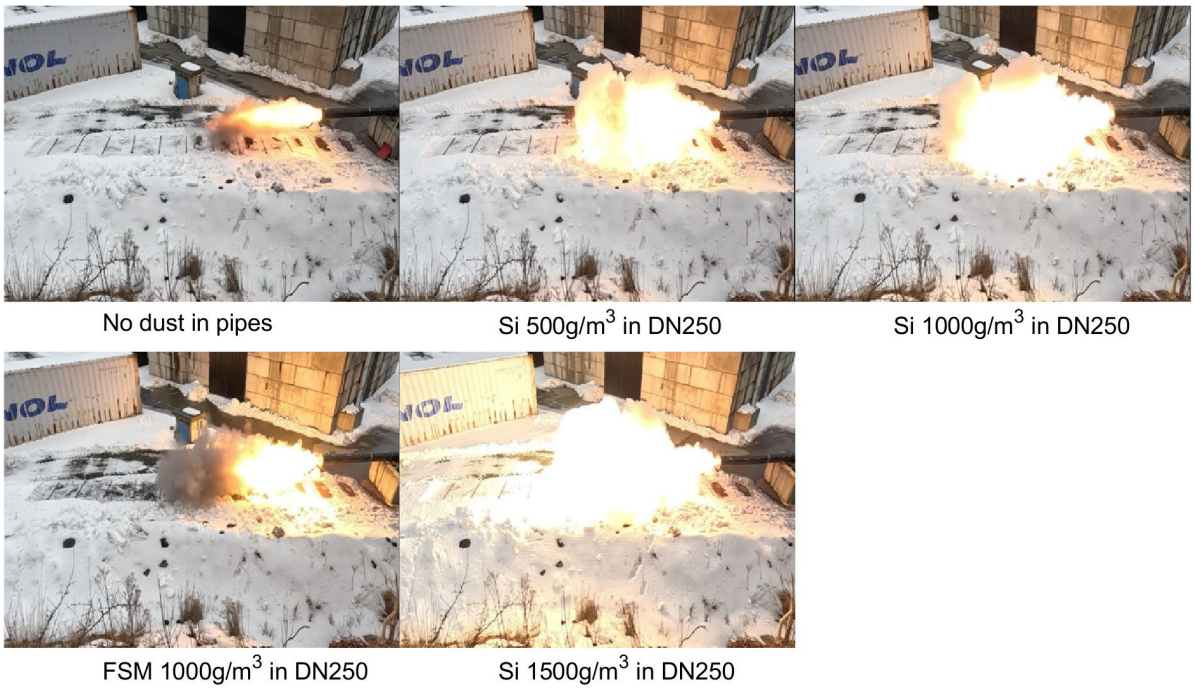

Figure 41: Comparing fireball size in configuration 4 for Si and FSM, and with no dust in pipes.

Table 16: Fireball length FSM and silicon in configuration 4

Concentration in DN160 (g/m³)	Concentration in DN250 (g/m³)	Fireball length FSM DN160 (m)	Fireball length silicon DN160 (m)
0	0	3.0	3.0
0	500	Not tested	5.0
0	1000	3.0	5.5
0	1500	Not tested	6.5

Explosion Pressure

The explosion pressure findings from the DN160 to DN250 configuration, as depicted in Figure 42, indicate only slight differences between the test with no dust in the pipes and a concentration of 1000 g/m^3 of layered FSM dust in the DN250 pipe. When silicon dust was introduced as a dust layer in the DN250 pipe, a second explosion occurred around 40 milliseconds after the initial explosion the ignition chamber, this was present for all three concentrations in the DN250 pipe. Layering both pipes with 1000 g/m^3 of silicon dust led to a slight increased peak explosion pressure and extended the duration of the pressure.

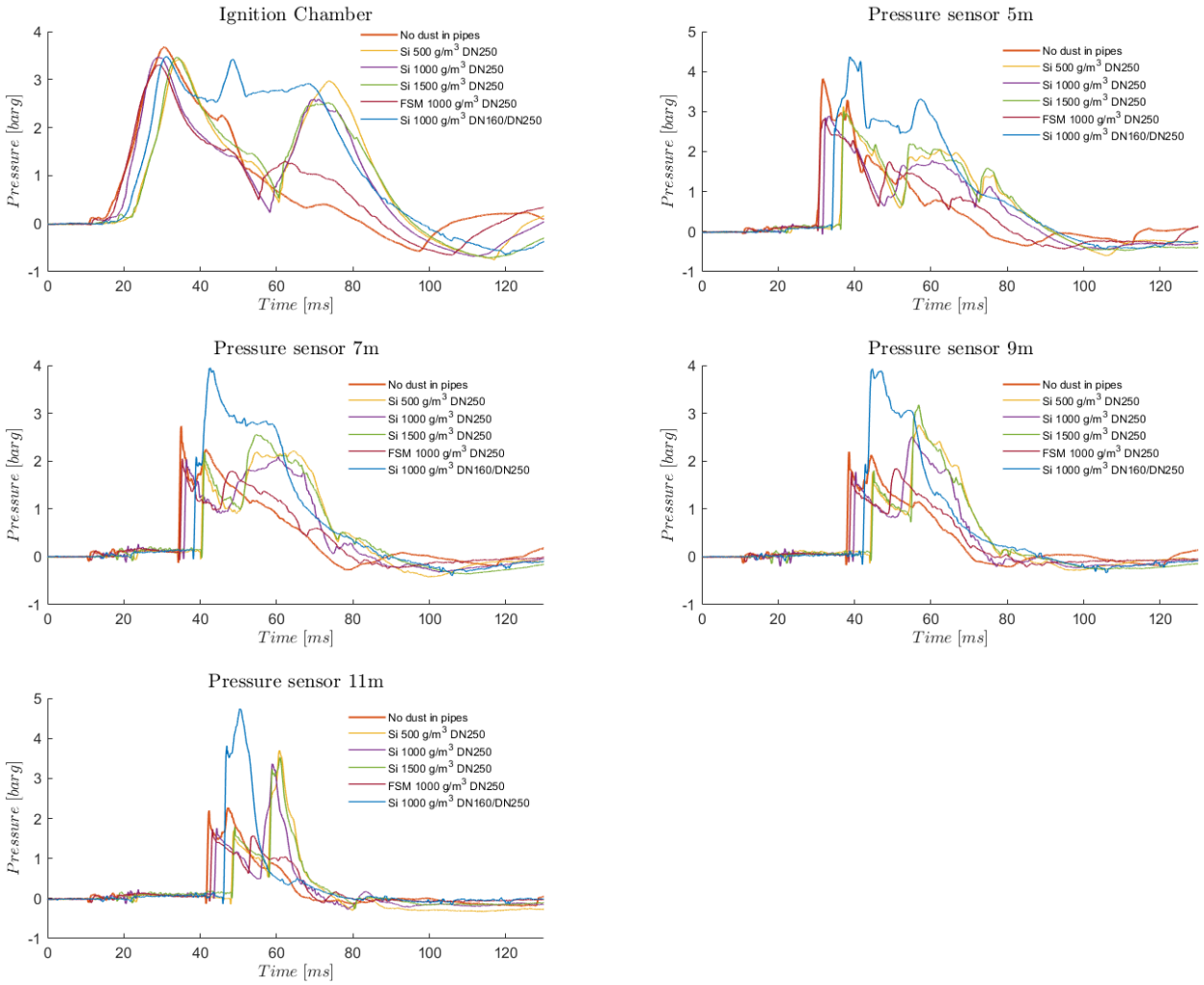

Figure 42: Explosion pressure in configuration 4 with layered dust in varying concentration

4.2.5 Configuration 5

In this section the results from tests in configuration 5, consisting of the ignition chamber and the DN250 pipe connected to the DN160 pipe with the DN160/DN60 crossover attached will be presented. Figure 43 presents the explosion pressure for configuration 5. The removal of the two 6-metre DN60 pipes from the setup, while retaining the DN60 crossover, resulted in a considerably lower explosion pressure compared to the configuration that included the two DN60 pipes.

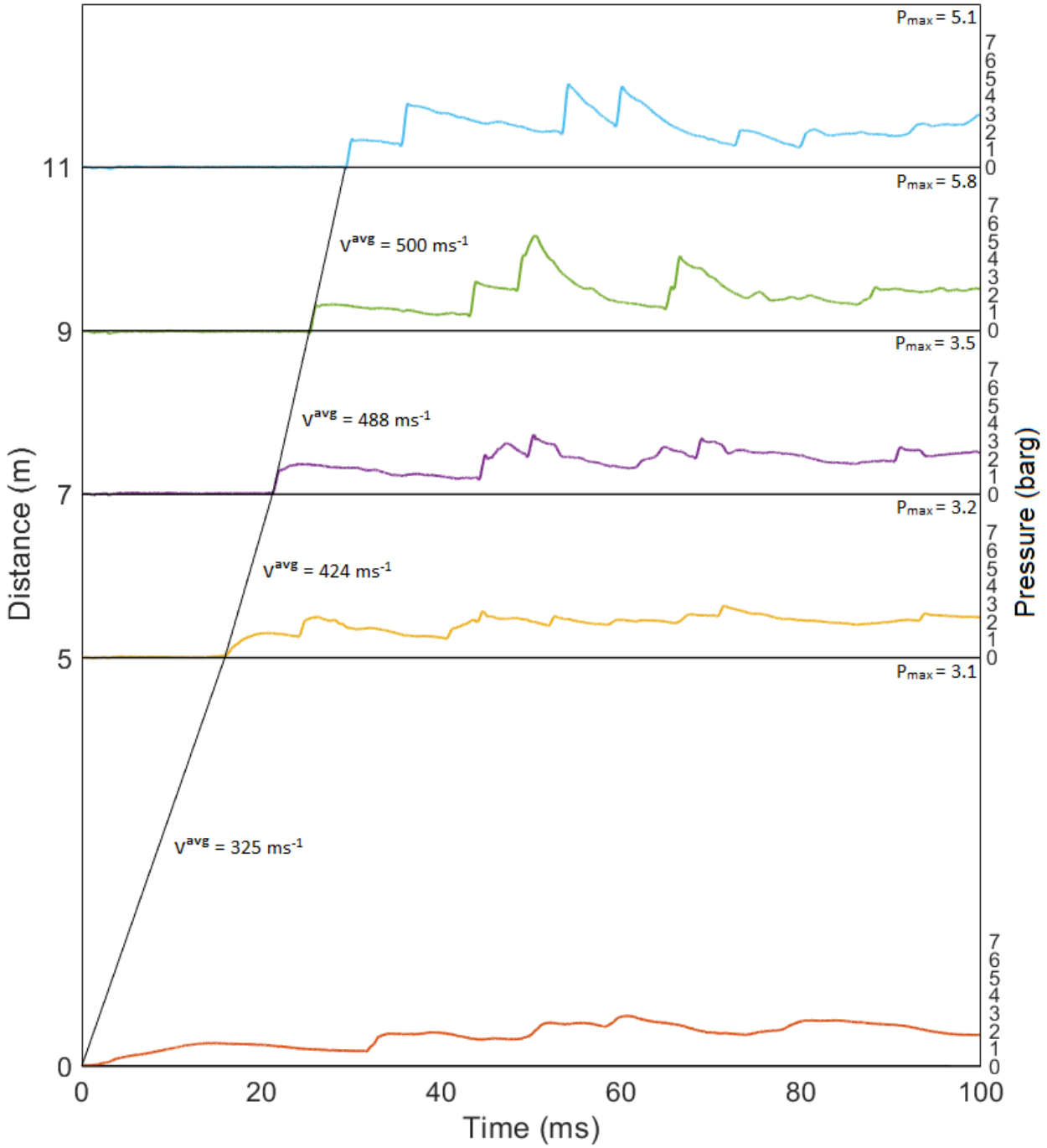

Figure 43: Explosion pressure for 1000 g/m^3 layered Si in configuration 5.

Figure 44 provides a comparison of the dust cloud formation outside the pipe just before ignition for setups both with and without the DN160/DN60 crossover attached. These images were captured approximately 4 millisecond (one frame) prior to the flame exiting the pipe. The configuration including the DN160/DN60 crossover demonstrated a substantially larger and less dense external dust cloud preceding ignition.

Figure 44: Comparison of dust cloud exiting the DN160 pipe with and without DN160/DN60 crossover.

4.2.6 Configuration 6

In this section presents the results from experiments conducted in Configuration 6, which consists of DN250-to-DN160-to-DN60 pipes. Tests #1 and #2 were conducted in late March. Due to the intriguing results from these initial tests, we conducted additional tests, namely Tests #3, #4, and #5, in late May. However, the time available for data interpretation for these later tests was limited.

Fireball

In the 25-metre configuration, with DN250-to-DN160-to-DN60, the flame successfully propagated through all the pipes during test #1 with silicon dust and the test with FSM dust, as seen in Figure 45. However, in test #2 with silicon dust, no fireball was observed outside the pipes, only sparks. An external fireball could also be observed for the configuration with only the DN160/DN60 crossover attached, and not the two 6-metre DN60 pipes.

DN250/DN160/DN60 Si 1000g/m^3 Test 1

DN250/DN160/DN60 Si 1000g/m^3 Test 2

DN250/DN160/DN60 FSM 1000g/m^3

DN250/DN160 With DN60 Crossover Si 1000g/m^3

Figure 45: Comparing fireball size in configuration 6 for Si and FSM, and configuration 5

Figure 46 illustrates the dust cloud emerging from the DN60 pipe in Test #1, which involved a dust layer of 1000 g/m³ Si. The figure highlights a significant shift in the dust cloud's colour as the explosion progresses through its various stages. Initially, the cloud presents a dark grey hue prior to ignition. This shifts to white as the flame propagate through it, and ultimately transitions to brown when the combustion products are ejected from the system.

Figure 46: Dust cloud observed in Test #1 with silicon in configuration 6.

Explosion Pressure

This section will present the explosion pressure results from the experiments conducted using configuration 6.

Explosion Pressure Test #1 Silicon

Figure 47 shows the explosions pressure measured in test #1, in the DN250-to-DN160-to-DN60 configuration. The pressure transducers were during test #1 set to 20 barg. The transducers situated at 11, 15 and 21 metres reached saturation, as evident from pressure graphs, resulting in a pressure reading of 21.1 barg for all three transducers. The plots in the figure are distance scaled.

In test #1, a fast transient wave propagating downstream from the ignition chamber can observed, exhibiting an average velocity of about 500 $m \cdot s^{-1}$. The pressure graph for the transducer located at 11-metres reveals a sudden increase in pressure, followed by a decline before experiencing another abrupt rise, resulting in oscillations in the pressure readings. This event is succeeded by the emergence of an upstream and downstream shock wave.

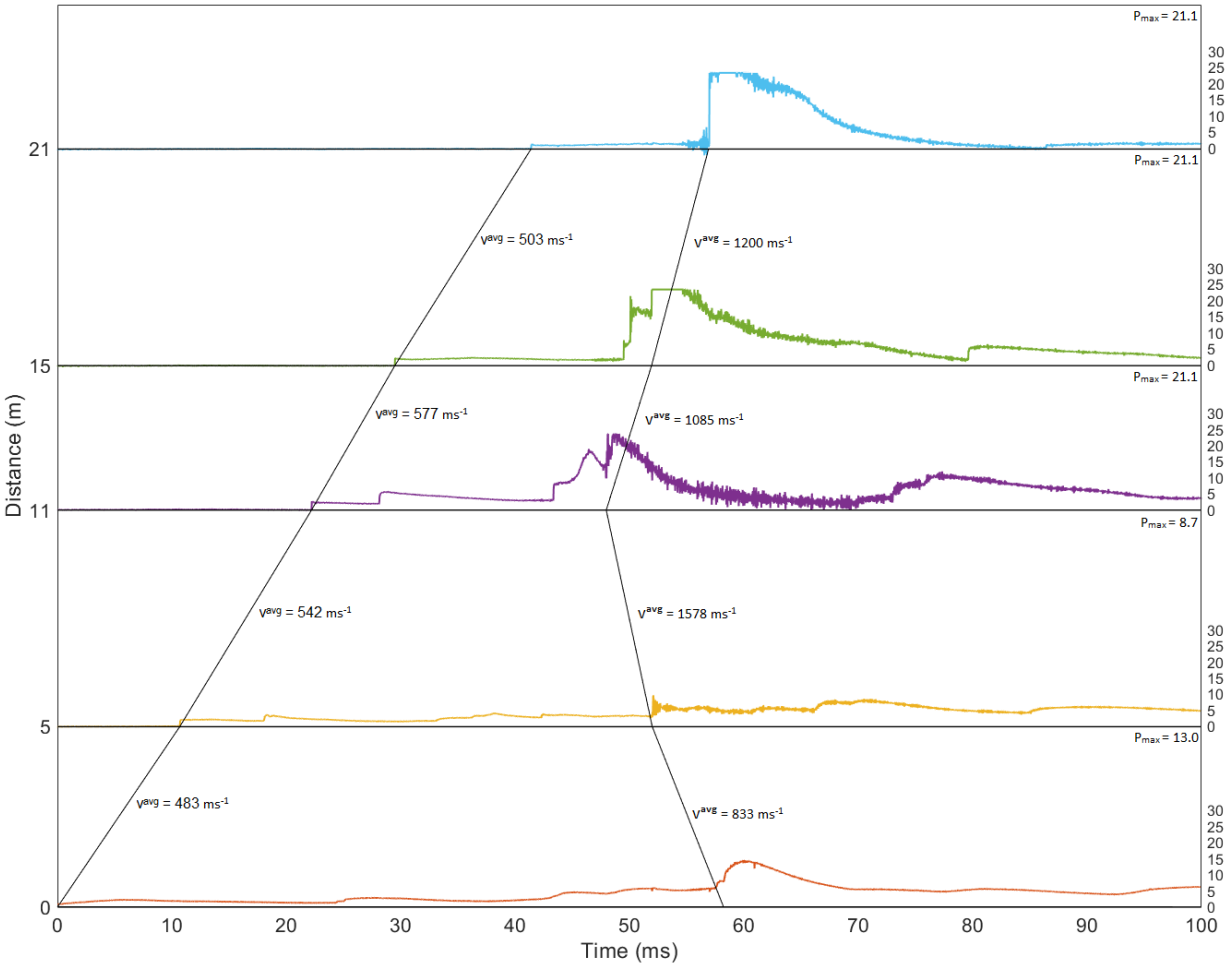

Figure 47: Explosion pressure for test #1 with 1000 g/m^3 with layered Si in configuration 6 using raw data, distance scaled.

Explosion Pressure Test #2 Silicon

For Test #2, the pressure transducers were set to 50 barg. As shown by the graph for the 11-metre transducer in Figure 48, it reached saturation, with the peak recorded pressure reading being 52.8 barg. The plots in the figure are distance scaled.

Like in Test #1, it can be seen in Figure 48, that Test #2 shows a fast transient wave propagating downstream from the ignition chamber, with an average velocity above 500 m·s^{-1}. The pressure graph for the transducer situated at 11-metres shows a sudden increase in pressure, followed by a decline and another abrupt rise. This sequence of events is followed by the appearance of an upstream shock wave and an additional downstream shock wave. It is noteworthy that the transducer at 21-metres in Test #2 presents lower peak pressures compared to Test #1, while the transducers at 5 and 0 metres display slightly elevated pressures in comparison to Test #1. The transducer at 11-metre showed increased oscillation

in the readings, compared to test #1, the opposite can be observed for the transducer at 15-metre.

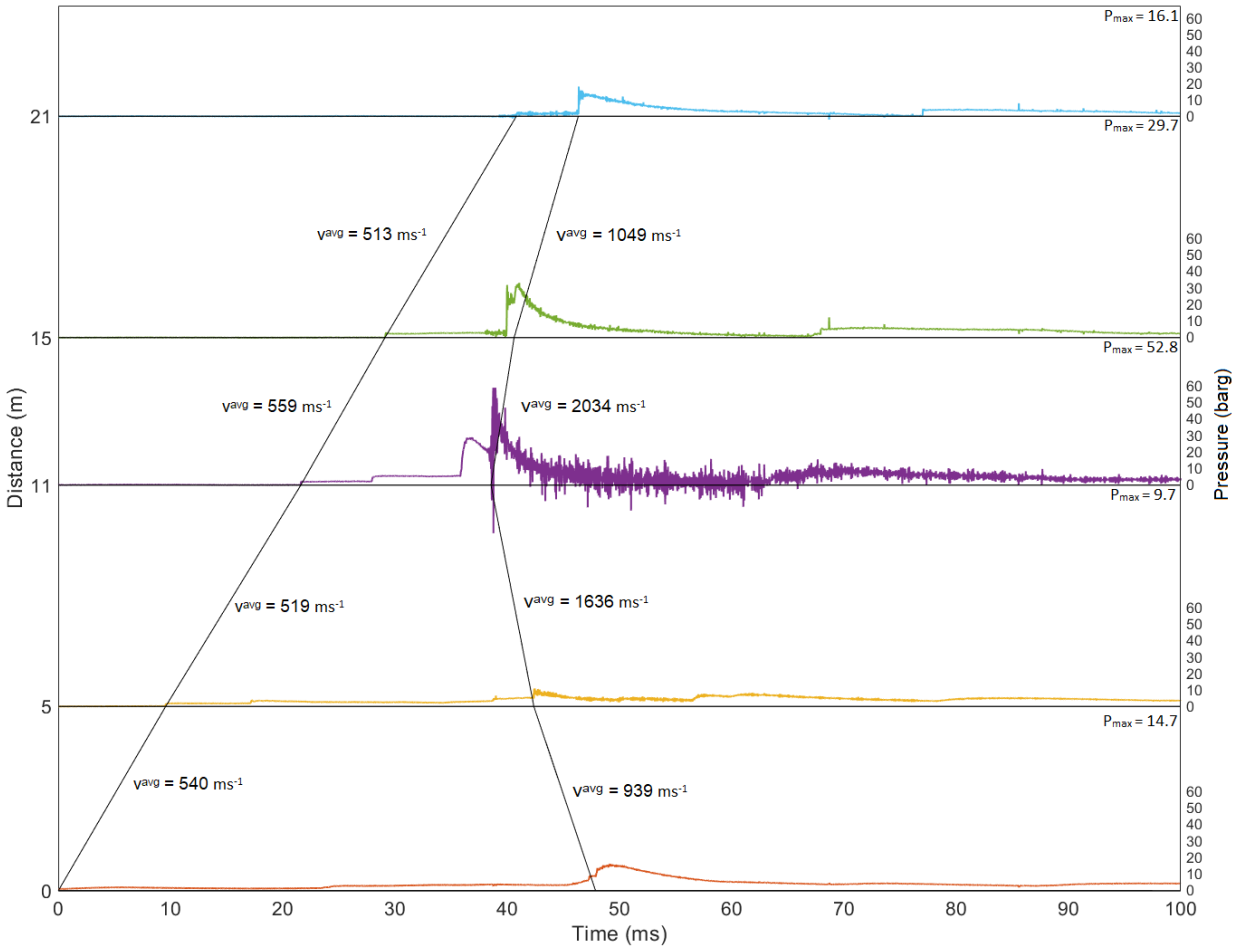

Figure 48: Explosion pressure for test #2 with 1000 g/m³ layered Si in configuration 6 using raw data, distance scaled.

Explosion Pressure Test #3 Silicon

Observations of high pressures during tests #1 and #2 necessitated further testing, incorporating variations in transducer placement and an additional transducer. The range of the transducers were also adjusted to 250 barg. In tests #3, #4, and #5, the proximity of the transducer precluded the use of distance-scaled plots, thus making lines indicating the pressure wave arrival time as an illustration only. Upon analysis of the results, it became apparent that the transducer in the ignition chamber malfunctioned. As a result, pressure data

from the ignition chamber was not available and therefore not included in the plots for tests #3, #4, and #5.

In test #3 the pressures were notably lower than in test #1 and #2, except for the transducer located at 21-metre which reached a maximum pressure of 47.4 barg, as depicted in Figure 49. The red dotted line is meant as an illustration to show the oscillations occurring simultaneously across multiple transducers as the peak pressure can be observed at the 21-metre transducer. The high pressure reading at the 21-metre mark in test #3 raised concerns that this reading could be attributed to acceleration compensation within the transducer. To mitigate this, in test #4 and #5 the DN60 pipes was additionally secured to two tractor tires to prevent any pipe movement and to dampen potential vibrations.

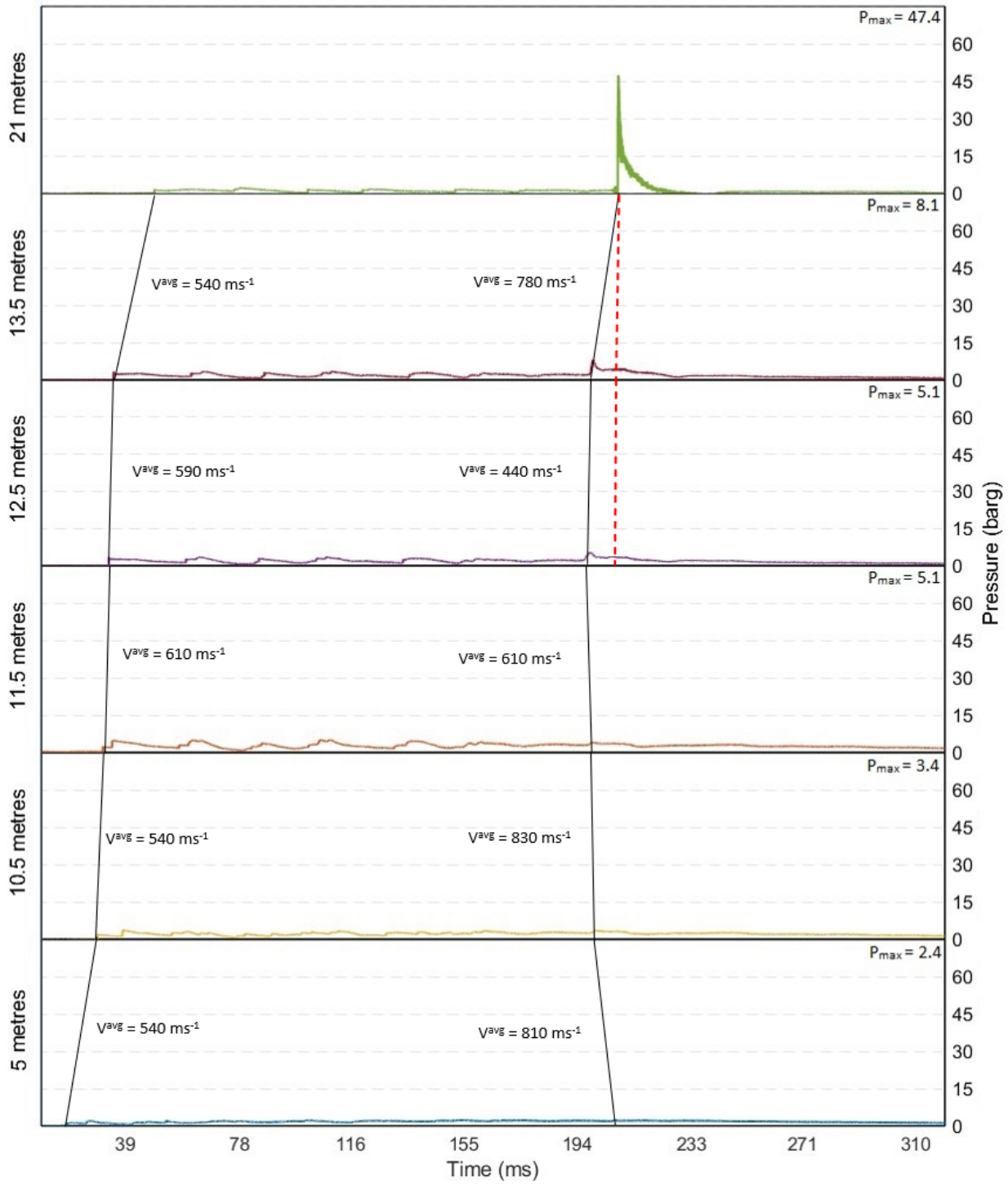

Figure 49: Explosion pressure for test #3 with 1000 g/m^3 layered Si in configuration 6 using raw data.

Explosion Pressure Test #4 Silicon

Test #4 exhibited pressure curves which closely resembled those of test #1 and #2, except for the 21-metre transducer, which reached a maximum pressure of 104 barg, as depicted in Figure 50. The red dotted line is meant as an illustration to show that the oscillations occur simultaneously across multiple transducers.

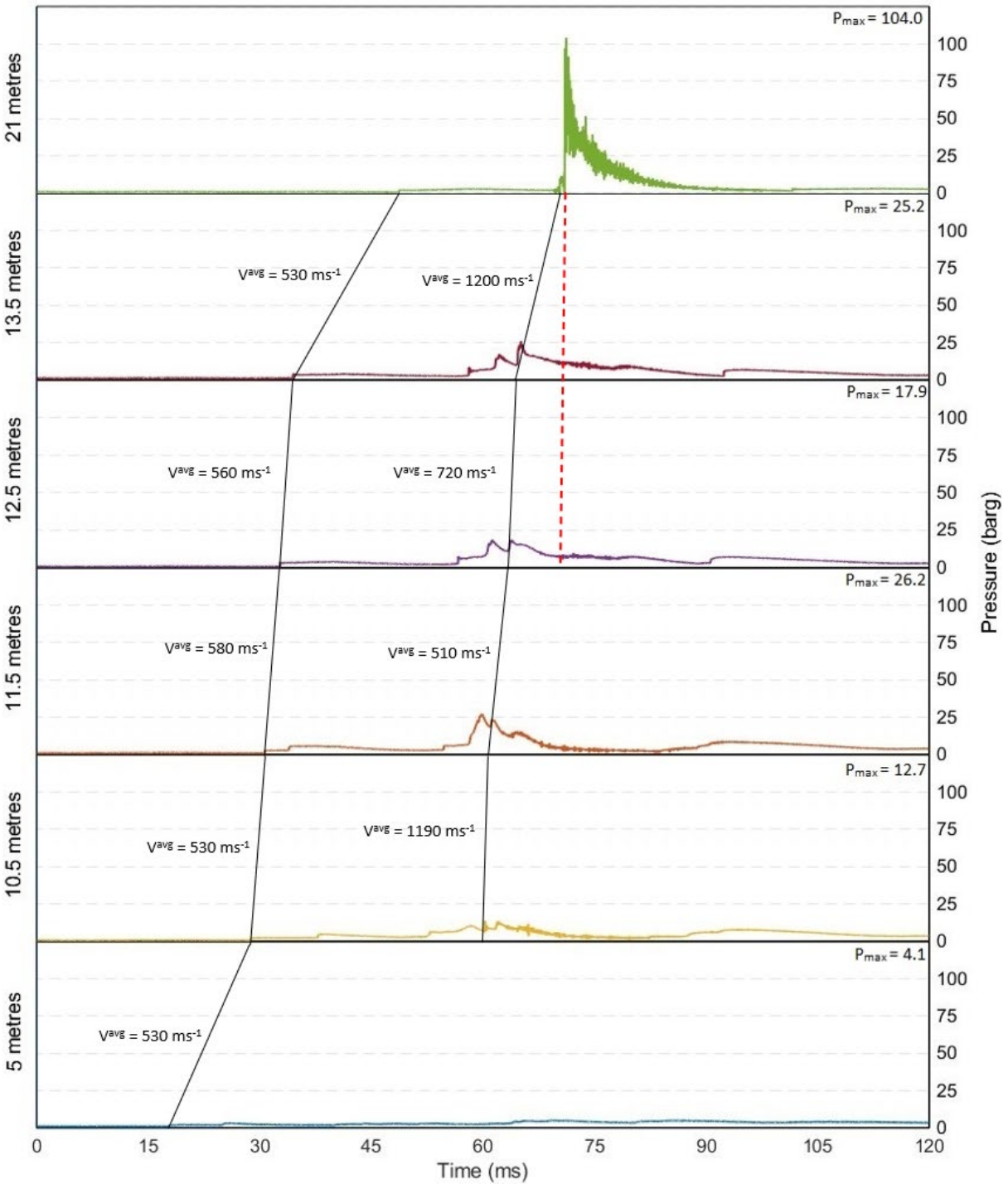

Figure 50: Explosion pressure for test #4 with 1000 g/m^3 layered Si in configuration 6 using raw data.

Explosion Pressure Test #5 Silicon

In test #5, the silicon dust layer was increased to 5000 g/m^3. This resulted in an elevated pressure across all transducers, except for the transducer at the 21-metre mark, when compared to the previous tests, as seen in Figure 51. The maximum explosion pressure was observed at the 11.5-metre transducer and was measured to be 66.4 barg.

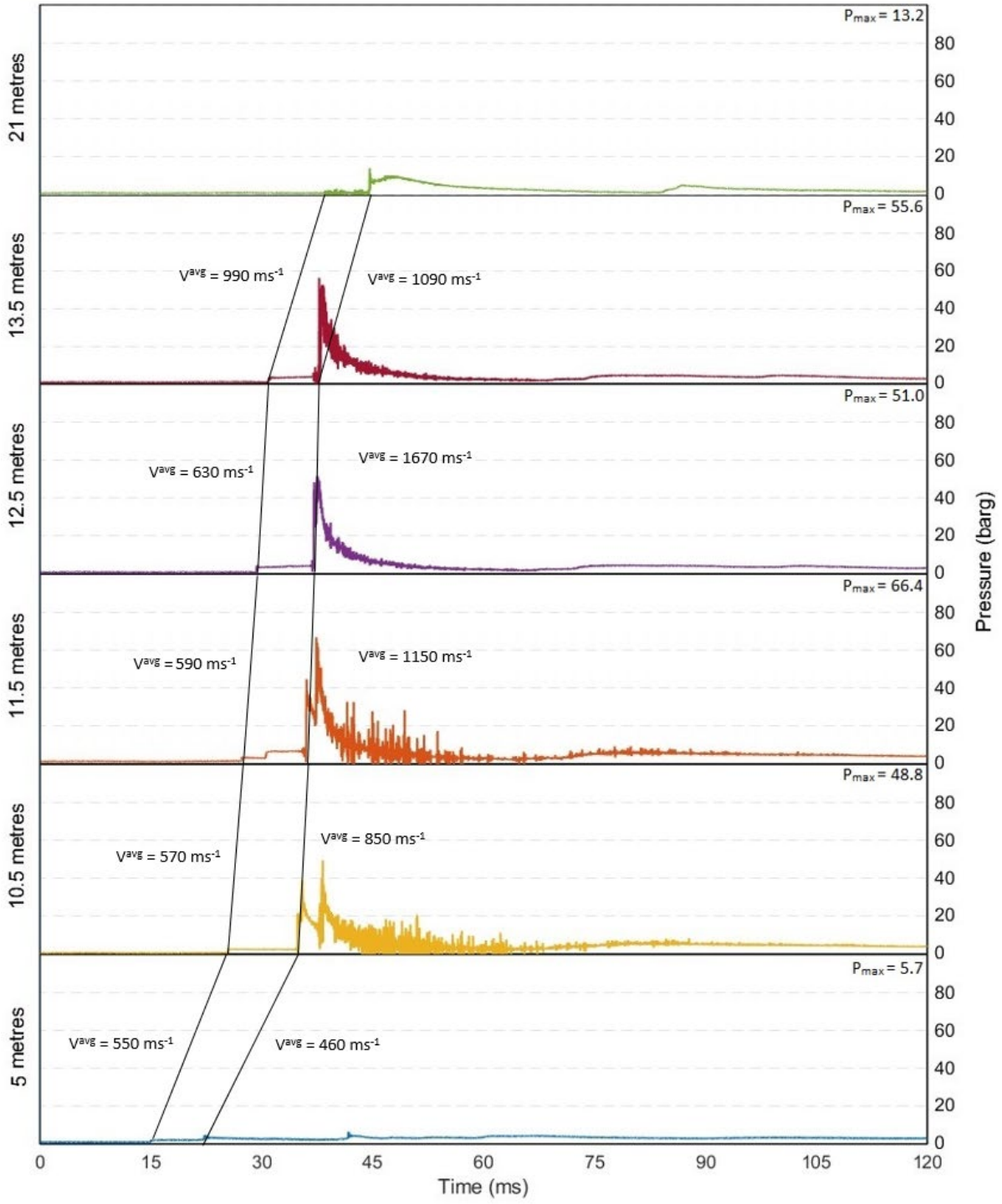

Figure 51: Explosion pressure for test #5 with 5000 g/m^3 layered Si in configuration 6 using raw data.

Explosion Pressure FSM

As demonstrated in Figure 52, in the DN250-to-DN160-to-DN60 configuration with a dust layer of 1000 g/m^3 FSM, the peak explosion pressure was notably lower than that in tests with silicon dust.

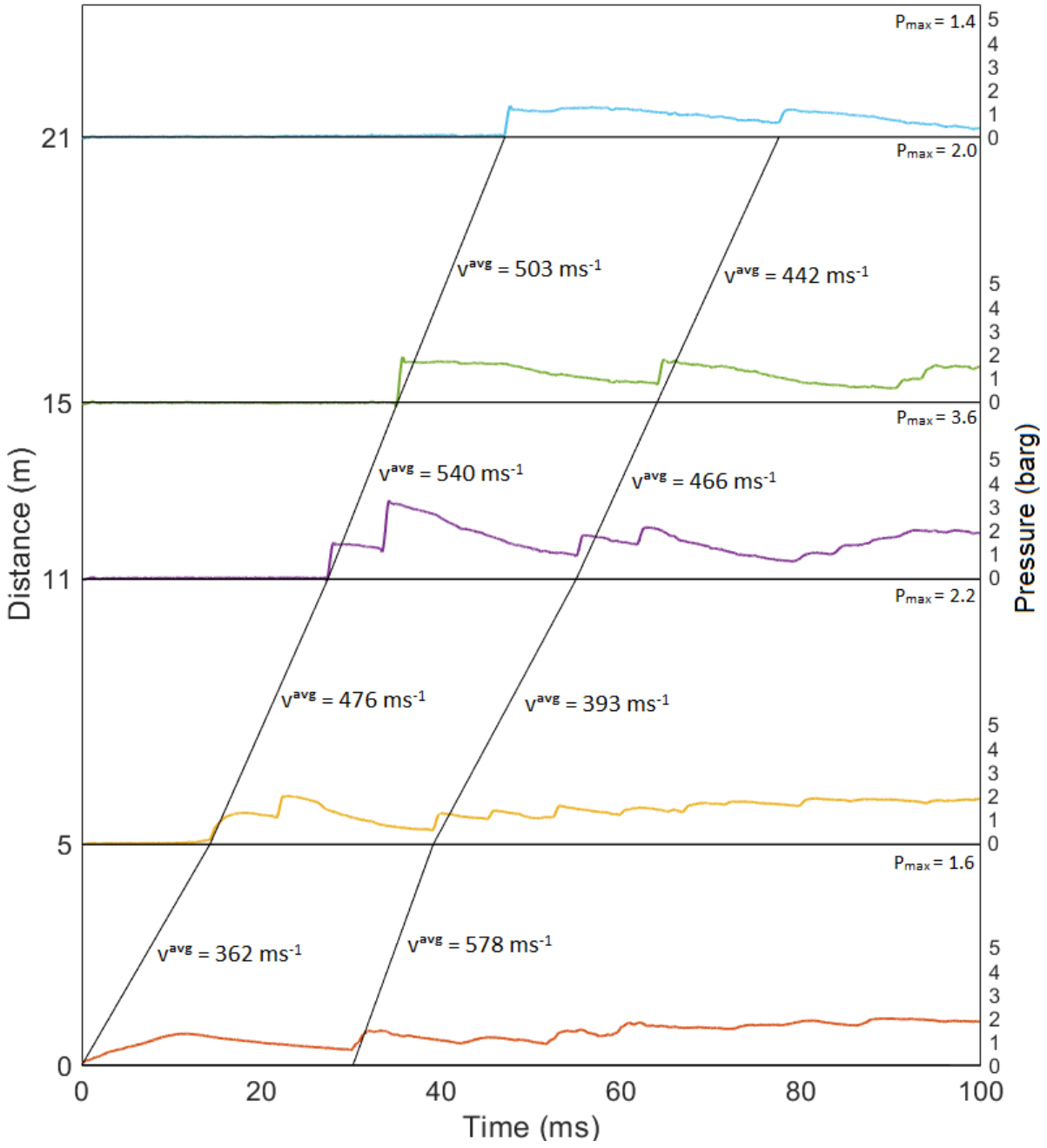

Figure 52: Explosion pressure for 1000 g/m^3 layered FSM in configuration 6.

4.3 Simulation

The Chapman-Jouguet (C-J) detonation velocity for the stoichiometric mixture of silicon and air was estimated through the methodology described in section 3.6. The calculated C-J velocity was found to be approximately 2100 $m \cdot s^{-1}$.

It is important to emphasize that this value should be treated as an approximation, given the model's simplifying assumptions. Primarily, the model presupposes that the combustion of silicon occurs entirely in the gaseous phase, thus likely overestimating the C-J velocity. This is because potential reactions occurring in other phases and heat loss due to silicon particle melting are not accounted for.

Nonetheless, this estimation serves as a valuable preliminary insight into the dynamics of a silicon-air detonation. Future efforts to construct a more comprehensive thermodynamic model that accounts for other phases and additional heat loss factors would lead to a more precise calculation of the C-J velocity.

5 Discussion

This chapter will discuss and compare the laboratory-scale and large-scale experiments to relevant literature and previous work.

5.1 Laboratory-Scale Experiments

When comparing the results for both dust types, silicon dust exhibited higher explosion pressure than the FSM dust and a higher rate of pressure rise as illustrated in Figure 53.

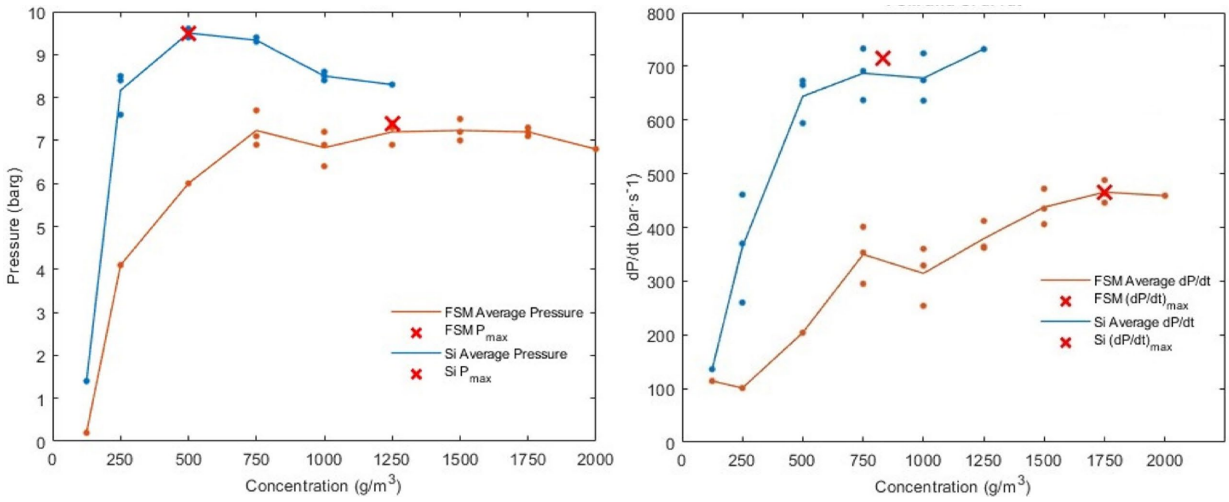

Figure 53: Comparing P_{max} (left) and dP/dt (right) for silicon and FSM.

The differences in explosion severity could be the variance in median particle sizes between the two dust types. The silicon dust has a smaller median particle size of 2.65 µm, compared to 9.71 µm for FSM. However, other factors like chemical composition and particle shape, might also contribute to the observed explosion behaviour differences.

The LEL values for both silicon and FSM dust were determined to be 100 g/m^3. This finding is somewhat surprising considering the higher explosion severity observed for silicon dust. The presence of magnesium in the FSM dust, known for its high reactivity, may increase its ignition sensitivity.

There are several potential sources of error in the results obtained with the 20-litre apparatus. Some include variations in dust dispersion within the sphere, measurement equipment inaccuracies, experimental condition inconsistencies, and potential sample contamination. Factors such as residual deposits of burned or unburned dust can influence the results,

highlighting the importance of proper apparatus cleaning for repeatability. Furthermore, the absence of water cooling in the vessel and the rudimentary temperature checking method may lead to test condition variations, affecting the results' repeatability and reliability.

To minimize these errors, it is essential to maintain a consistent, well-controlled experimental setup and ensure proper calibration of measurement equipment. Regular, thorough cleaning of the apparatus between tests can help eliminate residual dust influence on the results. Implementing more precise temperature control methods, like using thermocouples or infrared thermography, and incorporating water cooling systems, could help reduce temperature variations and increase testing efficiency. These improvements would contribute to more accurate and reliable data collection.

The experimental results for silicon dust in the 20-litre apparatus are in reasonable agreement with those reported by Skjold (2003) and Østgård (2022) for silicon dust with comparable particle sizes and chemical compositions. Unfortunately, no previous studies have investigated FSM with the specific silicon, iron, and magnesium chemical composition. Eckhoff (2003) listed in the appendix of his book a FSM dust with a 24% iron, 47% silicon and 17% magnesium composition, that exhibited much higher explosion pressures and K_{St} values than the FSM dust used in this study, which has composition of 33% iron, 47% silicon and 9% magnesium. The difference in K_{St} and explosion pressure is likely due to the increased magnesium content and decreased iron content, it could also be caused by the unknown chemical rest composition. However, given the strong alignment between the results obtained for silicon dust in this study and those in previous studies by Skjold and Østgård, there are no reason to doubt the test procedures or methods used to obtain the FSM results.

5.2 Large-Scale Experiments

This section will discuss the results from the large-scale experiments. The findings will be compared with established theories and previous research.

5.2.1 Fireball Characteristics

Given that the only measurements available for the fireball size are the maximum flame length, it is challenging to compare these results with those obtained by Holbrow et al. (2000). Holbrow suggested that there is no strong correlation between explosion characteristics and thermal radiation. Generally, a more saturated (brighter) photo is indicative of higher flame temperature and, consequently, greater thermal radiation. By comparing figures 29 and 30, it becomes clear that the silicon flame burns more brightly than that of the FSM, suggesting higher thermal radiation, as expected due to the high iron content in FSM which has a lower flame temperature than silicon. The results also shows that the expected fireball is much larger for alle concentrations and configurations for silicon than FSM. This could potentially suggest a relationship between the explosion characteristics and safe distance of fireballs from metal and metalloid dusts. However, further research is required to confirm whether this relationship is valid for other metal and metalloid dust.

5.2.2 Configuration 1 and 2

Examining the test results involving single pipes, specifically configuration 1 and 2, illustrated in figures 54 and 55, it is notable that dust layer concentration does not seem to considerably influence the explosion pressure. This could potentially be attributed to the relatively short length of the pipes, which results in limited flame acceleration.

Figure 54: Illustration of Configuration 1, consisting of a single 6-metre DN250 pipe.

Figure 55: Illustration of Configuration 2, consisting of a single 6-metre DN160 pipe.

The pressure data in figures 32, 33, 37 and 38 indicate that the primary explosion do not trigger significant exothermic activity within the pipes, as there is little variation with a dust layer and without one. On the contrary, figures 29, 30, 34 and 35, illustrating the fireball characteristics from the test series conducted in configuration 1 and 2, show a strong correlation between dust layer concentration and fireball length, as illustrated in Figure 56. This shows that most of the combustion happens outside the pipe.

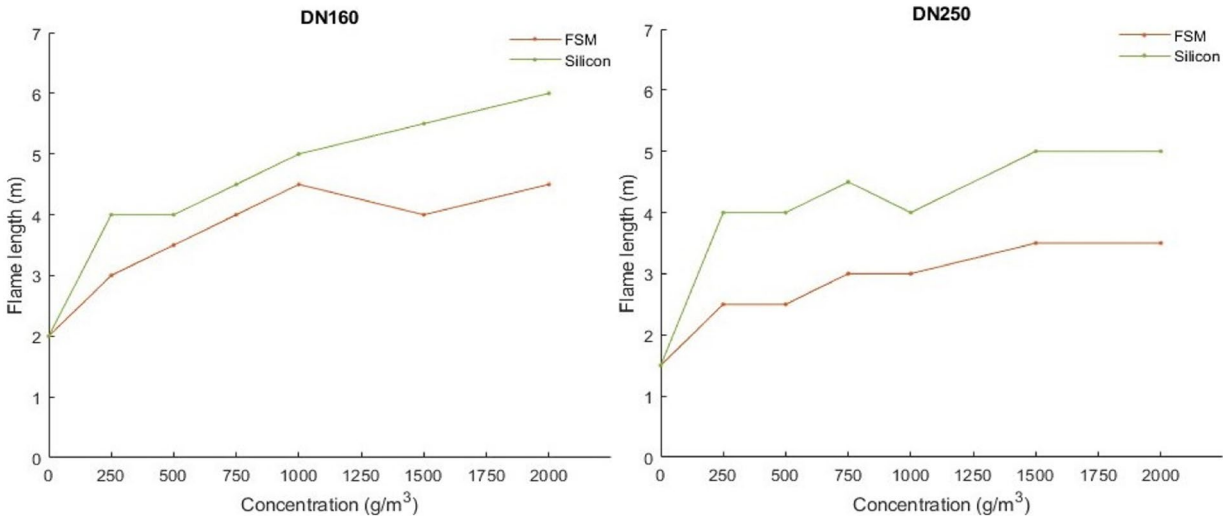

Figure 56: Fireball length for a given concentration in DN160 (left) and DN250 (right)

Interestingly, the maximum fireball length was observed in the configuration 2 for FSM and silicon. A plausible explanation for this phenomenon is the increased confinement in the ignition chamber when attached to the DN160 pipe, as compared to the DN250 pipe. This heightened confinement could intensify both the pressure and velocity of the pressure wave created by the expanding combustion products, amplifying turbulence within the DN160 pipe. This turbulence can subsequently facilitate more efficient dust lifting, resulting an increased transport of dust particles to the outside. It is probably also the reason for the second explosion event, that can be observed for silicon in the DN160 pipe.

Further tests are needed to establish for what pipe dimensions this holds true. The dynamics of flame propagation and the resulting explosion pressures are expected to vary significantly depending on the length of the pipe. In longer pipes, the flame would have more space and time to accelerate, and as a result, it may reach higher velocities. This increase in velocity could then lead to higher explosion pressures.

5.2.3 Configuration 3

In the experiments carried out in configuration 3, as depicted in Figure 57, flame propagation through both pipes was observed in only two scenarios when a dust layer was exclusively placed in the DN160 pipe. These specific instances involved either the absence of dust in the pipes or a concentration of 500 g/m^3 with silicon. As flame propagation occurred solely in the test without a dust layer and with the leanest concentration tested, it is plausible that higher concentrations could have induced flame cooling, thereby extinguishing the flame before it could propagate through both pipes. Alternatively, it might be that the flame, having to propagate first through the DN250 pipe before encountering the dust layer in the DN160 pipe, becomes almost depleted. In either case, this appears to be an edge case of what volume the primary explosion in the ignition chamber can propagate through, while both lifting and igniting a dust layer.

Figure 57: Illustration of configuration 3, which comprises a 6-metre DN250 pipe and a DN160 pipe.

The pressures illustrated in Figure 40 demonstrate minimal fluctuation in explosion pressure across different dust layer concentrations within the system. This remains true even when compared to scenarios with no dust layer in the DN250 pipe, wherein no substantial differences are noted. These findings suggest that, apart from the primary explosion, there is limited exothermic activity instigated within the system.

When a silicon dust layer was introduced into both the DN250 pipe and the DN160 pipe, the explosion pressure at 11-metre escalated dramatically, registering the highest reading observed in all tests involving configurations with one or two pipes. This heightened explosion pressure could likely be ascribed to the increased flow velocity caused by the crossover, transitioning the flow from a DN250 pipe to a DN160 pipe. This amplified flow velocity likely induced enhanced turbulence within the DN160 pipe, resulting in a rise in dust lifting. It is also probable that the crossover accelerated the flame, expanding the area of the flame front and facilitating faster combustion, thereby resulting in increased rate of and consequently increased pressure. The resultant fireball from this test was longer than that observed for the same concentration solely with the DN160 pipe, further indicating the effect of explosion pressure on fireball length.

5.2.4 Configuration 4

In the experiments in configuration 4, illustrated in Figure 58, with the inclusion of a dust layer solely in the DN250 pipe, a distinct elevation in explosion pressure was observed within the DN250 pipe relative to the tests in configuration 1. This observed increase is likely due to the crossover connection between the pipes, functioning as a diffuser. This observation aligns with the theoretical principles of diverging diffusers for subsonic speeds, where the flow velocity is reduced while the pressure correspondingly rises as the pipe diameter expands. An increase in pressure can be detected in both pipes approximately 20 milliseconds after ignition, likely a result of the combustion of the dust cloud that forms in the wake of the leading shock from the primary explosion in the ignition chamber.

Figure 58: Illustration of configuration 4, which comprises a 6-metre DN160 pipe and a DN250 pipe.

When a dust layer is introduced into both the DN160 pipe and the DN250 pipe, the explosion pressure in the DN250 pipe remains nearly identical to that observed without the additional dust layer. However, the dust layer appears to link the initial and secondary pressure rises that are observed in the absence of the dust layer, thereby resulting in an extended period of heightened pressure. As the deflagration traverses through the converging crossover that connects the two pipes, the pressure remains largely constant, contradicting the theoretical model of converging nozzles where pressure should decline. This may indicate an increase in exothermic activity. After the crossover, the pressure is markedly higher than that observed in tests with a dust layer only in the DN250 pipe, and the peak pressure is achieved more rapidly.

The experiments without a dust layer in the DN160 pipe demonstrated an extended fireball length relative to the tests conducted solely with the DN250 pipe. Furthermore, an increase in dust layer concentration corresponded to an enlargement of the fireball. This evidence further substantiates the interrelationship between dust layer concentration, flow velocity, pressure, and the length of the fireball.

5.2.5 Configuration 5

In this section, the results obtained from the tests in configuration 5 are discussed, the configuration is illustrated in Figure 59. The results show that removing the two 6-metre DN60 pipes led to a significant decrease in explosion pressure, not only when compared to the tests with the two DN60 pipes attached but also concerning the test in configuration 4.

Figure 59: Illustration of configuration 5, which comprises a 6-metre DN250 pipe, a DN160 pipe and a DN160/DN60 crossovers.

A notably lower explosion pressure was observed in comparison to configuration 4. This can likely be attributed to the expulsion of a dust cloud into the open atmosphere. Figure 44 demonstrates that the configuration with the crossover attached expels much more dust than without it.

The reduction in explosion pressure observed in this configuration, as opposed to the one with the two DN60 pipes connected, can likely be attributed to the pressure wave expelling a substantial amount of unburnt silicon dust from the system ahead of the flame, along with the reduced pre-compression. These factors likely resulted in minimal pre-compression and pre-heating of a much leaner dust cloud compared to the tests featuring the two connected pipes.

5.2.6 Configuration 6

In this section, the results obtained from the tests in configuration 6 are discussed, the configuration is illustrated in Figure 60.

Figure 60: Illustration of configuration 6, which comprises a 6-metre DN250 pipe, a DN160 pipe, and two DN60 pipes interconnected with crossovers.

Test #1 and #2 with Silicon

In the 25-metre configuration, using a concentration of 1000 g/m^3 of silicon dust, the explosion pressure and shock wave velocity observed from tests #1 and #2 align with values typically expected in the detonation regime.

Test #1 had oscillations in pressure readings, suggesting that a significant event occurred between the 11-metre and 15-metre transducers within the pipes. This inference is drawn from the sudden pressure increase and oscillating readings, first at the 11-metre transducer, then at the 15-metre transducer. Test #2 yielded similar results, with more pronounced oscillation at the 11-metre transducer and less oscillation at the 15-metre transducer compared to test #1. Furthermore, the 21-metre transducer in test #2 recorded significantly lower pressure than in test #1, implying that the significant event happened closer to the 11-metre transducer than in test #1.

It should be noted that there is considerable uncertainty regarding the shock wave speeds presented in this thesis. The estimated speeds are based on interpretations of shock wave arrival times and are therefore somewhat subjective.

While detonation cell size measurements for silicon dust are currently unavailable, cell size for aluminium dust has been reported as 0.4 metres by Zhang et al. (2001) and 0.495 metres by Liu et al. (2009). Considering the similar properties between aluminium and silicon dust, and the enhanced reactivity of aluminium, it can be inferred that the cell size of silicon would not be smaller than that of aluminium. This assumption leads to the conclusion that the critical tube diameter required to support a self-sustained detonation is not achieved past the DN160/DN60 crossover, as the inner diameter of the pipe is reduced from 157 mm to 62 mm.

Figures 47 and 48 display a distinctive pressure progression pattern at the 11-metre transducer during tests #1 and #2. This pattern begins with a gradual pressure increase, followed by a minor decline and then a rapid increase in pressure, saturating the transducer. This pattern closely resembles the two-stage deflagration-to-detonation transition (DDT) in aluminium dust, as described by Zhang et al. (2001) and Liu et al. (2009). The slow initial pressure increase matches their described pre-compression stage, and the sharp subsequent pressure spike aligns with their defined fast shock stage.

Assuming that the system behaves according to the properties of an ideal gas, and with the speed of sound equivalent to that in particle-free air, the speed of sound in the unburned dust/air mixture has previously in section 2.1.8 been calculated be 1140 $m \cdot s^{-1}$. This calculation

assumes that the surrounding medium maintains a temperature equivalent to the adiabatic flame temperature for silicon. In test #1, the downstream shock wave has an average speed of Mach 0.95, while the upstream shock wave has an average speed of Mach 1.38. In test #2, the initial average speeds for the downstream and upstream shock waves are recorded at Mach 1.78 and Mach 1.43, respectively. Interestingly, in both tests, the shock wave does not sustain the average speed in either direction. In test #1, the downstream shock wave appears to accelerate. By the time the wave reaches both the closed and open ends of the test rig, its average velocity aligns closely with the speed of sound. This behaviour of the upstream-facing shock wave resembles the retonation wave detailed by Sichel et al. (1995). Since the adiabatic flame temperature is used and the effect of dust particles is neglected, all Mach calculations are on the conservative side, the actual Mach number is likely to be higher. The fastest shock wave speed measured in test #2 was 2034 $m \cdot s^{-1}$, and are in reasonable agreement with the calculated Chapman-Jouguet velocity of 2100 $m \cdot s^{-1}$.

The primary explosion in the ignition chamber did not result in significant exothermic activity in the DN250 pipe in test #1 and #2, as evidenced by the low pressure. However, the upstream shock wave from the event initiated additional exothermic reactions in the DN250 pipe and the ignition chamber, increasing the pressure, the maximum pressure reading in the ignition chamber is likely caused by shock wave reflections and amplification.

Test #3, #4 and #5

In test #3, relatively low pressure was observed across all transducers, until a peak pressure of 5.1 barg was registered at the 12.5 metre transducer. This was followed by a peak pressure of 8.1 barg at 13.5 metres and 47.4 barg at 21 metres. The test shows no sign of a pressure wave speed indicating the formation of a shock wave. No pre-compression is observed before the peak pressure at 21 metres. Notably, oscillations starting at the 13.5 and 12.5 metre transducers occur exactly at the same time as the peak pressure at 21 metres. The maximum pressure reading at 21 metres is likely caused by either vibrations in the pipe caused by the explosion or by movement of the end of the pipe when the flame exits. This leads to the acceleration compensation in the transducer being triggered, resulting in a potentially false pressure reading.

In test #4, the pressure graphs have many similarities to test #1 and #2. The pressure graphs show clear signs of a slow pre-compression phase followed by a faster shock phase. The maximum average shock wave speed recorded was 1200 $m \cdot s^{-1}$ from the 13.5-metre transducer to the 21-metre transducer. The figure shows an abrupt increase in pressure at the 21-metre transducer with a peak pressure reading of 104 barg. However, no slow pre-compression is observed at this transducer, thus the high pressure reading is likely erroneous, possibly caused by vibrations in the pipe.

In test #5, when introducing a dust layer of 5000 g/m^3 to the system, the highest averaged pressure across multiple transducers was recorded. All sensors located in the area of the DN160/DN60 crossover exhibited high pressures, with a peak pressure reading of 66.4 barg at the 11.5 metre transducer. The pressure graphs show that the transducers at 10.5 and 11.5 metres registered two distinct pressure increases, where the last one was the most significant. The transducers at 12.5 and 13.5 metres exhibited only one distinct peak where the pressure was very high. The increased pressure wave speeds indicate the formation of a shock wave in the area of the crossover.

Despite the findings in the tests, the scarcity of data due to limited instrumentation in the experiments hampers the formulation of a definitive explanation for these findings. Nevertheless, the existing data provides valuable insights for the generation of hypotheses:

Hypothesis 1 – Pressure Piling

As the deflagration progresses through an arrangement of progressively constricting pipes, the unburned dust-air mixture within these pipes gets compressed ahead of the advancing flame. This phenomenon occurs because the pressure wave from the deflagration moves faster than the flame front. At the narrowest section, or the throat, of the DN160/DN60 crossover, the flow becomes choked due to the small cross-sectional area. Additionally, dust particles suspended in the air are forced through the crossover. While these particles are not dense enough to cause jamming, they do add an additional layer of obstruction. This obstruction leads to further pre-compression of the unburned mixture in the path of the flame.

As a result, when the flame front reaches the pre-compressed suspension, the ensuing combustion process occurs at a significantly higher pressure. This leads to an explosion with pressure levels far exceeding those anticipated from a deflagration. However, this hypothesis does not readily account for the shock wave patterns observed in the tests. The characteristics of the shock waves in these figures suggest additional dynamic phenomena that might not be adequately explained by pressure piling alone. Despite this, it should be considered that the perceived discrepancies could potentially be due to misinterpretation of shock wave arrival times, meaning what is currently identified as shock waves could, in fact, be pressure waves.

Hypothesis 2 – Deflagration to Detonation Transition

The expanding combustion products, propelled by the deflagration, flow through the concentric crossover between the DN250 and DN160 sections. Here, they undergo acceleration, yet the flow remains subsonic. As the flow enters the crossover from the DN160 to the DN60 section, it accelerates further, eventually reaching Mach 1, which results in a choked flow condition in the crossover. This choked flow condition leads to a pre-compression of the unburnt dust/air mixture due to increased back pressure.

When the flame arrives at the pre-compressed area, it is already a fast turbulent deflagration due to being accelerated through the converging sections. Given the high initial pressure and flame velocity, the deflagration attempts to transition into a detonation but fails due to the small diameter of the pipe where the initiation occurs. The DDT initiation results in the formation of a shock that propagates in both directions, yielding high pressure readings. The velocity of most of the shock waves are approximately 50% of the calculated Chapman-Jouguet velocity of 2100 $m \cdot s^{-1}$, potentially indicating conditions akin to quasi-detonation or a fast turbulent deflagration, and the fastest shock waves approximate the calculated C-J velocity, indicating detonation.

Summary

These two hypotheses – pressure piling and deflagration to detonation transition - offer compelling, yet distinct explanations for the phenomena observed in the experiments involving silicon dust subjected to deflagration in increasingly confined environments. While each presents its own merits and limitations, they collectively underline the complex dynamics at play. Definitive conclusions are currently hampered by limited data and the absence of

measurements such as detonation cell size and flame arrival times. Despite these constraints, these hypotheses open avenues for further investigation. Furthermore, it should be noted that without precise flame arrival times, it is challenging to definitively interpret what pressure values are due to measurement errors or actual pressure phenomena. Despite the limitations in instrumentation, the agreement between the calculated Chapman-Jouguet velocity and the observed shock wave velocity suggests a deflagration to detonation transition.

Test with FSM

The FSM tests yielded significantly lower explosion pressures than silicon. This difference in explosion pressure can be attributed to the varying reactivity of the two substances and their distinct combustion mechanisms. With its high iron content, FSM likely to exhibit a higher degree of heterogeneous combustion due to the iron's influence on the reaction process.

To better understand the effects of particle size and chemical composition on combustion behaviour in the experimental set-up, it is necessary to conduct additional tests. Ideally, tests with FSM dust with a similar particle size to that of the silicon dust tested and tests using FSM dust with a lower iron and higher magnesium percentage could provide valuable insights. Furthermore, by adjusting the composition of FSM and controlling particle size, it may be possible to identify the threshold at which combustion behaviour changes and potentially observe a phenomenon similar to that observed with silicon dust.

5.2.7 Limitations

The results from the experiments conducted within the pipe(s), possess certain limitations and potential sources of error. These factors may exert an influence on the accuracy and reliability of the results, thus necessitating careful interpretation and further validation:

- *Variability in dust layer distribution*: The dust layer is distributed within the pipes using a 6-metre angle iron. The uniformity of the dust layer can only be visually inspected from the ends of the pipes, leaving parts of the dust layer unchecked. The width of the dust layer can affect the results, as shown by Sichel et al. (1995).
- *Cleaning challenges*: Due to the 6-metre length of the pipes, there are limited abilities to inspect them for remaining dust deposits between each test. This limitation results in uncertainty regarding the cleaning, potentially affecting the reliability and comparability of the experimental results.

- *Limited number of tests:* The study aimed to investigate as many pipe configurations and dust layer concentrations as possible within a limited timeframe. While four repetitions were conducted for silicon dust in configuration 6, other tests were not replicated. This discrepancy introduces uncertainty as dust explosions are highly sensitive to variations in test conditions.
- *Insufficient Instrumentation:* To thoroughly investigate the phenomena observed in configuration 6, obtaining pressure readings from the crossovers and every 1-2 metres within the pipes would have been ideal. Additionally, incorporating reliable optical flame sensors for flame arrival times and using the soot foil technique for measuring silicon detonation cell size would enhance the comprehension of observed phenomena. As it stands, the current results highlight the limitations of the instrumentation used in this study, which may potentially impact the comprehensiveness and accuracy of the findings.
- *Pressure transducer vibration*: The observed pressure and oscillations might be attributed to vibrations in the pipes, which could trigger the acceleration compensation in the transducers. To reduce uncertainties in future tests, vibration dampeners for the transducers and the pipes should be incorporated.
- *Weather Conditions*: All tests were conducted outdoors during winter and spring, resulting in variable weather conditions. These variations, ranging from sunny to snowy, introduce uncertainty regarding the pipes' humidity levels and the potential moisture impact on the dust layer. Although metal dusts are less affected by moisture compared to organic dusts, moisture can still increase surface tension, affecting dust dispersion. Furthermore, wind can easily disperse dust particles, potentially impacting the uniformity of the dust layer inside the pipes. This was mitigated by covering the pipe ends with a plastic bag after dust introduction, removed prior to test initiation.

6 Conclusion

The explosion characteristics of silicon and ferrosilicon magnesium dust have been studied utilizing a 20-litre apparatus, with results consistent with previous studies on similar types of dust. Experiments with the same dusts in pipes showed a strong correlation between dust layer concentration and the resultant fireball in both individual pipe and dual-pipe configurations. These findings also indicated that the explosion pressure is not coupled to dust layer concentration. This may change with modifications in pipe lengths and diameters or with the implementation of weaker or stronger ignition sources.

In the 25-metre configuration, encompassing pipes of three distinct diameters, it was revealed that explosions with a silicon dust with a K_{St} value of 194 ± 12% (which is on the border between St-1 and St-2 classification), possesses sufficient reactivity to cause detonation-like pressure and shock wave speeds. However, it remains to be determined if under different circumstances the deflagration of silicon dust can transition into a self-sustained detonation. Further research is needed to explore this phenomenon.

7 Further Work

The findings from this study opens numerous avenues for further exploration to enhance the understanding of flame propagation in dust extraction systems. In future work, it would be highly interesting to examine the following aspects in more detail:

- *Larger and/or longer systems:* Investigating how the phenomena observed in configuration 6 would change in larger or longer pipe systems. This could provide valuable insights into real-world applications and safety considerations. It would be interesting to determine whether the phenomena can occur for larger-diameter pipes with the same percentile reduction in diameter.
- *Improved instrumentation:* Enhancing the experimental setup with a reliable method for flame arrival times, like optic flame sensors, could offer a more precise understanding of the phenomena observed in the final tests. The system should also be equipped with more pressure transducers, ideally one per metre, and transducers in each concentric crossover.
- *Improved clamping:* To avoid vibrations and movement in the set-up during tests, the test rig should be fastened to concrete blocks using suitable clamps. The clamps should also be lined with rubber, to prevent vibrations in the pipes.
- *Reference tests*: Conducting reference tests using gaseous or hybrid mixtures would make it possible to isolate specific factors, such as dust dispersion.
- *Primary explosion:* Changing the ignition source from a dust cloud to a gas explosion in the ignition chamber could eliminate the variability of dust cloud dispersion, resulting in a higher degree of repeatability. All experimental tests in this thesis used the same dust concentration of 750 g/m^3 in the ignition chamber, further tests should look into the effect of varying the strength of the primary explosion.
- *Minimum dust layer concentration:* It would be highly interesting to investigate what dust concentrations is necessary to sustain a deflagration through longer pipes.
- *Ignition chamber volume:* Investigate how the volume of the vessel containing the primary explosion impacts flame propagation in the pipes.
- *Venting:* Explore the effect of different pressure relief configurations. This could help identify the boundary conditions for the phenomenon observed in this thesis.
- *Other dust types:* Investigate whether detonations can be observed for other types of dust in the same experimental set-up.

- *Sampling of accumulated dust:* Conduct sampling and explosion testing of accumulated dust in process plants to assess inventory and reactivity, thus furthering our understanding of the associated hazards.
- *Computational Fluid Dynamics (CFD):* To gain a more comprehensive understanding of the fluid behaviour within the system, particularly around the complex regions like crossovers, it would be highly beneficial to perform a computational fluid dynamics analysis. FLACS, a CFD tool, features a dust model known as DustEX. Currently, this model does not support simulations involving metal dust. However, this functionality is under development.

References

Allen, T. (2003). *Powder Sampling and Particle Size Determination*. Elsevier.

Atkins, P., Paula, J. d., & Keeler, J. (2018). *Atkins' Physical Chemistry* (Eleventh ed.). Oxford University Press.

Bartknecht, W. (1989). *Dust Explosions Course, Prevention, Protection* (1 ed.). Springer Berlin Heidelberg.

Ben-Dor, G. (2001). Two Dimensional Reflection. In G. I. Ben-Dor, Ozer. & T. Elperin (Eds.), *Handbook of Shock Waves* (Vol. 2, pp. 68-202). Academic Press.

Ben-Dor, G. (2006). A State-of-the-Knowledge Review on Pseudo-Steady Shock-Wave Reflections and their Transition Criteria. *Shock Waves*, *15*(3), 277-294.

Bjørnsen, A. (2023). *Experimental Investigation of Silicon Dust Explosions in Pipes* [University of Bergen]. Bergen Open Research Archive.

Broggi, A. (2021). *Condensation of SiO and CO in Silicon and Ferrosilicon Production* [Norwegian University of Science and Technology].

Broggi, A., Tangstad, M., & Ringdalen, E. (2019). Characterization of a Si-SiO 2 Mixture Generated from SiO(g) and CO(g). *Metallurgical and Materials Transactions B*, *50*, 2667-2681.

Casal, J. (2018). *Evaluation of the Effects and Consequences of Major Accidents in Industrial Plants* (Second ed.). Elsevier.

Cashdollar, K. L., & Zlochower, I. A. (2007). Explosion temperatures and pressures of metals and other elemental dust clouds. *Journal of Loss Prevention in the Process Industries*, *20*, 337–348.

Cesana, C., & Siwek, R. (2020). Manual for 20-l-Apparatus 7.1. In: TÜV SÜD Schweiz AG, Cesana AG.

Cross, M., & Ciccarelli, G. (2015). DDT and Detonation Propagation Limits in an Obsatcle Filled Tube. *Journal of Loss Prevention in the Process Industries*, *36*, 380-386.

Crowe, C. T., Schwarzkopf, J. D., Sommerfeld, M., & Tsuji, Y. (2011). *Multiphase Flows with Droplets and Particles* (2 ed.). CRC Press.

Eckhoff, R. K. (2003). *Dust explosions in the process industries* (Third ed.). Elsevier.

Eckhoff, R. K. (2016). *Explosion hazards in the process industries* (Second ed.). Elsevier.

Eckhoff, R. K., & Li, G. (2021). Industrial Dust Explosions. A Brief Review. *Applied Sciences*, *11*(4).

El-Sayed, A. F. (2016). *Fundamentals of Aircraft and Rocket Propulsion* (1 ed.). Springer.

Emanuel, G. (2001). Shock Waves in Gases. In G. Ben-Dor, O. Igra, & T. Elperin (Eds.), *Handbook of Shock Waves* (Vol. 1, pp. 185-262). Academic Press.

Friedman, M. P. (1960). An Improved Perturbation Theory for Shock Waves Propagating Through Non-Uniform Regions. *Journal of Fluid Mechanics*, *8*(2), 193-209.

Futko, S. i., Koznacheev , I. A., Rabinovich , O. S., Penyazkov, O. G., & Krivosheyev, P. N. (2019). On the Mechanism of Combustion of Thin Nanostructurized Silicon Plates in Oxygen at an Elevated Pressure. *Journal of Engineering Physics and Thermophysics*, *92*(1).

Gan, B., Yang, M., Zhang, S., Zhou, Y., Bi, M., & Wei, G. (2019). Flame propagation and pressure characteristics of polymethyl methacrylate dust explosions in a horizontal pipe. *Journal of Loss Prevention in the Process Industries*, *62*.

Gelfand, B. E., Silnikov, M. V., Medvedev, S. P., & V., K. S. (2012). *Thermo-Gas Dynimics of Hydrogen Combustion and Explosion*. Springer.

Glassman, I., & Yetter, R. A. (2008). *Combustion* (4 ed.). Academic Press.

Guo, Y., Ren, K., Wei, A., Tao, C., Huang, W., Zhao, P., & Wi, D. (2022). Iron dust explosion characteristics with small amount of nano-sized Fe 2 O 3 and Fe 3 O 4 particles. *Fuel*, *324*.

Holbrow, P., Hawksworth, S. J., & Tyldesley, A. (2000). Thermal Radiation from Vented Dust Explosions. *Journal of Loss Prevention in the Process Industries*, *13*(6), 467-476.

Igra, O., & Heilig, W. (2001). Shock Waves in Channels. In G. Ben-Dor, O. Igra, & T. Elperin (Eds.), *Handbook of Shock Waves* (Vol. 2, pp. 320-392). Academic Press.

Kauffman, C. W. (1982). Agricultural Dust Explosions in Grain Handling Facilities. Fuel-air Explosions, Ontario, Canada.

Kittel, C. (2005). *Introduction to Solid State Physics* (Eighth ed.). John Wiley & Sons, Inc.
Kletz, T. A., & Amyotte, P. (2010). *Process Plants: A Handbook for Inherently Safer Design* (2 ed.). CRC Press.
Krehl, P. (1992). Single-Mach and double-Mach reflection — its representation in Ernst Mach's historical soot method. *Shock Waves*(Proceedings of the 18th International Symposium on Shock Wave), 221-226.
Krehl, P. (2001). History of Shock Waves. In G. Ben-Dor, O. Igra, & T. Elperin (Eds.), *Handbook of Shock Waves* (Vol. 1, pp. 1 - 142). Academic Press.
Lee, J. H. S. (2008). *The Detonation Phenomenon*. Cambridge University Press
Li, G., Yang, H.-X., Yuan, C.-M., & Eckhoff, R. K. (2016). A catastrophic aluminium-alloy dust explosion in China. *Journal of Loss Prevention in the Process Industries*, *39*, 121-130.
Li, J., He, J., Meng, B., & Tian, B. (2022). Investigation of dust lifting by a moving shock wave based on compressible multiphase particle-in-cell method *Physics of Fluids*, *34*(10).
Lide, D. R. (2006). CRC Handbook of Chemistry and Physics. In (86th ed., pp. Standard Thermodynamic Properties of Chemical Substances): Taylor and Francis.
Liu, Q., Li, X., & Bai, C. (2009). Deflagration to detonation transition in aluminum dust–air mixture under weak ignition condition. *Combustion and Flame*, *156*(4), 914-921.
Malvern Panalytical (2013). MASTERSIZER 3000 USER MANUAL. In.
Milton, B. E. (2001). Axisymmetric Shock Wave Reflection. In G. Ben-Dor, O. Igra, & T. Elperin (Eds.), *Handbook of Shock Waves* (Vol. 2, pp. 266-317). Academic press.
Nessvi, K., & Persson, H. (2019). *Dammexplosionsrisker i metallbearbetande industri*.
Ogle, R. A. (2016). *Dust Explosion Dynamics* (1 ed.). Butterworth-Heinemann.
Pitard, F. F. (1993). *Pierre Gy's Sampling Theory and Sampling Practice. Heterogeneity, Sampling Correctness, and Statistical Process Control* (2 ed.). CRC Press.
Rudinger, G. (1980). Fundamentals of Gas-Particle Flow. In J. C. Williams & T. Allen (Eds.), *Handbook of Powder Technology* (Vol. 2, pp. 142). Elsevier Scientific Publishing Company.
Schei, A., Tuset, J. K., & Tveit, H. (1998). *Production of High Silicon Alloys*. Tapir Academic Press.
Shepherd, J. E. (2023). *Shock and Detonation Toolbox - 2021 Version*.
Sichel, M., Kauffman, C. W., & Li, Y. C. (1995). Transition from Deflagration to Detonation in Layered Dust Explosions. *Process Safety Progress*, *14*(4), 257-265.
Skjold, T. (2003). *Selected Aspects of Turbulence and Combustion in 20-Litre Explosion Vessels* [University of Bergen]. Bergen Open Research Archive.
Skjold, T., Castellanos, D., Olsen, K. L., & Eckhoff, R. K. (2014). Experimental and numerical investigation of constant volume dust and gas explosions in a 3.6-m flame acceleration tube. *Journal of Loss Prevention in the Process Industries*, *30*, 164-176.
Smithells Metals Reference Book. (1998). (E. A. Brandes & G. B. Brook, Eds. 7 ed.). Butterworth-Heinemann.
Sun, H., Xu, S., Pan, X., Shi, L., Geng, X., & Cai, Y. (2019). Investigating the jamming of particles in a three-dimensional fluid-driven flow via coupled CFD–DEM simulations. *International Journal of Multiphase Flow*, *114*, 140-153.
Suna, X., Yanc, C., Yand, Y., Mid, X., Lee, J. H. S., & Ng, H. D. (2022). Critical Tube Diameter for Quasi-Detonations. *Combustion and Flame*, *244*.
Teodorczyk, A., Lee, J. H. S., & Knystautas, R. (1989). Propagation Mechanism of Quasi-Detonations. *Symposium on Combustion*, *22*(1), 1723-1731.
Wikipedia. (2022). *Jamming (Physics)*. Wikipedia. Retrieved 26.05.2023 from https://en.wikipedia.org/wiki/Jamming_(physics)
Wolinski, M., & Wolanski, P. (1992). Shock-Wave Induced Combustion of Dust Layers.
Young, H. D., & Freedman, R. A. (2016). *Sears & Zemansky's University Physics with Modern Physics* (14 ed.). Pearson.
Zhang, F., Gröning, H., & van de Ven, A. (2001). DDT and detonation waves in dust-air mixtures. *Shock Waves*, *11*, 53-71.

Østgård, T. (2022). *En eksperimentell studie av partikkelstørrelsesfordelingens innvirkning på utvalgte eksplosjonsparametere for silisiumstøv* [University of Bergen]. Bergen Open Research Archive.

Appendix A: KSEP Reports

Silgrain MC P_{max}

Universitetet i Bergen - Dust lab

Sample:	**Silgrain MC**
Customer:	
Reason:	
Data to sample origin:	
Preparation of sample:	
Median value:	

Explosion Characteristics

Max. explosion pressure:	Pmax	=	**9,5** bar	± 10%
Max. rate of pressure rise:	(dP/dt)max	=	**716** bar / s	± 12%
Product specific constant:	Kmax	=	**194** m·bar / s	± 12%

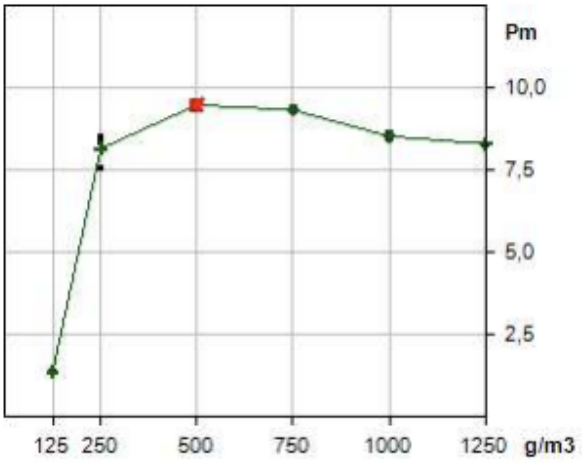

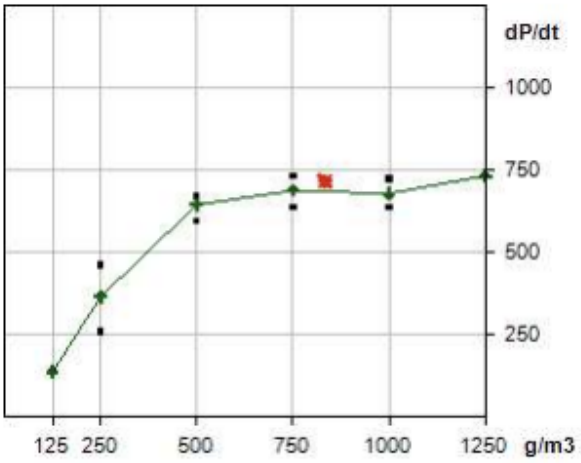

Dust: Pmax, Kmax **Silgrain MC**

Test	Series	Conc. [g/m3]	Pm [bar]	dP/dt [bar/s]	tv eff [ms]
1	1	125	1,4	136	60
2	1	250	7,6	260	60
3	1	500	**9,5**	665	60
4	1	750	9,4	**733**	59
5	1	1000	8,6	674	60
6	1	1250	8,3	732	60
7	-	250	,0	0	60
8	-	500	,0	188?	60
9	2	250	8,4	461	60
10	2	500	**9,6**	673	60
11	2	750	9,3	637	60
12	-	1000	8,7	887	60
13	2	1000	8,5	**724**	61
14	3	250	8,5	370	61
15	3	500	**9,4**	594	60
16	3	750	9,3	**691**	60
17	3	1000	8,4	636	60

Silgrain MC LEL

Universitetet i Bergen - Dust lab

Sample: **Silgrain MC**
Customer:
Reason:
Data to sample origin:
Preparation of sample:
Median value:

Explosion Characteristics

Lower explosion limit: LEL = **100** g/m3 ± 10%

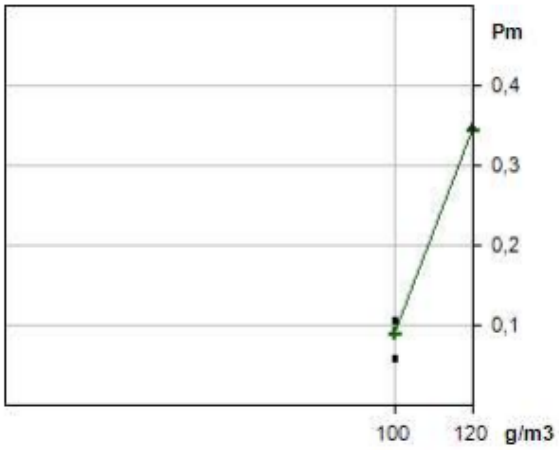

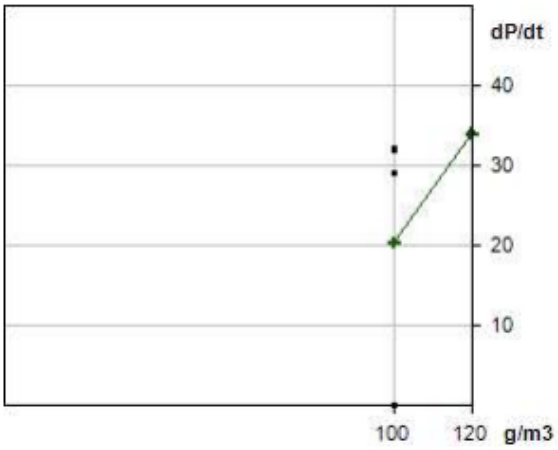

Dust: LEL **Silgrain MC**

Test	Series	Conc. [g/m3]	Pm [bar]	dP/dt [bar/s]	tv eff [ms]
1	1	100	,1	32	59
2	1	100	,1	29?	60
3	1	100	,1	0	60
4	1	120	**,3**	**34**	60

FSM P_{max}

Universitetet i Bergen - Dust lab

Sample: **FSM**
Customer:
Reason:
Data to sample origin:
Preparation of sample:
Median value:

Explosion Characteristics

Max. explosion pressure:	Pmax	=	**7,4**	bar	± 10%
Max. rate of pressure rise:	(dP/dt)max	=	**473**	bar / s	± 12%
Product specific constant:	Kmax	=	**128**	m·bar / s	± 12%

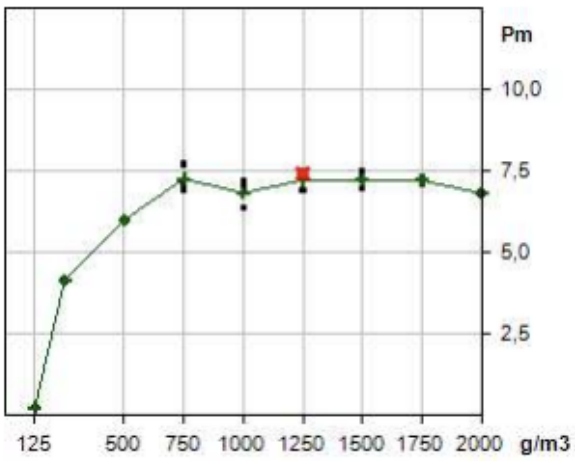

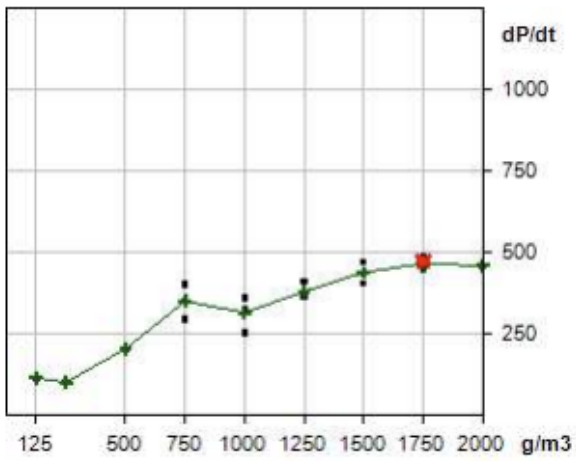

Dust: Pmax, Kmax **FSM**

Test	Series	Conc. [g/m3]	Pm [bar]	dP/dt [bar/s]	tv eff [ms]
1	1	125	,2	114	60
2	1	250	4,1	101	60
3	1	500	6,0	204	60
4	1	750	6,9	295	60
5	1	1000	6,9	329	60
6	1	1250	6,9	364	60
7	1	1500	7,0	406	60
8	1	1750	**7,1**	446	60
9	1	2000	6,8	**459**	60
10	2	750	**7,7**	401	60
11	2	1000	7,2	360	61
12	2	1250	7,3	362	60
13	2	1500	7,5	**472**	60
14	2	1750	7,3	463	60
15	3	750	7,1	353	60
16	3	1000	6,4	254	60
17	3	1250	**7,4**	412	60
18	3	1500	7,2	435	60
19	3	1750	7,2	**488**	60

FSM LEL

Universitetet i Bergen - Dust lab

Sample: **FSM**
Customer:
Reason:
Data to sample origin:
Preparation of sample:
Median value:

Explosion Characteristics

Lower explosion limit: LEL = **100** g/m3 ± 10%

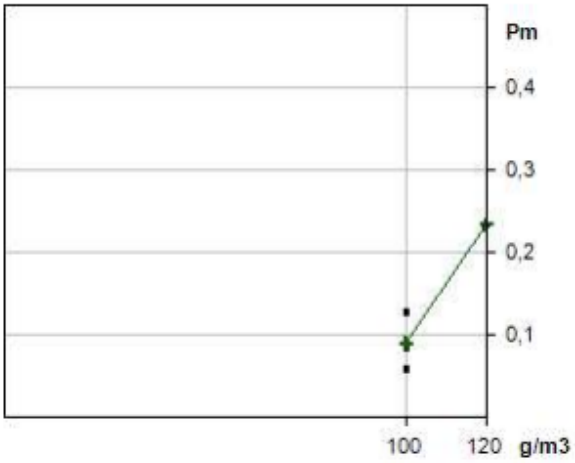

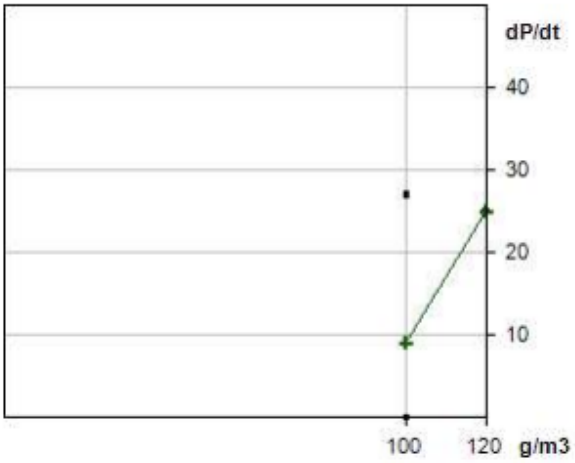

Dust: LEL **FSM**

Test	Series	Conc. [g/m3]	Pm [bar]	dP/dt [bar/s]	tv eff [ms]
1	1	120	**,2**	25	60
2	1	100	,1	0	60
3	1	100	,1	0	60
4	1	100	,1	**27**	60

Appendix B: Malvern Analysis

Malvern Analysis Silgrain MC

Analysis

Elkem AS Technology

Malvern

Measurement Details	
Operator Name	krscni
Sample Name	Average of ' Lot BREJ-1606057912'
SOP File Name	AeroS.cfg

Measurement Details	
Analysis Date Time	08.02.2023 10:48:09
Measurement Date Time	08.02.2023 10:48:09
Result Source	Averaged

Analysis	
Particle Name	Si krystallinsk
Particle Refractive Index	0.000
Particle Absorption Index	0.000
Dispersant Name	Dry dispersion
Dispersant Refractive Index	1.000
Scattering Model	Fraunhofer
Analysis Model	Narrow Modes
Weighted Residual	0.78 %
Laser Obscuration	2.79 %

Result	
Concentration	0.0007 %
Span	1.566
Uniformity	0.499
Specific Surface Area	1479 m^2/kg
D [3;2]	1.74 µm
D [4;3]	2.81 µm
Dv (10)	0.756 µm
Dv (50)	2.65 µm
Dv (90)	4.91 µm
Dv (99)	7.65 µm
Dv (99.9)	10.5 µm
Dv (100)	11.2 µm
Dv (95)	5.50 µm

Frequency (compatible)

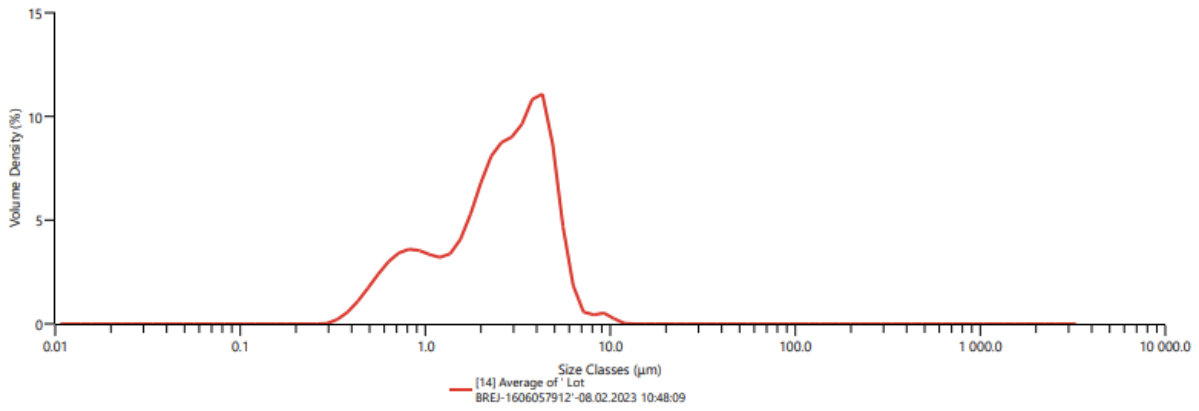

Result

Size (µm)	% Volume In	Size (µm)	% Volume In	Size (µm)	% Volume In	Size (µm)	% Volume In	Size (µm)	% Volume In	Size (µm)	% Volume In	Size (µm)	% Volume In	Size (µm)	% Volume In	Size (µm)	% Volume Ir
0.0100	0.00	0.0463	0.00	0.214	0.00	0.991	2.78	4.58	7.33	21.2	0.00	98.1	0.00	454	0.00	2100	0.0
0.0114	0.00	0.0526	0.00	0.243	0.00	1.13	2.65	5.21	3.82	24.1	0.00	111	0.00	516	0.00	2390	0.0
0.0129	0.00	0.0597	0.00	0.276	0.00	1.28	2.78	5.92	1.42	27.4	0.00	127	0.00	586	0.00	2710	0.0
0.0147	0.00	0.0679	0.00	0.314	0.16	1.45	3.35	6.72	0.39	31.1	0.00	144	0.00	666	0.00	3080	0.0
0.0167	0.00	0.0771	0.00	0.357	0.46	1.65	4.40	7.64	0.35	35.3	0.00	163	0.00	756	0.00	3500	
0.0189	0.00	0.0876	0.00	0.405	0.90	1.88	5.69	8.68	0.46	40.1	0.00	186	0.00	859	0.00		
0.0215	0.00	0.0995	0.00	0.460	1.44	2.13	6.78	9.86	0.19	45.6	0.00	211	0.00	976	0.00		
0.0244	0.00	0.113	0.00	0.523	2.01	2.42	7.32	11.2	0.00	51.8	0.00	240	0.00	1110	0.00		
0.0278	0.00	0.128	0.00	0.594	2.51	2.75	7.48	12.7	0.00	58.9	0.00	272	0.00	1260	0.00		
0.0315	0.00	0.146	0.00	0.675	2.87	3.12	7.97	14.5	0.00	66.9	0.00	310	0.00	1430	0.00		
0.0358	0.00	0.166	0.00	0.767	3.01	3.55	9.08	16.4	0.00	76.0	0.00	352	0.00	1630	0.00		
0.0407	0.00	0.188	0.00	0.872	2.96	4.03	9.44	18.7	0.00	86.4	0.00	400	0.00	1850	0.00		

Malvern Analysis FSM

Analysis

Elkem AS Technology

Malvern

Measurement Details	
Operator Name	krscni
Sample Name	Average of 'FSM 1'
SOP File Name	AeroS.cfg

Measurement Details	
Analysis Date Time	07.02.2023 16:46:12
Measurement Date Time	07.02.2023 16:46:12
Result Source	Averaged

Analysis	
Particle Name	FeSiMg
Particle Refractive Index	0.000
Particle Absorption Index	0.000
Dispersant Name	Dry dispersion
Dispersant Refractive Index	1.000
Scattering Model	Fraunhofer
Analysis Model	Narrow Modes
Weighted Residual	1.39 %
Laser Obscuration	2.28 %

Result	
Concentration	0.0016 %
Span	2.240
Uniformity	0.731
Specific Surface Area	1167 m^2/kg
D [3;2]	5.14 µm
D [4;3]	12.1 µm
Dv (10)	2.38 µm
Dv (50)	9.71 µm
Dv (90)	24.1 µm
Dv (99)	38.9 µm
Dv (99.9)	44.1 µm
Dv (100)	45.5 µm
Dv (95)	32.7 µm

Frequency (compatible)

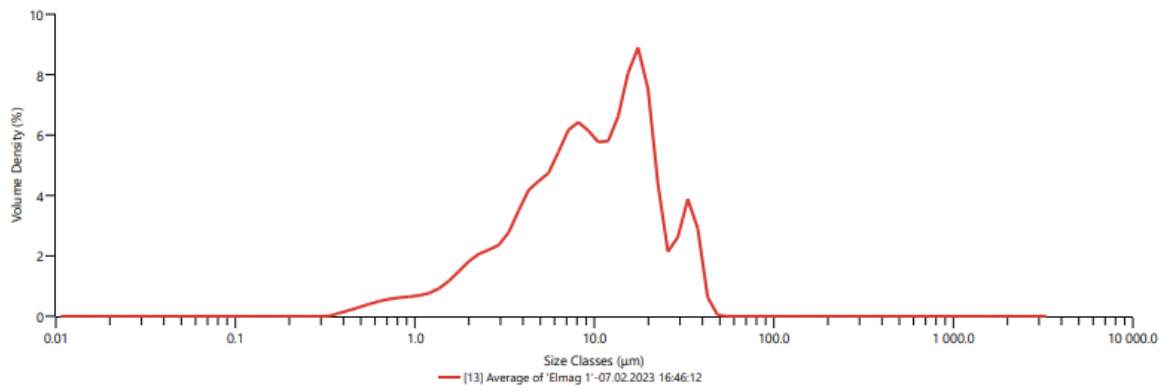

Result

Size (µm)	% Volume In	Size (µm)	% Volume In	Size (µm)	% Volume In	Size (µm)	% Volume In	Size (µm)	% Volume In	Size (µm)	% Volume In	Size (µm)	% Volume In	Size (µm)	% Volume In
0.0100	0.00	0.0463	0.00	0.214	0.00	0.991	0.57	4.58	3.73	21.2	3.59	98.1	0.00	454	0.00	2100	0.00
0.0114	0.00	0.0526	0.00	0.243	0.00	1.13	0.63	5.21	3.92	24.1	1.57	111	0.00	516	0.00	2390	0.00
0.0129	0.00	0.0597	0.00	0.276	0.00	1.28	0.76	5.92	4.53	27.4	2.12	127	0.00	586	0.00	2710	0.00
0.0147	0.00	0.0679	0.00	0.314	0.00	1.45	0.97	6.72	5.18	31.1	3.41	144	0.00	666	0.00	3080	0.00
0.0167	0.00	0.0771	0.00	0.357	0.09	1.65	1.24	7.64	5.40	35.3	2.54	163	0.00	756	0.00	3500	
0.0189	0.00	0.0876	0.00	0.405	0.16	1.88	1.52	8.68	5.14	40.1	0.38	186	0.00	859	0.00		
0.0215	0.00	0.0995	0.00	0.460	0.25	2.13	1.73	9.86	4.78	45.6	0.00	211	0.00	976	0.00		
0.0244	0.00	0.113	0.00	0.523	0.34	2.42	1.83	11.2	4.78	51.8	0.00	240	0.00	1110	0.00		
0.0278	0.00	0.128	0.00	0.594	0.42	2.75	1.95	12.7	5.46	58.9	0.00	272	0.00	1260	0.00		
0.0315	0.00	0.146	0.00	0.675	0.48	3.12	2.29	14.5	6.76	66.9	0.00	310	0.00	1430	0.00		
0.0358	0.00	0.166	0.00	0.767	0.52	3.55	2.92	16.4	7.58	76.0	0.00	352	0.00	1630	0.00		
0.0407	0.00	0.188	0.00	0.872	0.54	4.03	3.51	18.7	6.42	86.4	0.00	400	0.00	1850	0.00		

Appendix C: Finite Element Analysis of Ignition Chamber

Analyzed File:	Ignition Chamber.iam
Autodesk Inventor Version:	2023 (Build 270158000, 158)
Creation Date:	02.09.2022, 15:51
Study Author:	Andreas Faye
Summary:	

Static Analysis:1

General objective and settings:

Design Objective	Single Point
Study Type	Static Analysis
Last Modification Date	02.09.2022, 15:34
Model State	[Primary]
Design View	Default
Positional	[Primary]
Detect and Eliminate Rigid Body Modes	Yes
Separate Stresses Across Contact Surfaces	No
Motion Loads Analysis	No

iProperties

Summary

Author	Andreas Faye

Project

Part Number	Tennkammer med tennerholder
Designer	Andreas Faye

Physical

Mass	125,316 kg
Area	2045660 mm^2
Volume	31927800 mm^3
Center of Gravity	x=290,216 mm y=317,125 mm z=392,869 mm

Note: Physical values could be different from Physical values used by FEA reported below.

Mesh settings:

Avg. Element Size (fraction of model diameter)	0,1
Min. Element Size (fraction of avg. size)	0,2
Grading Factor	1,5
Max. Turn Angle	60 deg
Create Curved Mesh Elements	No
Use part based measure for Assembly mesh	Yes

Material(s)

Name	Steel, Carbon	
General	Mass Density	7,85 g/cm^3
	Yield Strength	350 MPa
Stress	Ultimate Tensile Strength	420 MPa
	Young's Modulus	200 GPa
	Poisson's Ratio	0,29 ul
	Shear Modulus	77,5194 GPa
Part Name(s)	Endelokk ferdig.ipt dn355.ipt DN250.ipt Overgang 355 til 273.ipt	

Operating conditions

Pressure:1

Load Type	Pressure
Magnitude	10,000 MPa

Selected Face(s)

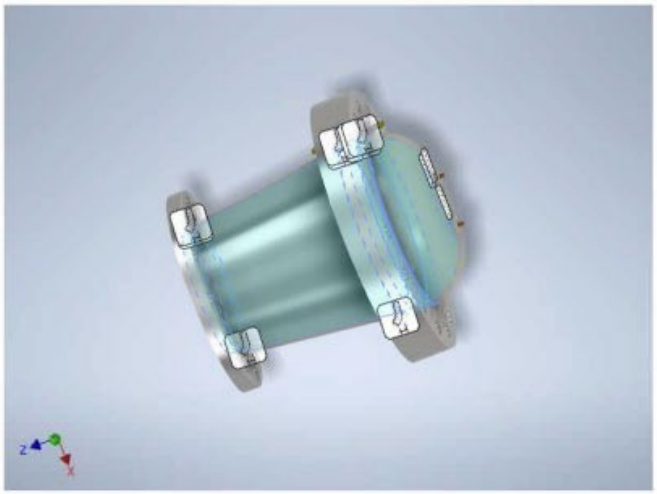

Fixed Constraint:1

Constraint Type	Fixed Constraint

Selected Face(s)

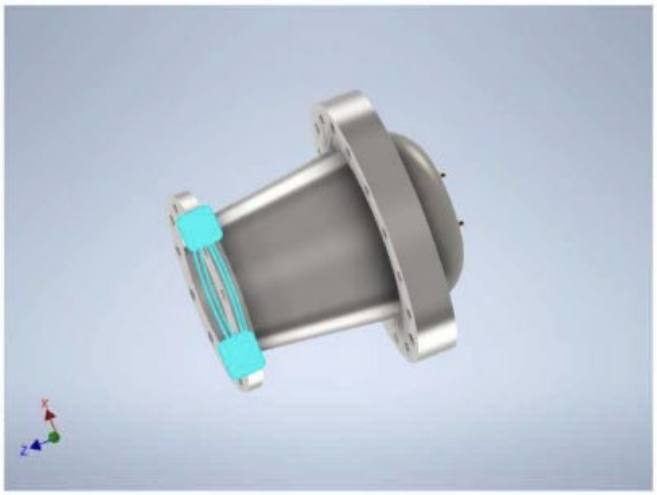

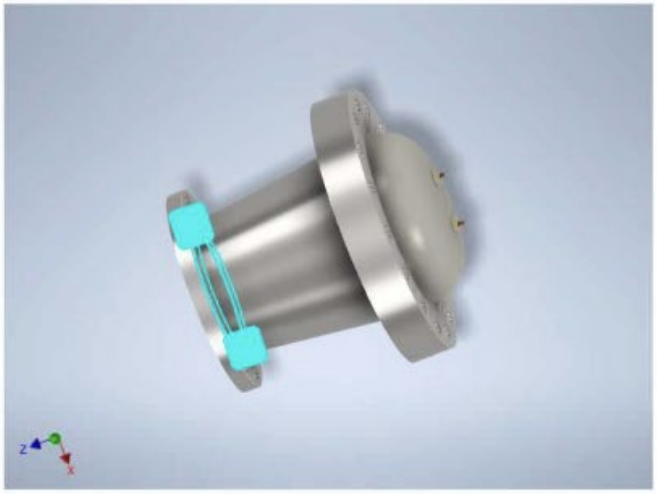

Fixed Constraint:2

Constraint Type	Fixed Constraint

Selected Face(s)

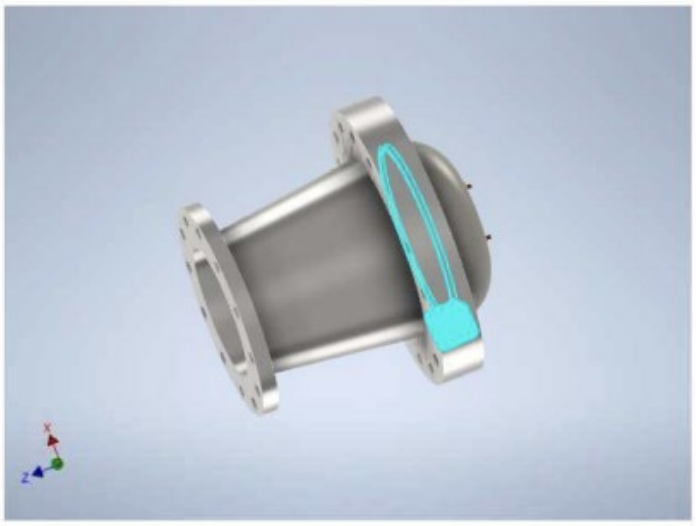

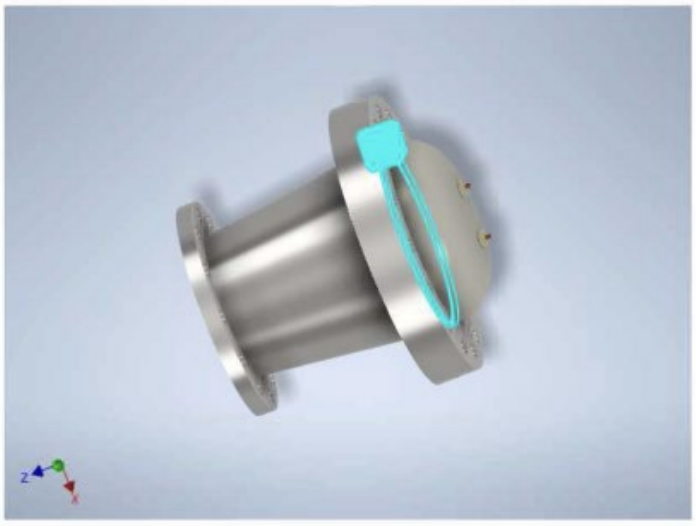

Fixed Constraint:3

Constraint Type	Fixed Constraint

Selected Face(s)

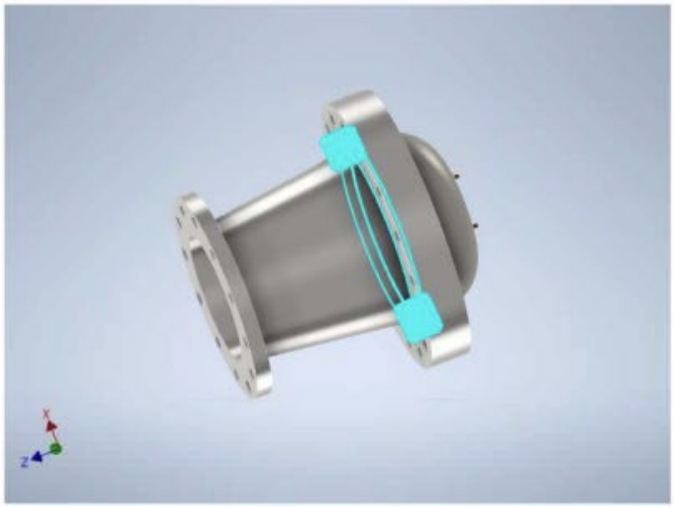

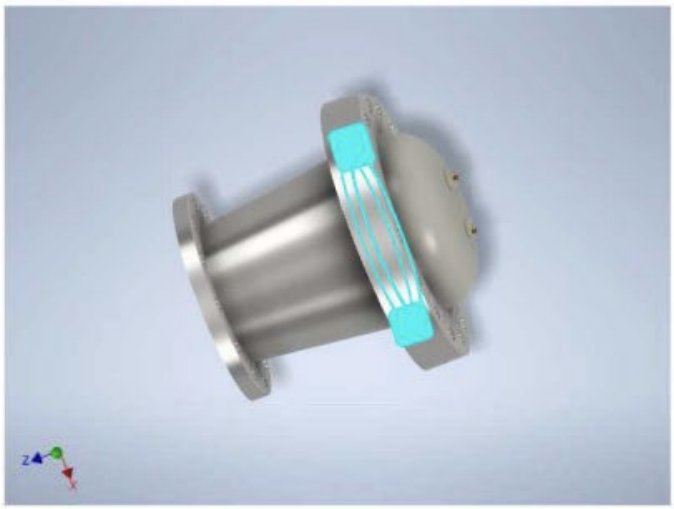

Fixed Constraint:4

Constraint Type	Fixed Constraint

Selected Face(s)

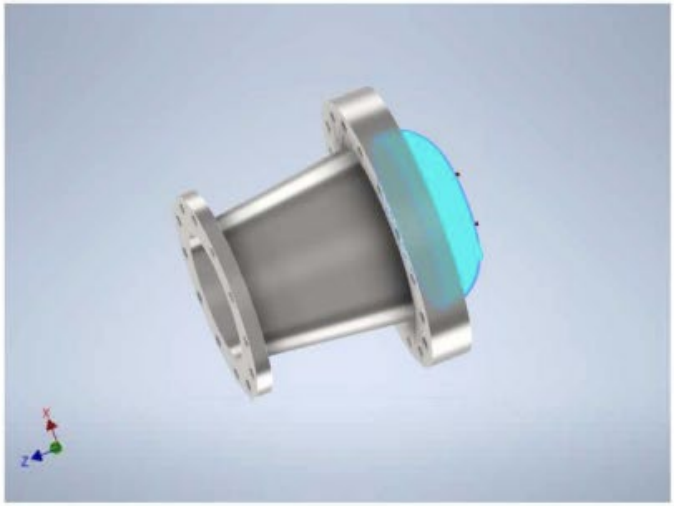

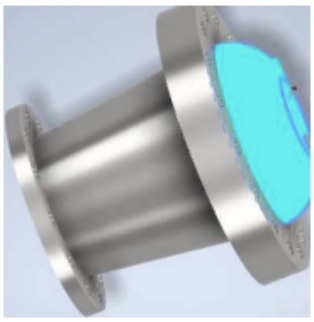

z

Contacts (Bonded)

Name	Part Name(s)
Bonded:1	DN250:1 Overgang 355 til 273:1
Bonded:2	dn355:1 dn355:2
Bonded:3	dn355:1 Overgang 355 til 273:1

Results

Reaction Force and Moment on Constraints

Constraint Name	Reaction Force		Reaction Moment	
	Magnitude	Component (X,Y,Z)	Magnitude	Component (X,Y,Z)
		0 N		0 N m
Fixed Constraint:1	170058 N	0 N	0 N m	0 N m
		170058 N		0 N m
		0 N		0 N m
Fixed Constraint:2	54752,5 N	0 N	22,6577 N m	-22,6577 N m
		54752,5 N		0 N m
		0 N		0 N m
Fixed Constraint:3	626855 N	0 N	0 N m	0 N m
		-626855 N		0 N m
		0 N		0 N m
Fixed Constraint:4	922610 N	0 N	0 N m	0 N m
		922610 N		0 N m

Result Summary

Name	Minimum	Maximum
Volume	15963900 mm^3	
Mass	125,316 kg	
Von Mises Stress	0,0000126903 MPa	338,811 MPa
1st Principal Stress	-50,7859 MPa	414,731 MPa
3rd Principal Stress	-222,633 MPa	48,1144 MPa
Displacement	0 mm	0,173161 mm
Safety Factor	1,03302 ul	15 ul
Stress XX	-76,1847 MPa	231,285 MPa

Stress XY	-117,079 MPa	117,125 MPa
Stress XZ	-88,1582 MPa	86,1529 MPa
Stress YY	-80,1368 MPa	227,456 MPa
Stress YZ	-55,8896 MPa	60,9607 MPa
Stress ZZ	-217,845 MPa	393,202 MPa
X Displacement	-0,16892 mm	0,168675 mm
Y Displacement	-0,169589 mm	0,170061 mm
Z Displacement	-0,0229499 mm	0,0345731 mm
Equivalent Strain	0,00000000005467 ul	0,00156805 ul
1st Principal Strain	-0,000000841282 ul	0,00182566 ul
3rd Principal Strain	-0,000928565 ul	0,00000000272077 ul
Strain XX	-0,000526352 ul	0,00108308 ul
Strain XY	-0,000755162 ul	0,000755459 ul
Strain XZ	-0,00056862 ul	0,000555686 ul
Strain YY	-0,000533112 ul	0,00108489 ul
Strain YZ	-0,000360488 ul	0,000393196 ul
Strain ZZ	-0,000897679 ul	0,0016834 ul
Contact Pressure	0 MPa	42,6394 MPa
Contact Pressure X	-9,66511 MPa	7,58185 MPa
Contact Pressure Y	-10,8833 MPa	10,4029 MPa
Contact Pressure Z	-42,1976 MPa	31,9212 MPa

Figures

Von Mises Stress

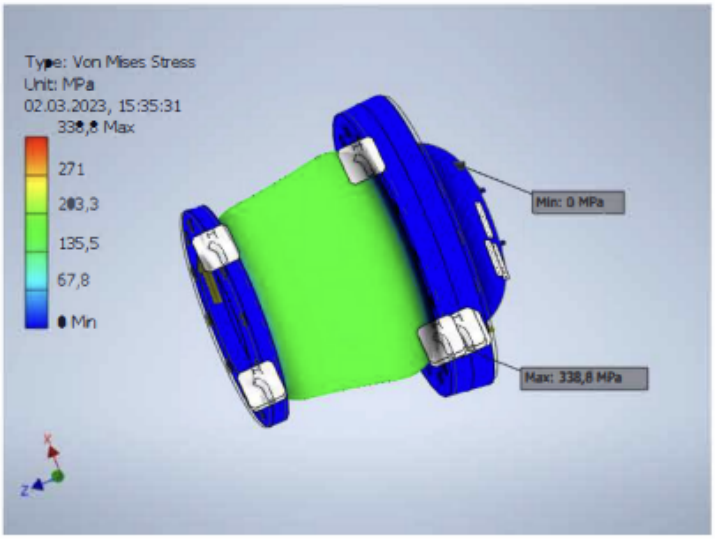

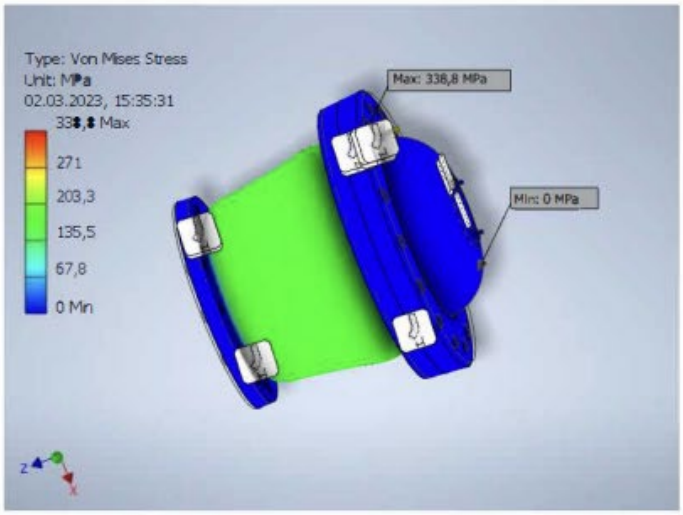

1st Principal Stress

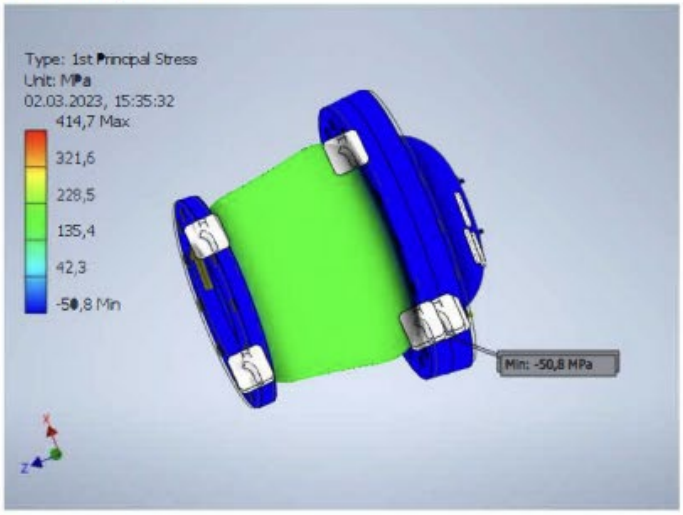

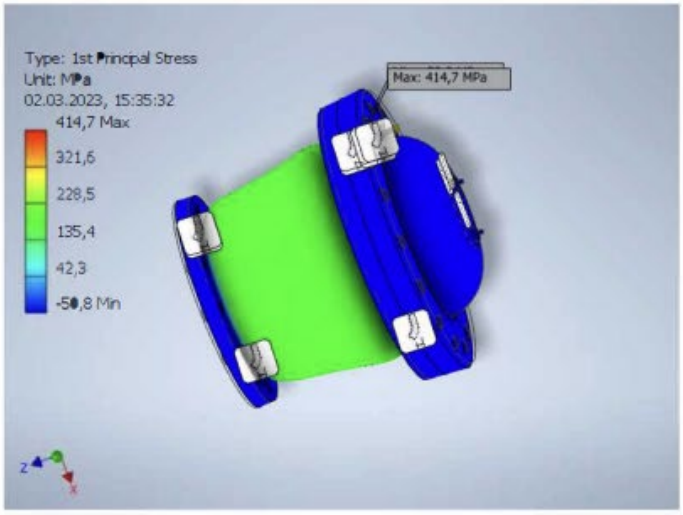

3rd Principal Stress

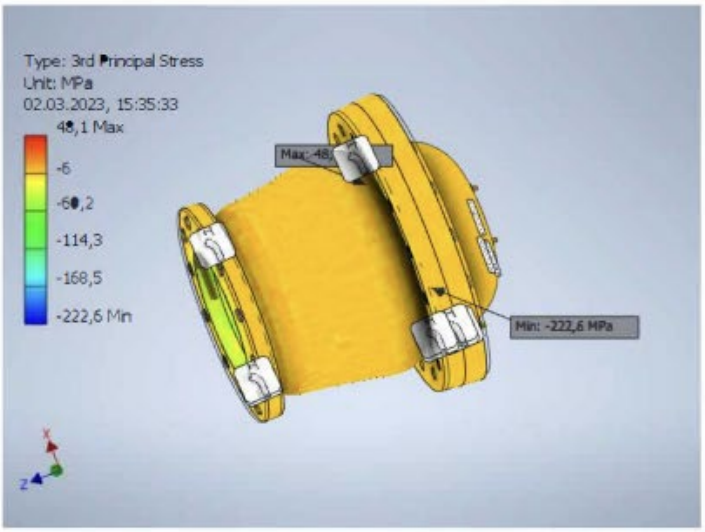

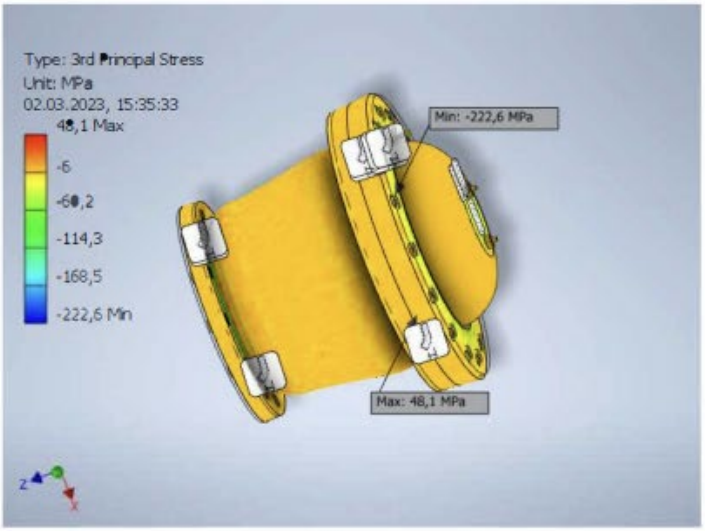

Displacement

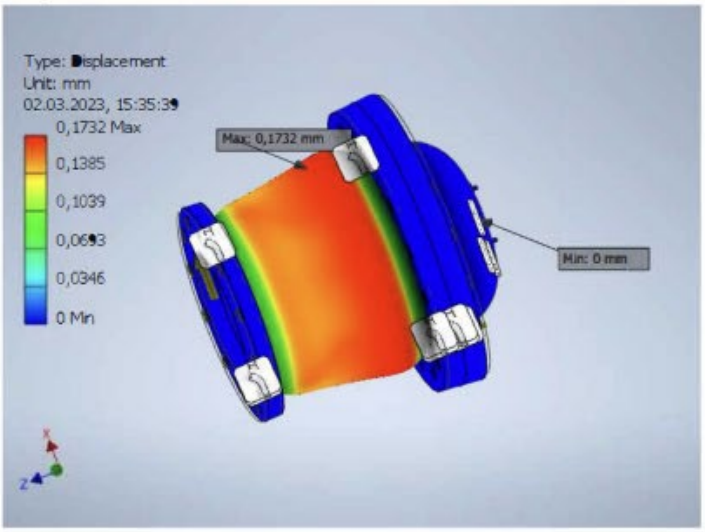

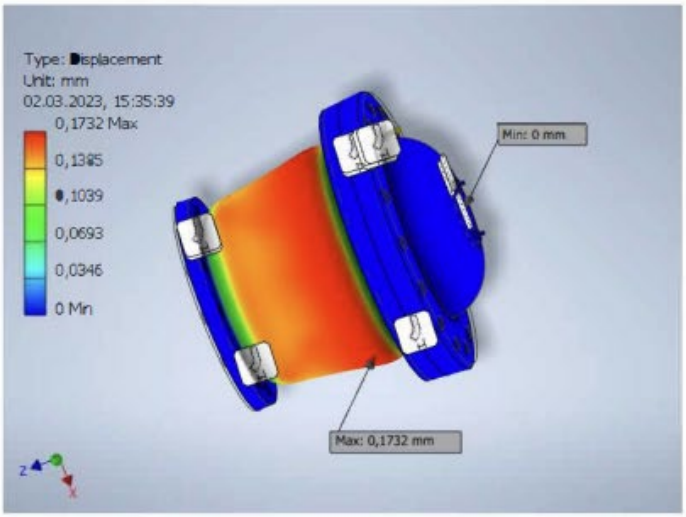

Safety Factor

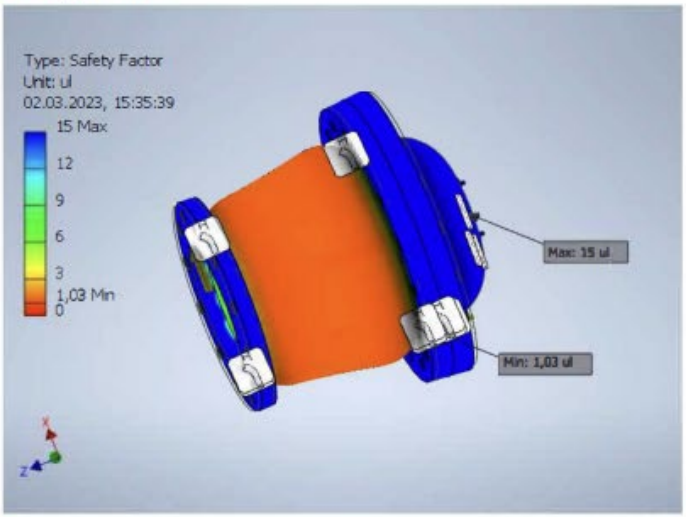

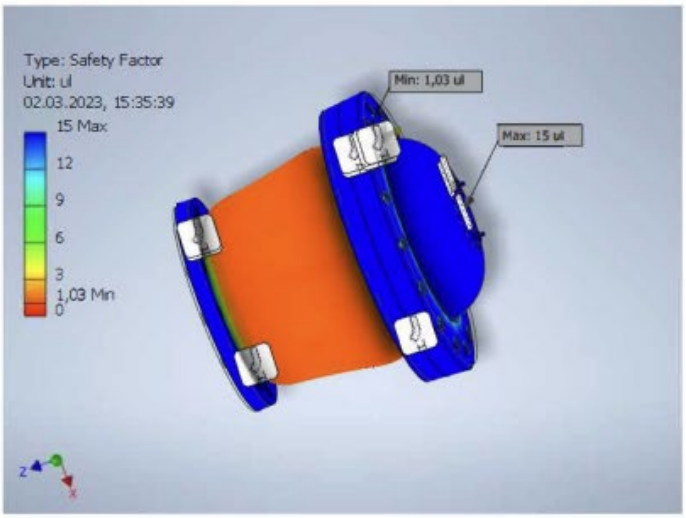

Stress XX

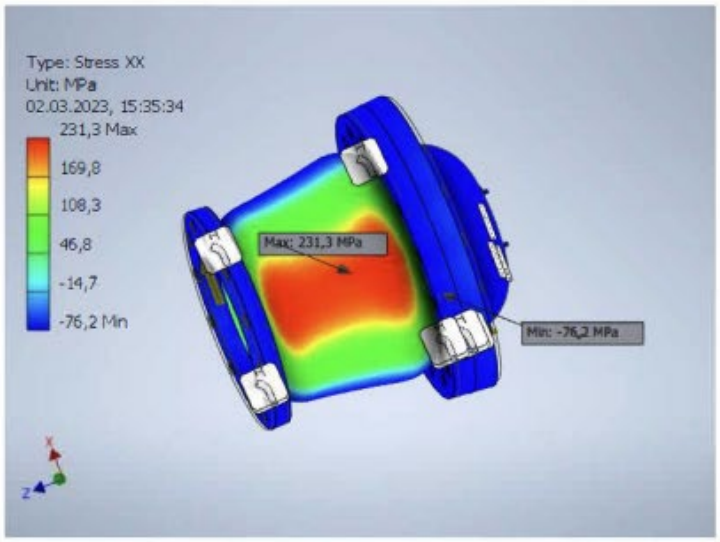
Type: Stress XX
Unit: MPa
02.03.2023, 15:35:34
231,3 Max
169,8
108,3
46,8
-14,7
-76,2 Min
Max: 231,3 MPa
Min: -76,2 MPa

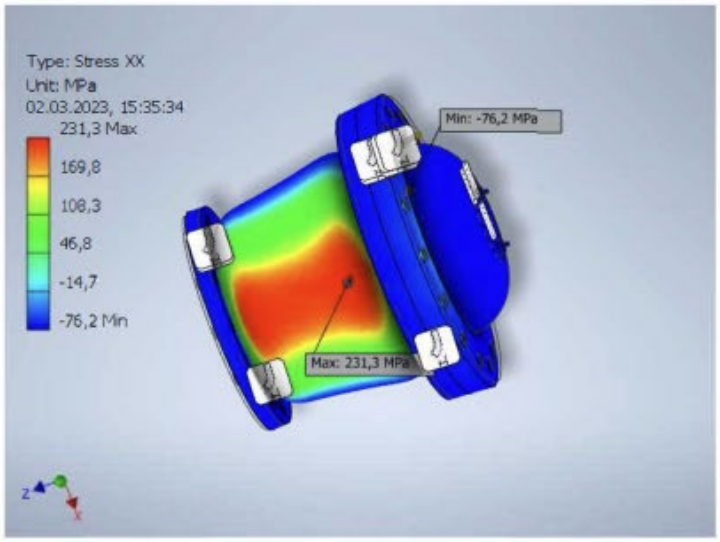
Type: Stress XX
Unit: MPa
02.03.2023, 15:35:34
231,3 Max
169,8
108,3
46,8
-14,7
-76,2 Min
Min: -76,2 MPa
Max: 231,3 MPa

Stress XY

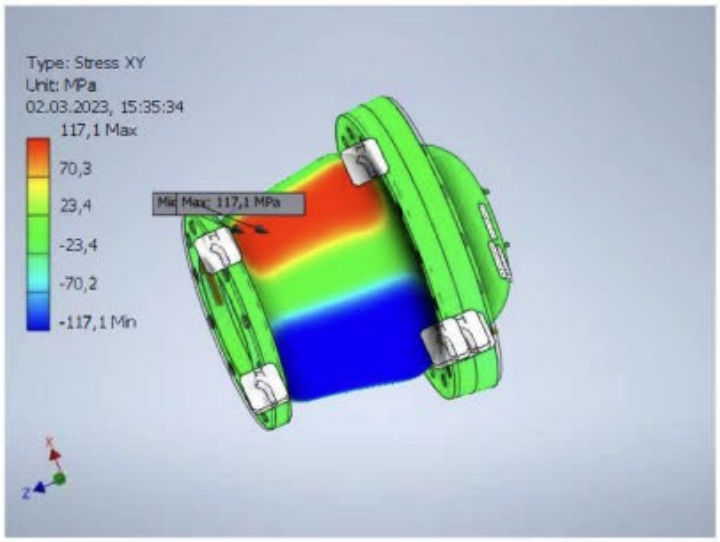
Type: Stress XY
Unit: MPa
02.03.2023, 15:35:34
117,1 Max
70,3
23,4
-23,4
-70,2
-117,1 Min
Max: 117,1 MPa

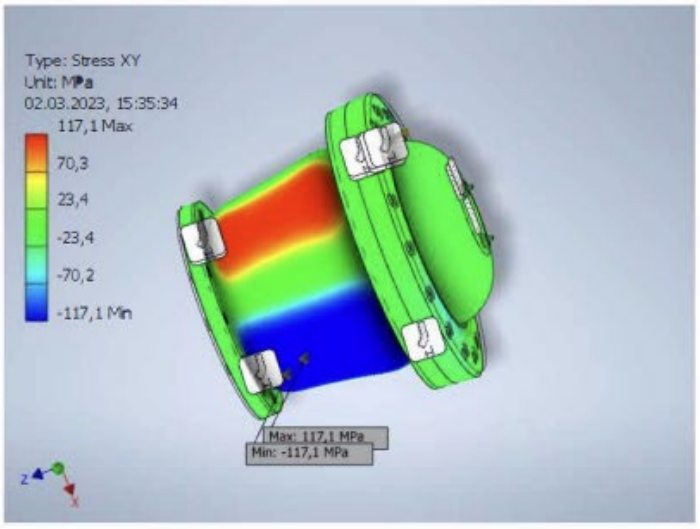

Stress XZ

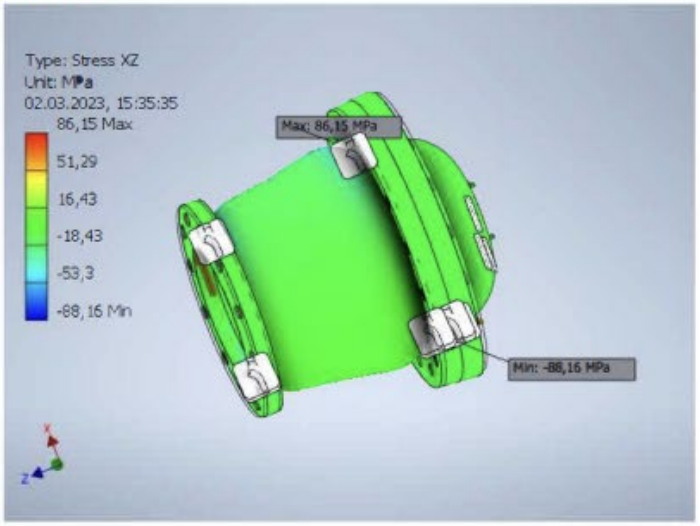

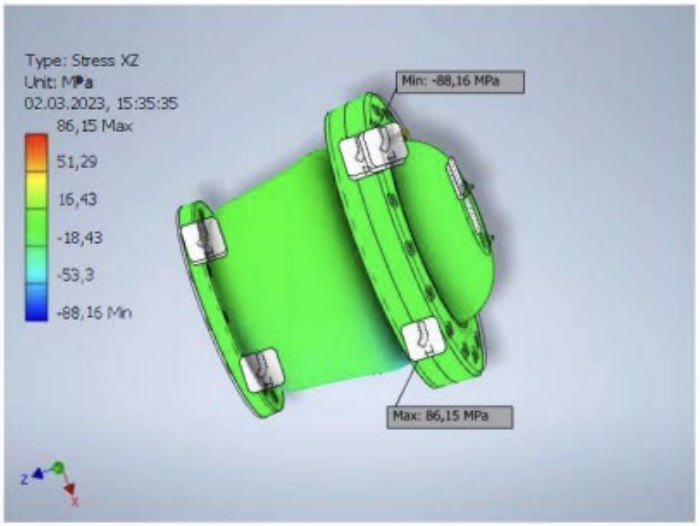

Stress YY

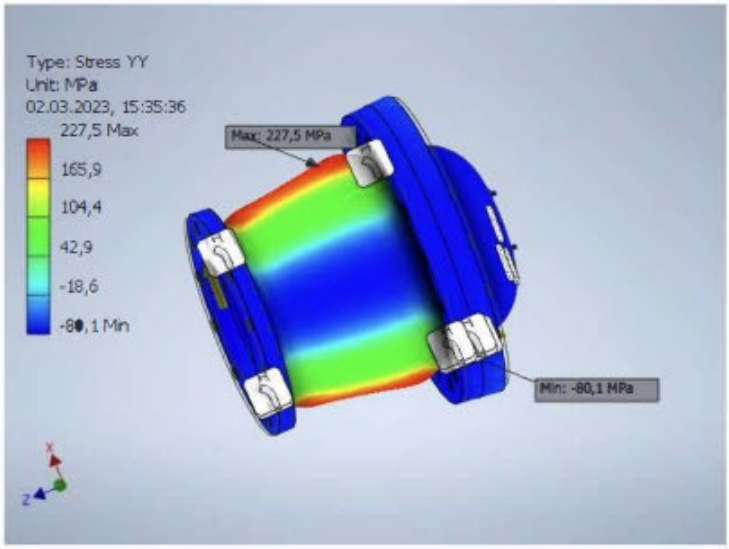
Type: Stress YY
Unit: MPa
02.03.2023, 15:35:36
227,5 Max
165,9
104,4
42,9
-18,6
-80,1 Min
Max: 227,5 MPa
Min: -80,1 MPa

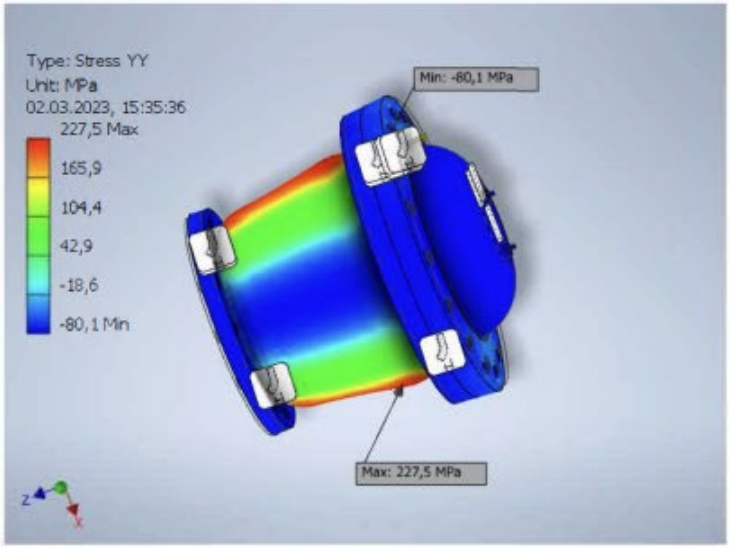
Type: Stress YY
Unit: MPa
02.03.2023, 15:35:36
227,5 Max
165,9
104,4
42,9
-18,6
-80,1 Min
Min: -80,1 MPa
Max: 227,5 MPa

Stress YZ

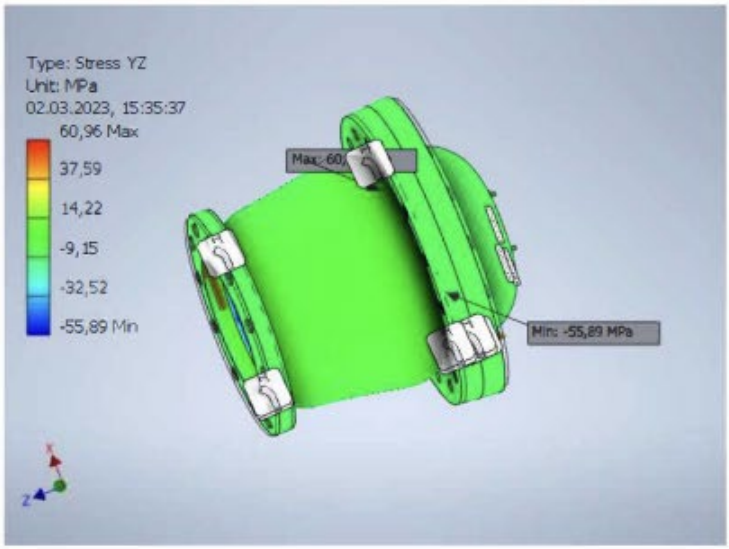
Type: Stress YZ
Unit: MPa
02.03.2023, 15:35:37
60,96 Max
37,59
14,22
-9,15
-32,52
-55,89 Min
Max: 60
Min: -55,89 MPa

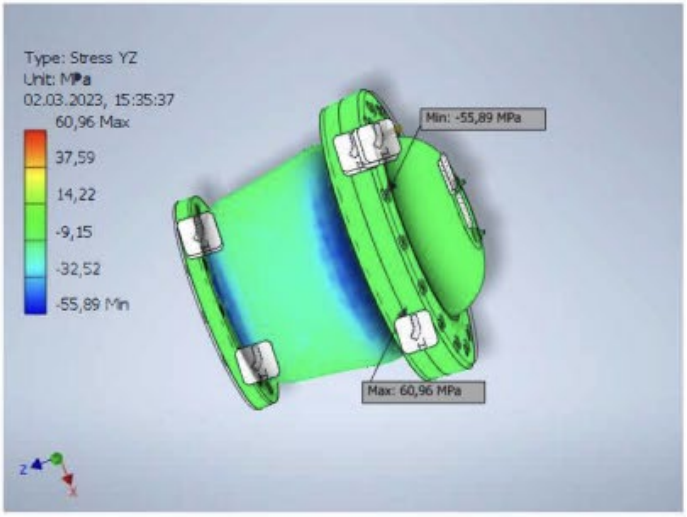

Stress ZZ

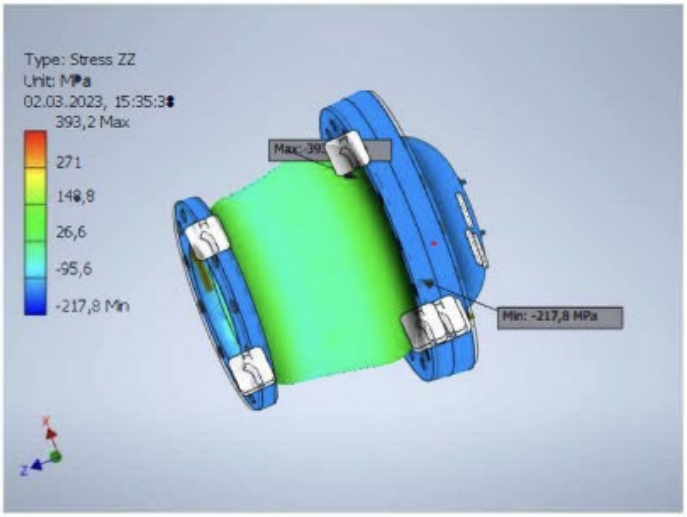

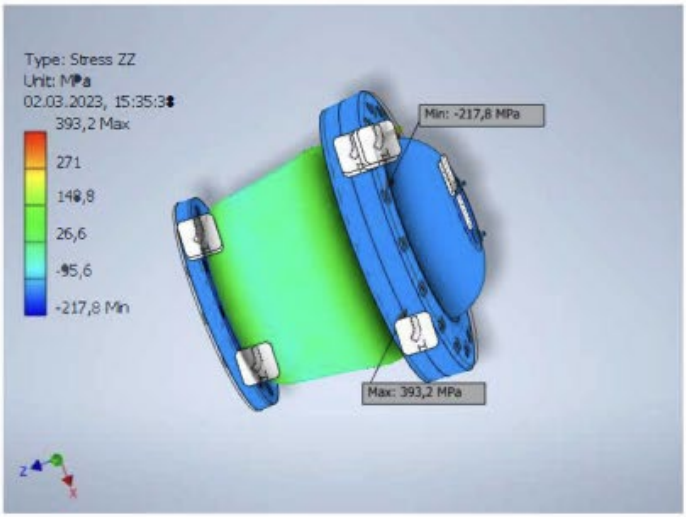

X Displacement

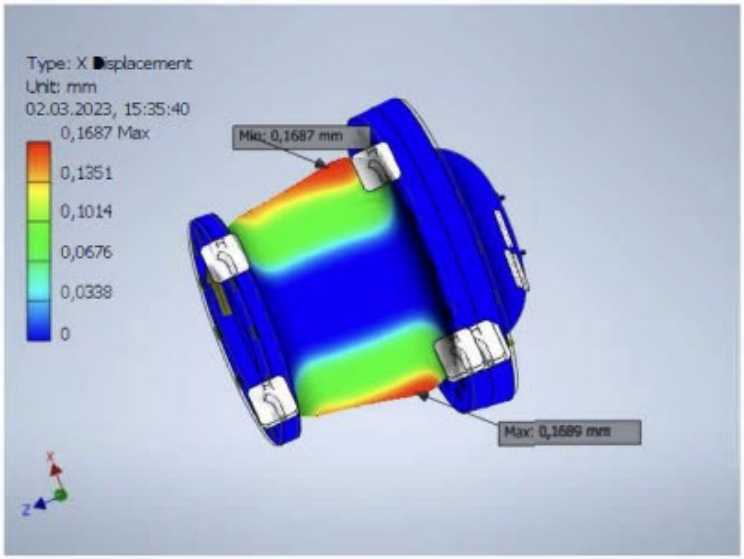

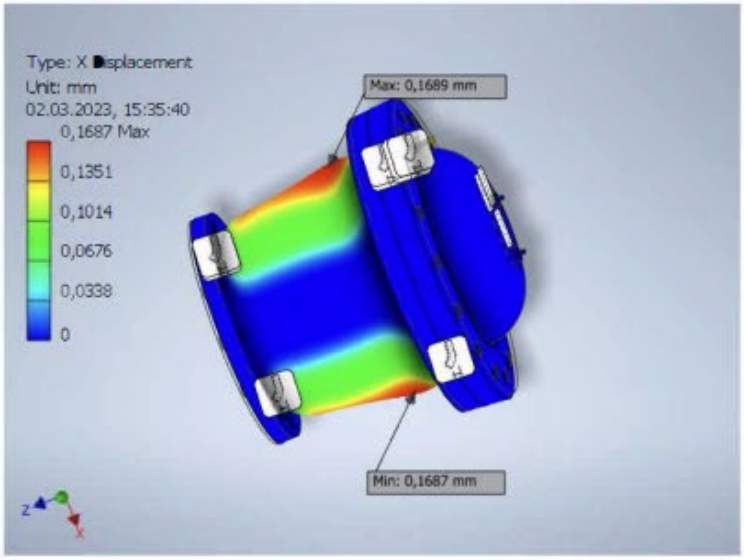

Y Displacement

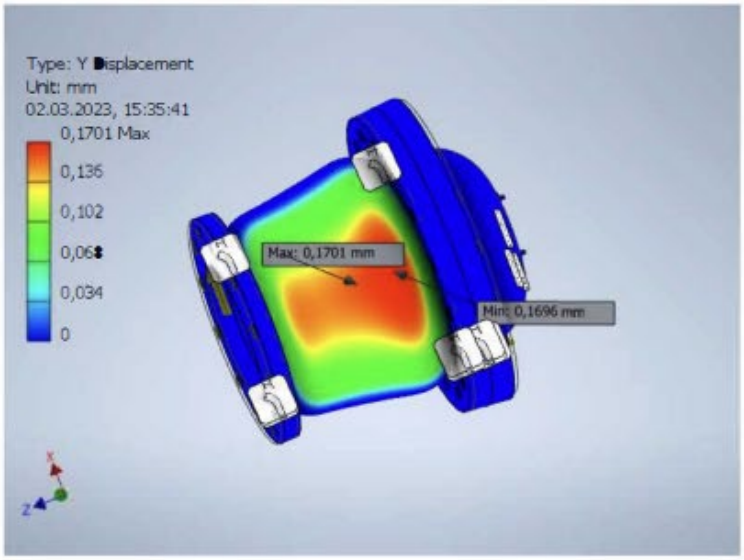

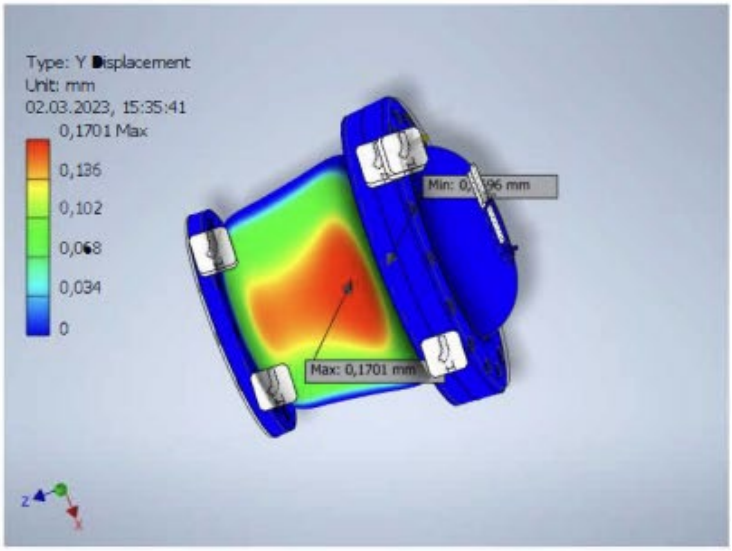

Z Displacement

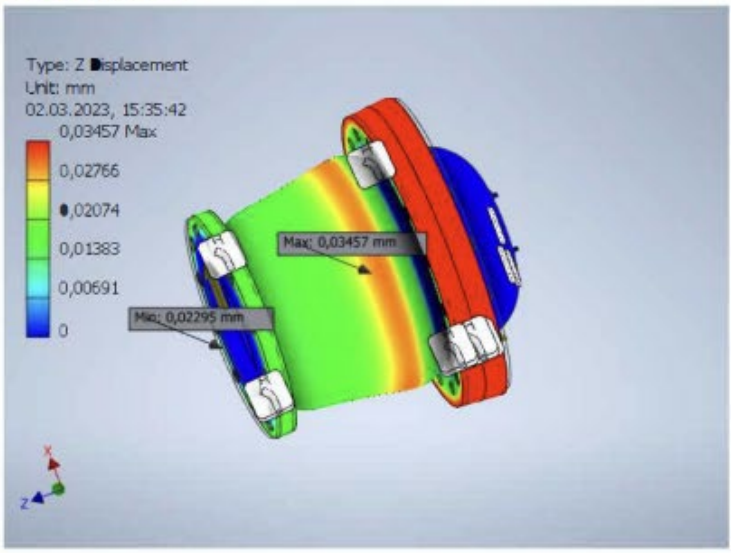

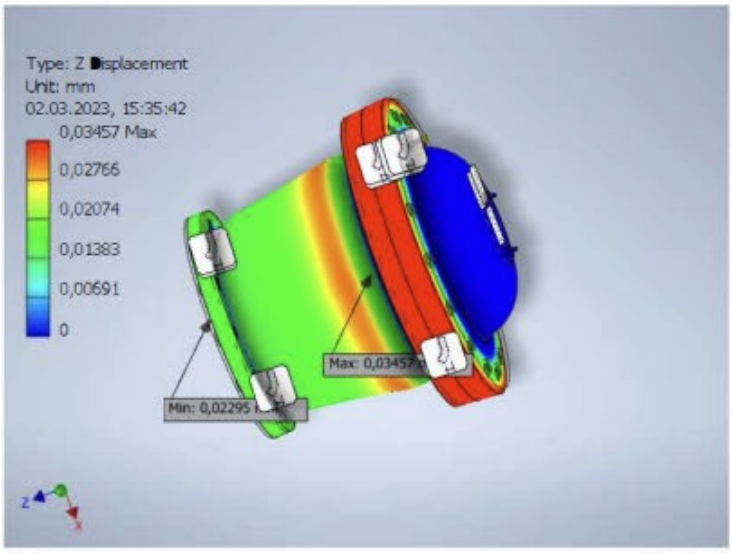

Equivalent Strain

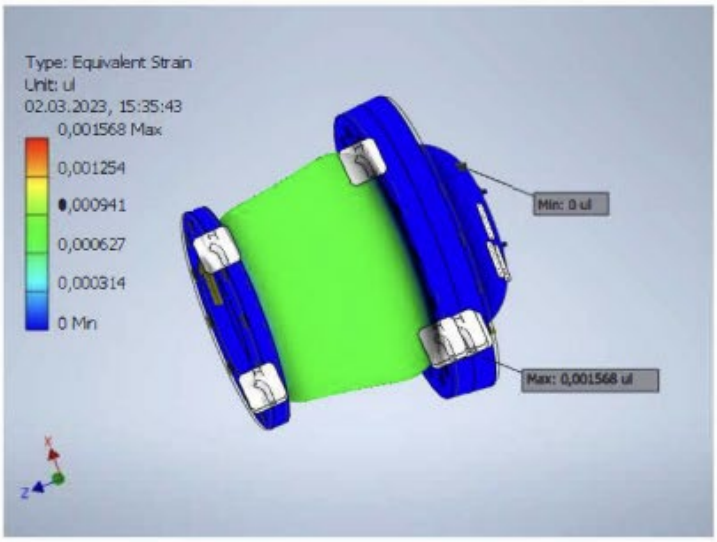

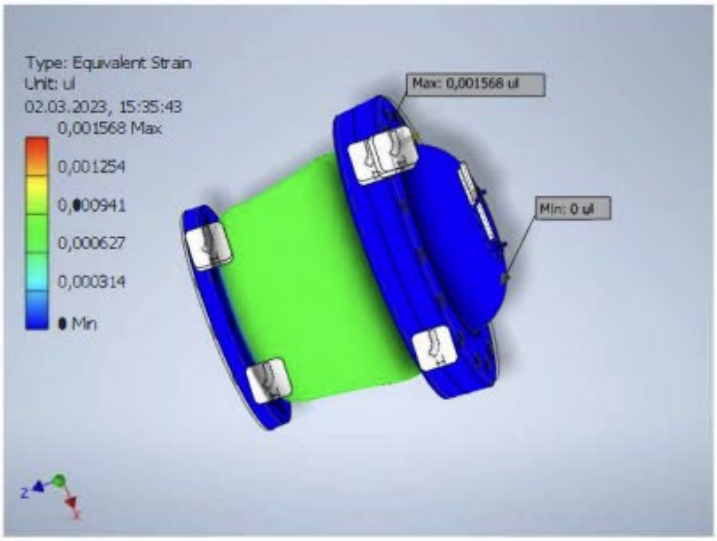

1st Principal Strain

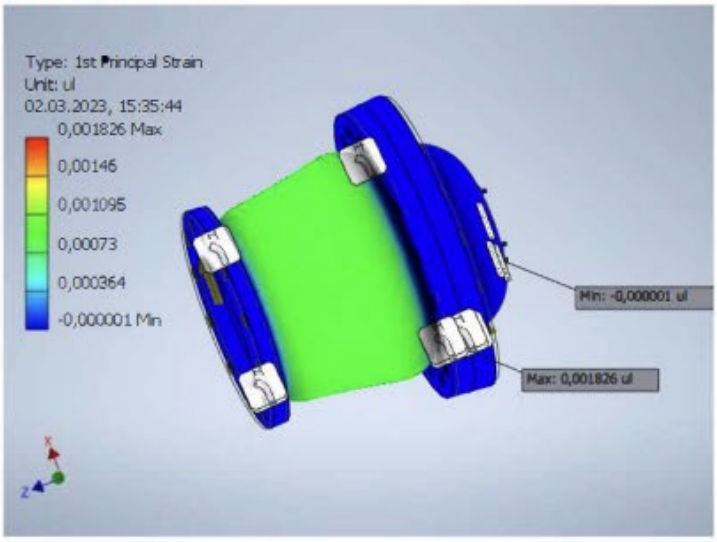

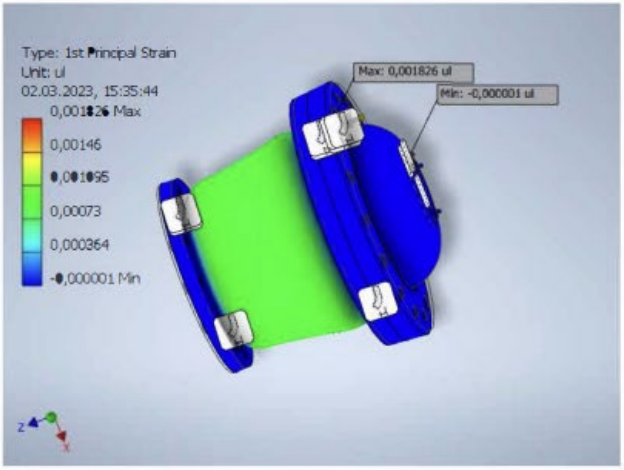

3rd Principal Strain

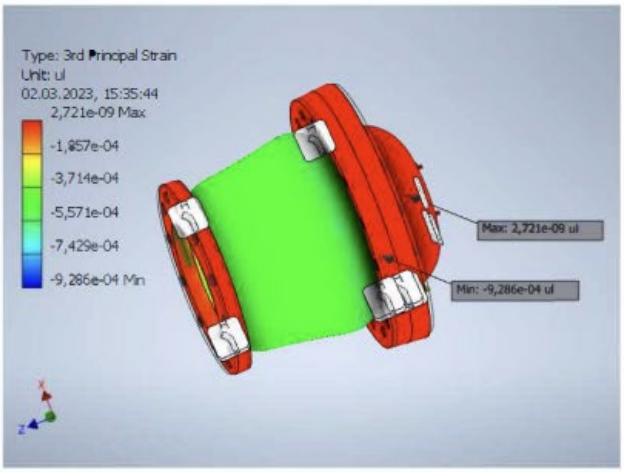

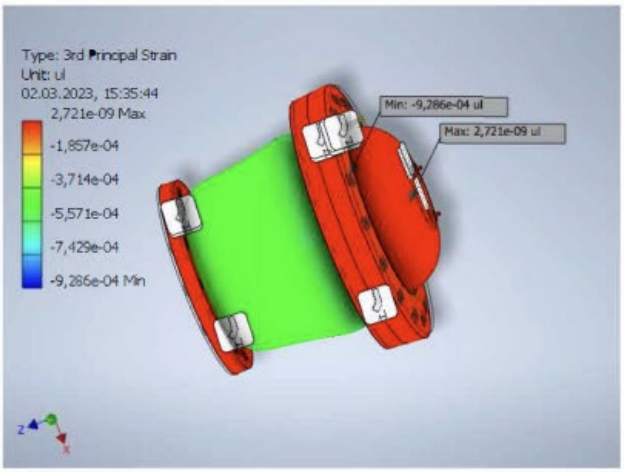

Strain XX

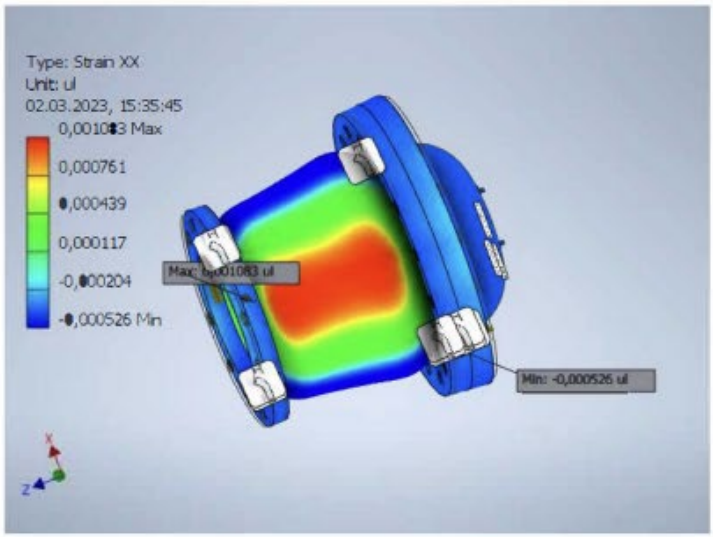
Type: Strain XX
Unit: ul
02.03.2023, 15:35:45
0,001083 Max
0,000761
0,000439
0,000117
-0,000204
-0,000526 Min
Min: -0,000526 ul

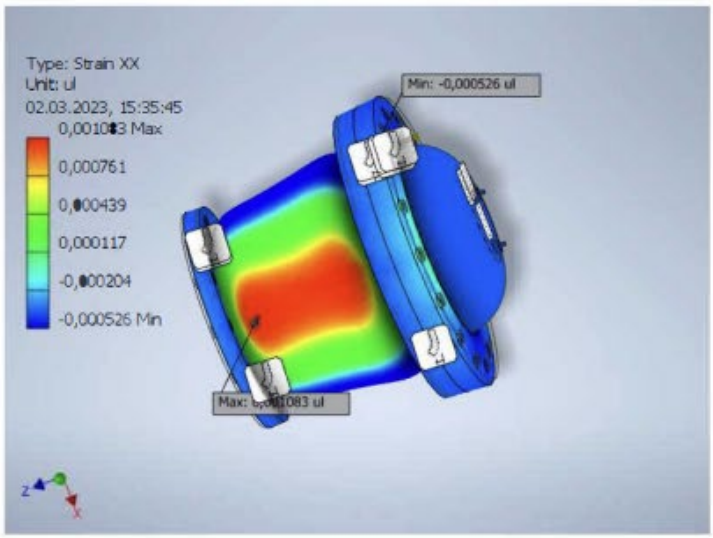
Type: Strain XX
Unit: ul
02.03.2023, 15:35:45
0,001083 Max
0,000761
0,000439
0,000117
-0,000204
-0,000526 Min
Min: -0,000526 ul

Strain XY

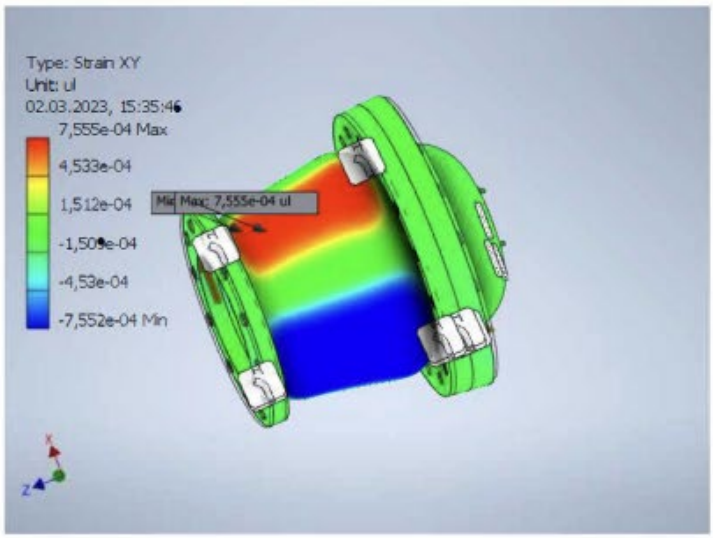
Type: Strain XY
Unit: ul
02.03.2023, 15:35:46
7,555e-04 Max
4,533e-04
1,512e-04
-1,509e-04
-4,53e-04
-7,552e-04 Min
Max: 7,555e-04 ul

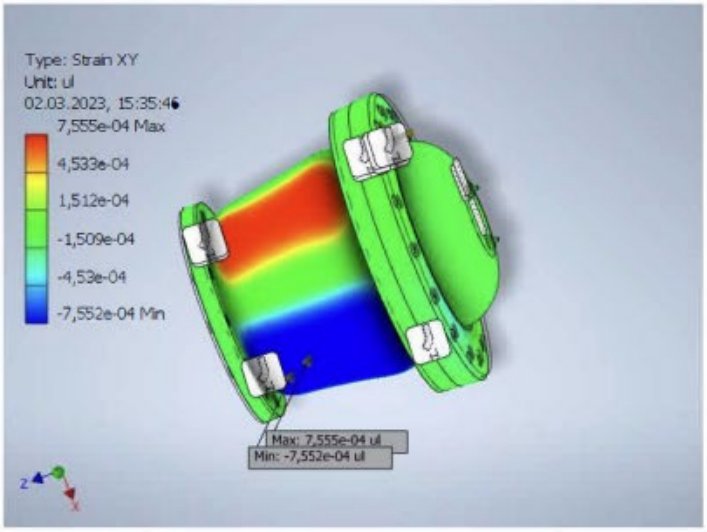

Strain XZ

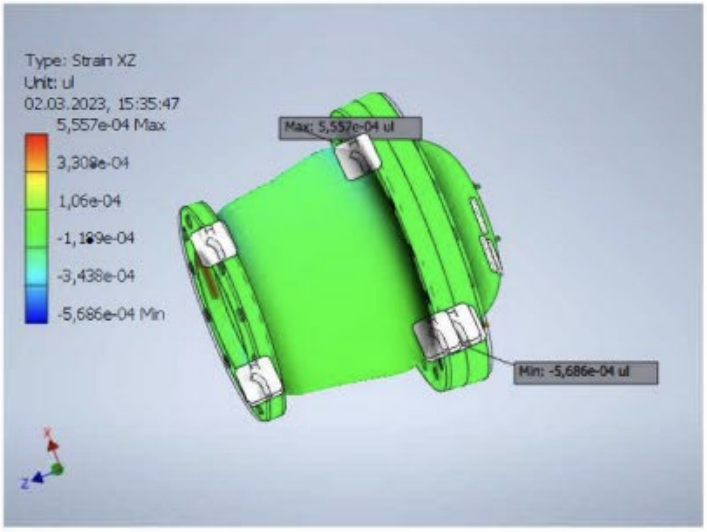

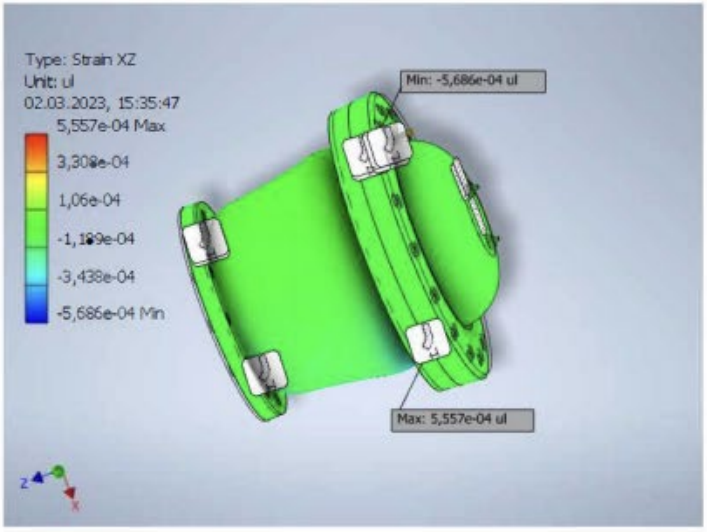

Strain YY

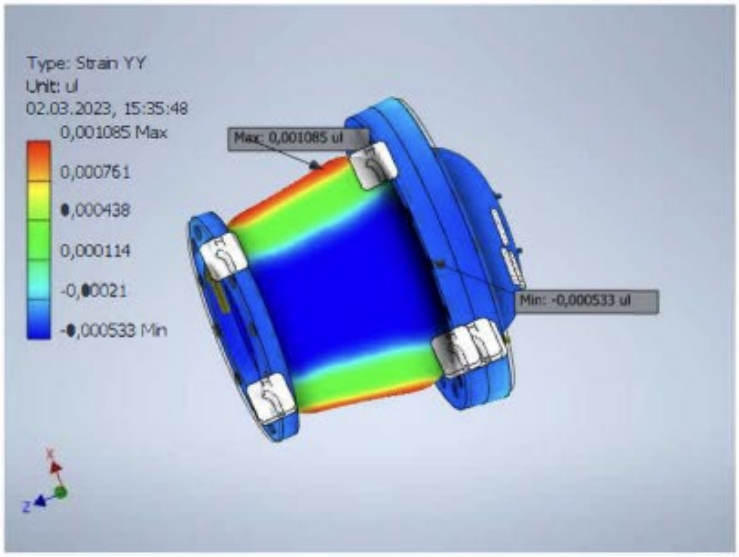
Type: Strain YY
Unit: ul
02.03.2023, 15:35:48
0,001085 Max
0,000761
0,000438
0,000114
-0,00021
-0,000533 Min
Max: 0,001085 ul
Min: -0,000533 ul

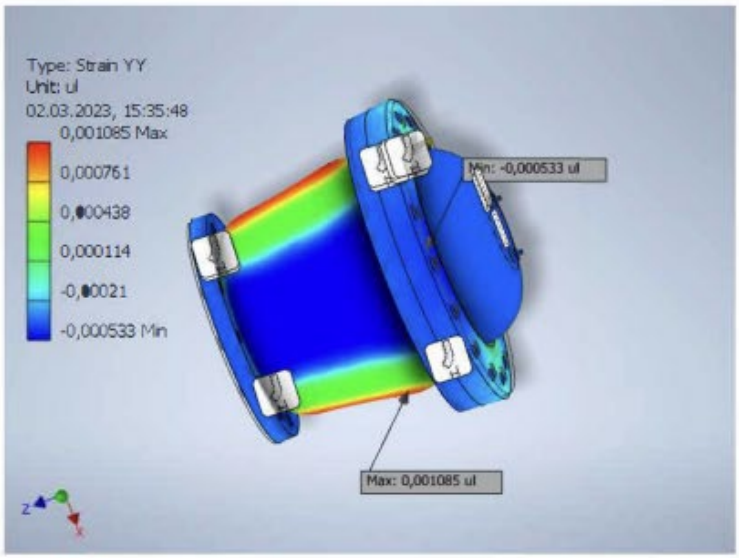
Type: Strain YY
Unit: ul
02.03.2023, 15:35:48
0,001085 Max
0,000761
0,000438
0,000114
-0,00021
-0,000533 Min
Min: -0,000533 ul
Max: 0,001085 ul

Strain YZ

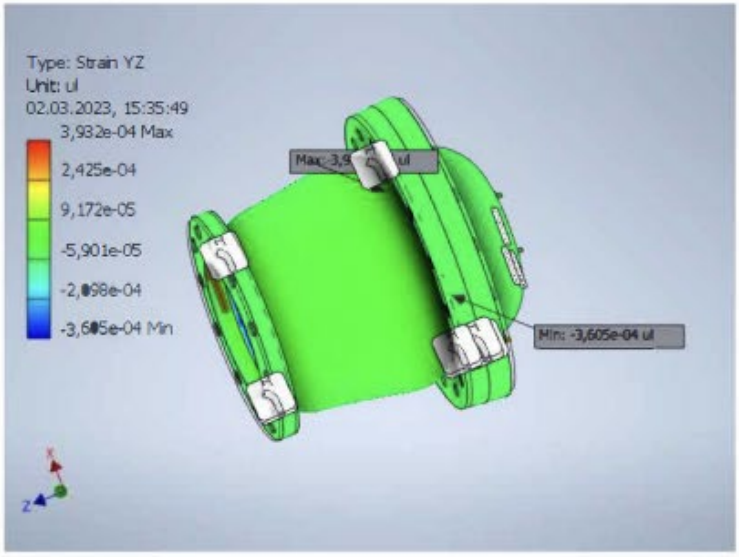
Type: Strain YZ
Unit: ul
02.03.2023, 15:35:49
3,932e-04 Max
2,425e-04
9,172e-05
-5,901e-05
-2,098e-04
-3,605e-04 Min
Min: -3,605e-04 ul

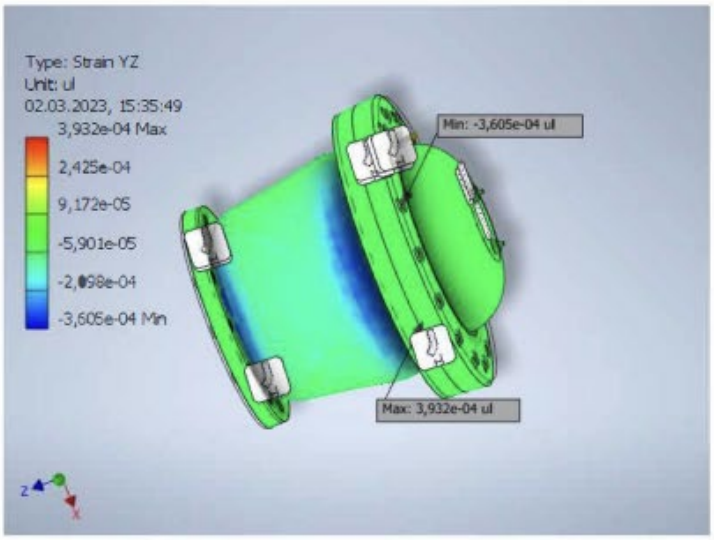

Strain ZZ

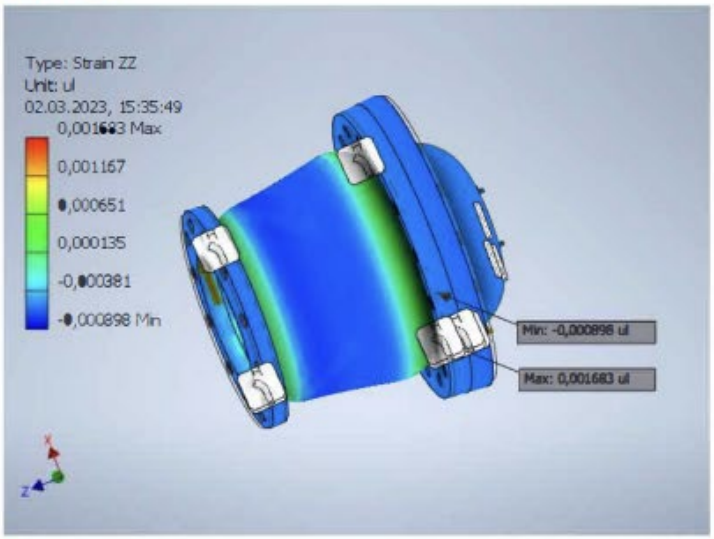

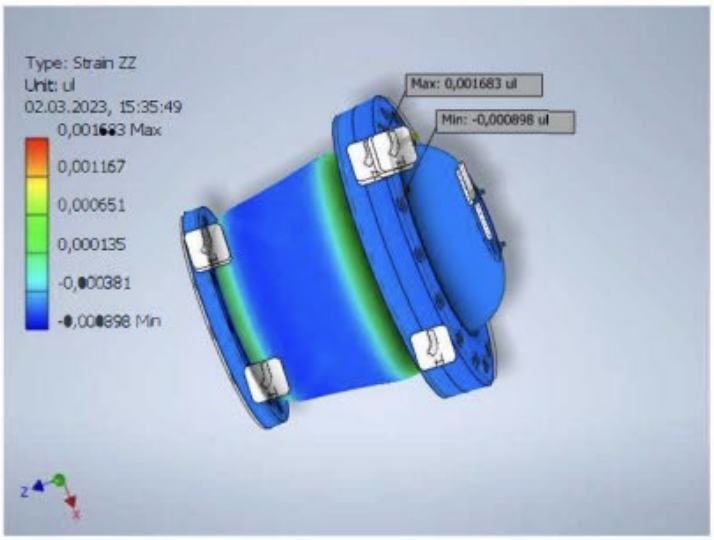

Contact Pressure

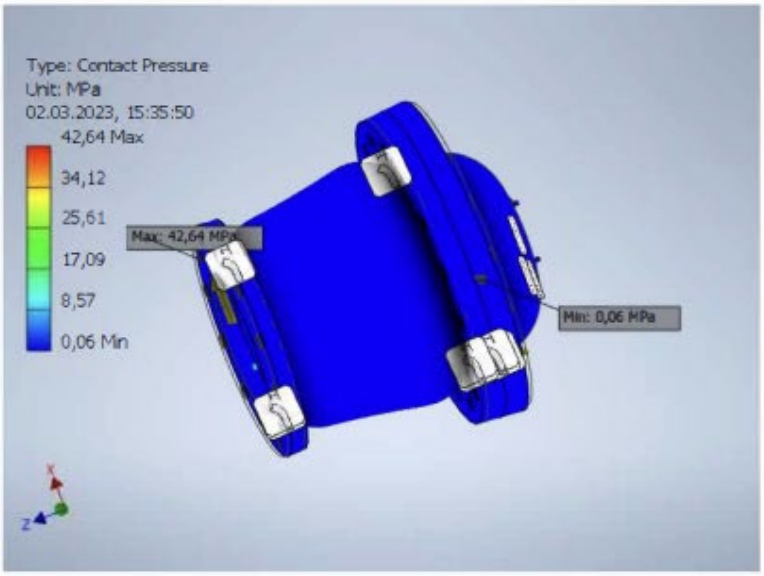

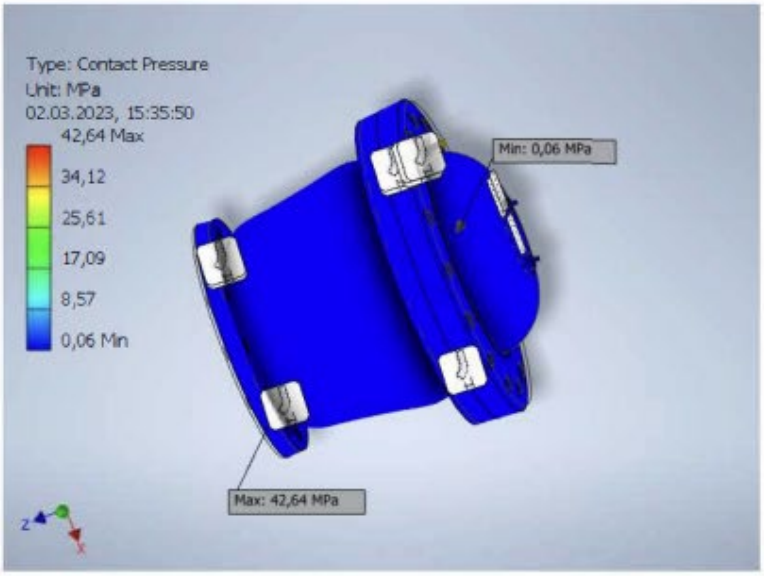

Contact Pressure X

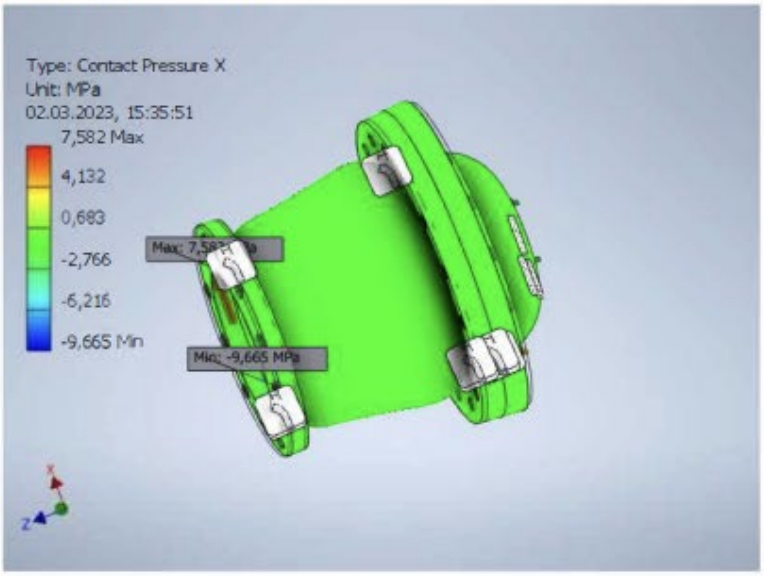

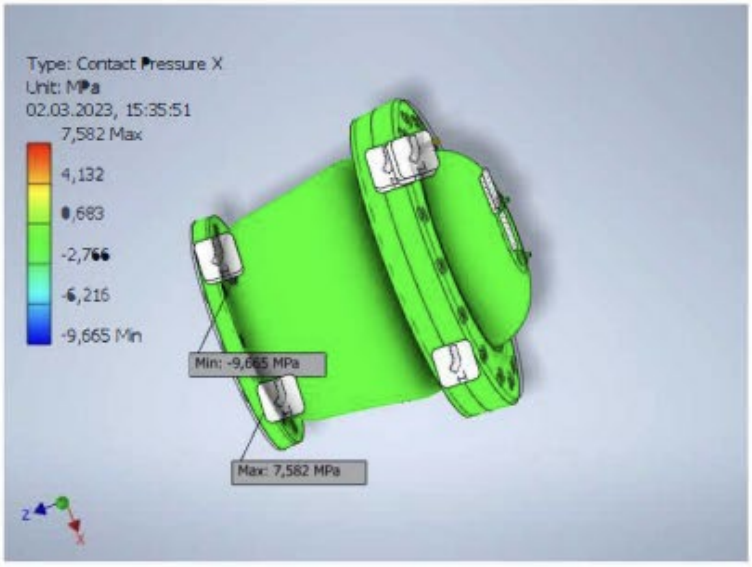

Contact Pressure Y

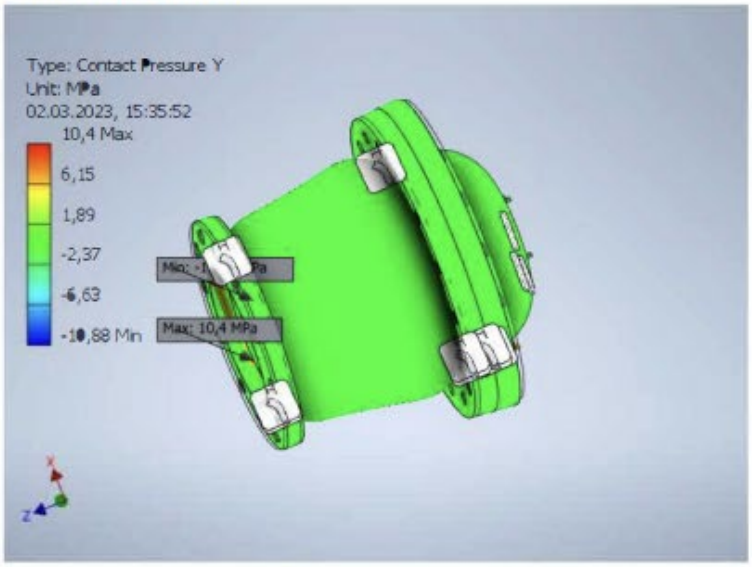

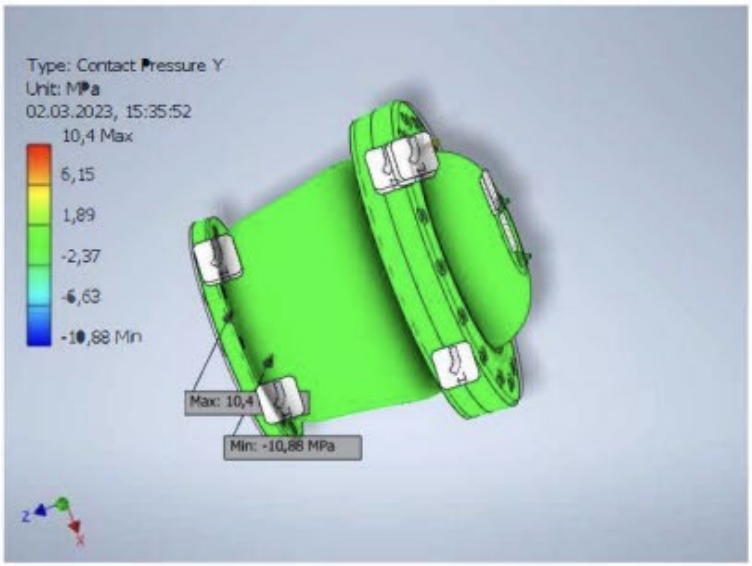

Contact Pressure Z

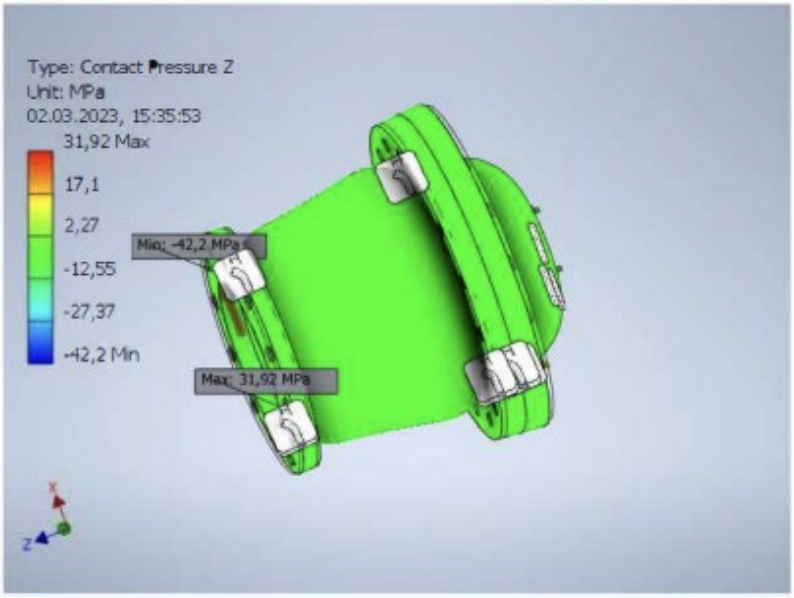
Type: Contact Pressure Z
Unit: MPa
02.03.2023, 15:35:53
31,92 Max
17,1
2,27
-12,55
-27,37
-42,2 Min
Min: -42,2 MPa
Max: 31,92 MPa

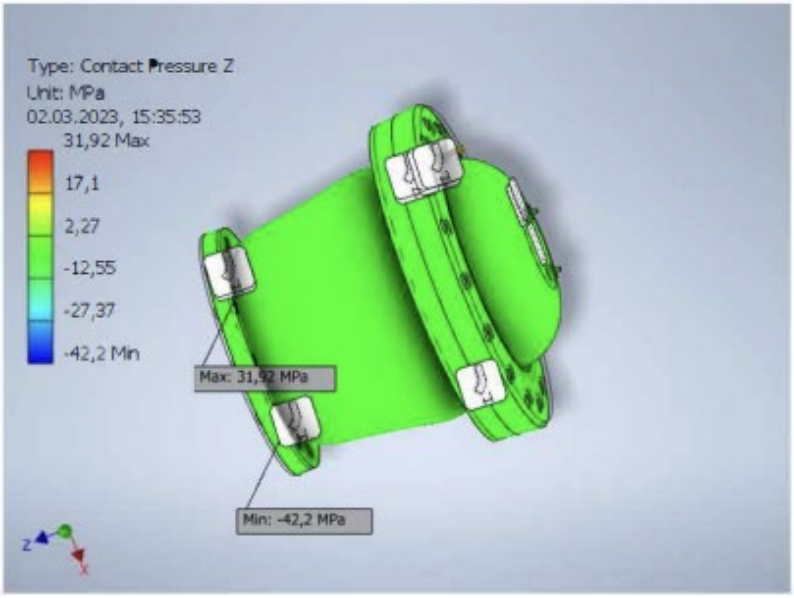
Type: Contact Pressure Z
Unit: MPa
02.03.2023, 15:35:53
31,92 Max
17,1
2,27
-12,55
-27,37
-42,2 Min
Max: 31,92 MPa
Min: -42,2 MPa